Achiral and Chiral Nematic Liquid Crystals for Printed Photonic Technologies



A Thesis submitted to the Board of the Faculty of the Mathematical, Physical and Life Sciences Division for the degree of Doctor of Philosophy in the University of Oxford

Xuke Qiu

Mansfield College

August 2025

Abstract

Achiral and Chiral Nematic Liquid Crystals for Printed Photonic Technologies

By Xuke Qiu

This thesis investigates the use of achiral and chiral nematic liquid crystals (LCs) for printed photonic applications, with a focus on droplet-based devices fabricated using drop-on-demand and electrohydrodynamic printing techniques. By combining the unique optical properties of LCs with the flexibility of printing methods, this work aims to develop compact, tunable, and scalable optical components.

The first part of the thesis presents the physical properties of nematic and chiral nematic LCs, including their phase behaviour, anisotropic dielectric and optical characteristics, and their response to alignment layers and external fields. These fundamental properties provide the basis for the later design and control of printed LC droplets. The experimental section describes the preparation of LC mixtures, substrate fabrication, and the printing processes used to generate droplets with defined internal configurations.

The core of the thesis is divided into three main parts. The first investigates the internal configuration of printed chiral nematic LC droplets under different alignment and doping conditions. Both simulations and experiments are employed to understand how the droplet geometry, anchoring strength, and chirality determine the director field within the droplet. This provides a fundamental understanding of structure formation in the printed LC droplets. As the chirality increases, droplets with planar anchoring evolve from bipolar configurations to spiral structures, while those with homeotropic anchoring transition from radial patterns to fingerprint-like textures. These transitions are captured by the helicity number N_0, which provides a simple predictive parameter for droplet structure control. The second part of the thesis explores how these droplets can modulate light in both phase and polarization. By printing droplets with different internal director profiles, complex structured light fields can be generated, which are then characterized using interferometric and polarimetric optical systems.

These include full Poincaré beams carrying two units of orbital angular momentum, radially and azimuthally polarized beams, and beam with polarization singularities.

The third part of the thesis presents the development of a printed LC droplet array as a novel compact device for full optical field sensing. The droplet array combines Stokes polarimetry with Shack-Hartmann wavefront sensing, enabling simultaneous measurement of the spatially resolved polarization and phase of an incident light beam. This device highlights the practical potential of printed LC droplets for integrated optical sensing applications. Combined, the work presented in the thesis demonstrates the potential of printed achiral and chiral nematic LC droplets as building blocks for functional optical devices that can both generate complex optical fields and characterise their properties. The ability to control the internal droplet structure through printing offers new pathways for miniaturized photonic systems in beam sensing and structured light generation.

Acknowledgements

I would like to express my deepest gratitude to my four supervisors: Professor Stephen M. Morris, Professor Steve J. Elston, Professor Alfonso Castrejón-Pita, and Professor Chao He, for their invaluable support throughout this journey. Steve M, thank you for welcoming me into the SMP group and making me feel part of a family from the very beginning. Your steady guidance at every stage of my D.Phil, from the first day to the final viva, ensured that I never missed out on what it truly means to do a D.Phil. Your kindness, clarity, and calm presence have defined my Oxford experience. Steve E, thank you for your constant support on the project, and for always taking the time to explain things with clarity and depth. You have a remarkable way of turning complex problems into manageable ones, and every conversation with you left me more confident and inspired. Alfonso, thank you for your generous support on the printing side and for always checking in with warmth and encouragement. And to Chao, you've been far more than a supervisor. You brought new life into my project and opened my eyes to the beauty of optics. Whenever there was a problem, you were the first to show up, with ideas, with energy, or simply with the right words. Because of you, this journey has not only been meaningful but filled with joy and momentum.

I am also deeply thankful to everyone in the SMP, FD and VOP groups who made this journey both meaningful and memorable. Mengmeng and Guanxiong were the first senior members I met when I arrived in Oxford. Guanxiong, thank you for your clear and patient training which helped me quickly find my footing. Mengmeng, as both my college mother and the senior who guided me most closely, you gave me tremendous support both in and out of the lab. I am also grateful to Zimo and Yifei for your valuable help in optics, and to Jinge and Runcheng for your wholehearted involvement in my project despite being juniors. Alva and Waqas, thank you for sharing your experience and always being willing to help when I needed it. To Bohan, Linpei, and Adi, thank you for the daily conversations and support which made the long research hours far more enjoyable.

Finally, no words can truly capture the depth of my gratitude to those closest to me. To

Yuxuan, thank you for being the person who accompanied me through this entire journey. You didn't fix the struggles or share the research, but you were there, in the middle of it all. More than anything, thank you for being my closest friend through these years. No matter what lies ahead, I will always be grateful that you were with me through this chapter. To my parents, your love has never asked for anything in return. Through every uncertain moment you stood quietly behind me, giving without measure and believing without hesitation. During my D.Phil. I experienced the most painful loss of my life. I lost you, Dad. There is no paragraph that can contain what that meant. But you remain with me, not only in memory, but in the way I think, in the choices I make, and in the responsibilities I now carry. I hope you can see that I have not forgotten your teachings, and I hope you would be at peace knowing that I will protect mom, just as you once did for both of us.

Publications

Thesis-related

1. Alva C. J. Orr, **Xuke Qiu**, Waqas Kamal, Thomas C. Sykes, Steve J. Elston, Julia M. Yeomans, Stephen M. Morris, Alfonso A. Castrejón-Pita **Topologically Frustrated Structures in Inkjet Printed Chiral Nematic Liquid Crystal Droplets – Experiments and Simulations** *Soft Matter* 7493 (2024).
2. **Xuke Qiu**, Runchen Zhang, Yifei Ma, Zimo Zhao, Zipei Song, Alva C. J. Orr, Mengmeng Li, Waqas Kamal, Jinge Guo, Alfonso A. Castrejón-pita, Steve J. Elston, Stephen M. Morris, Chao He **Complex Structured Light Generation using Printed Liquid Crystal Droplets** [*under review*]
3. **Xuke Qiu**, Jinge Guo, Jiahe Cui1, Runchen Zhang, Zimo Zhao, Yifei Ma, Steve J Elston, Alfonso A. Castrejón-pita, Stephen M Morris, Chao He **Full Vectorial Field Sensor Based on LC Droplet Array** [*in preparation*]

Other publications

1. Runchen Zhang, **Xuke Qiu**, Yifei Ma, Zimo Zhao, An Aloysius Wang, Jinge Guo, Ji Qin, Steve J. Elston, Stephen M. Morris, and Chao He **Physically Plausible Vectorial Metrics for Polarization Information Analysis** [*under review*]
2. An Aloysius Wang, Yifei Ma, Yunqi Zhang, Zimo Zhao, Yuxi Cai, **Xuke Qiu**, Bowei Dong, and Chao He. **Unlocking New Dimensions in Photonic Computing using Optical Skyrmions** [*under review*]
3. Bohan Chen, Peng Xie, Zimo Zhao, Patrick S. Salter, Mengmeng Li, Linpei Xue, **Xuke Qiu**, Martin J. Booth, Steve J. Elston, and Stephen M. Morris **Ultrafast Laser-Writing of Liquid Crystal Waveguides** *Ultrafast Science* 0065 (2024)

4. Chao He, Binguo Chen, Zipei Song, Zimo Zhao, Yifei Ma, Honghui He, Lin Luo, Tade Marozsak, An Aloysius Wang, Rui Xu, Peixiang Huang, Jiawen Li, **Xuke Qiu**, Yunqi Zhang, Bangshan Sun, Jiahe Cui, Yuxi Cai, Yun Zhang, Andong Wang, Mohan Wang, Patrick Salter, Julian AJ Fells, Ben Dai, Shaoxiong Liu, Limei Guo, Yonghong He, Hui Ma, Daniel J.Royston, Steve J. Elston, Qiwen Zhan, Chengwei Qiu, Stephen M. Morris, Martin J. Booth, and Andrew Forbes **A Reconfigurable Arbitrary Retarder Array as Complex Structured Matter** *Nature Communication* 4902 (2025)
5. Mengmeng Li, Steve J. Elston, Chao He, **Xuke Qiu**, Alfonso A. Castrejón-Pita, and Stephen M. Morris **Printed Liquid Crystal Optical Vortex Beam Generators** *Advanced Optical Materials* 2400450 (2024)

Conferences

British Liquid Crystal Society Annual Meeting 2024

Worcester College, Oxford, United Kingdom – April 2024 (***Poster***)

"Complex Structured Light Generation using Printed Liquid Crystal Droplets"

Table of Contents

1 Introduction 2

1.1 Aim and Motivation 2

1.2 Layout of the Thesis 5

2 Background 10

2.1 Liquid Crystals 10

2.2 Liquid Crystal Phases 11

2.2.1 Nematic phase 12

2.2.2 Chiral nematic phase 14

2.3 Physical Properties of the Nematic Phase 16

2.3.1 Alignment 16

2.3.2 Elastic energy 18

2.3.3 Dielectric permittivity 20

2.3.4 Optical properties of nematic phase 21

2.4 Optical Properties of the Chiral Nematic Phase 25

2.5 Printing Liquid Crystalline Materials 28

2.6 Summary 29

3 Experimental Methods 32

3.1 Introduction 32

3.2 Sample Preparation 33

3.2.1 mixture preparation 33

3.2.2 Substrate preparation 33

3.3 Fabrication of In-plane Electrode Substrates 35

3.4 Polarized Optical Microscopy 38

3.5 Pitch Measurements 41

3.5.1 Short-pitch chiral nematic liquid crystals 42

3.5.2 Long-pitch chiral nematic liquid crystals 44

3.6 Ink-Jet Printing System 50

3.6.1 MicroFab Jetlab - II 50

3.6.2 Bespoke Inkjet Printing System 55
3.7 The EHD Printing 58
3.8 Summary 60
4 Printed Chiral Liquid Crystal Droplets 63
4.1 Introduction 63
4.2 Simulation of the LC Director Field 64
4.2.1 Theoretical model 65
4.2.2 Director field generation 70
4.2.3 Simulating POM images 75
4.2.4 Simulation of chiral nematic LC droplets 78
4.2.5 COMSOL simulations 83
4.3 Printed Chiral Nematic LC Droplet 87
4.3.1 Chiral nematic LC droplet on a homeotropic alignment layer 88
4.3.2 Chiral nematic LC droplet on a planar alignment layer 104
4.4 Summary 108
5 Printed LC droplets for structured light generation 110
5.1 Introduction 110
5.2 Fundamental Concepts in Optics 112
5.2.1 Polarization and phase 113
5.2.2 Jones vectors and Stokes vectors 114
5.2.3 Vectorial light responses 117
5.2.4 Mueller matrix decomposition methods 119
5.3 Fabrication of LC droplets 121
5.4 Vectorial Optical Characterization of LC Droplets 124
5.4.1 Mueller polarimetry 124
5.4.2 The Mach-Zehnder Interferometer 127
5.5 Results and Discussion 128
5.5.1 Printed nematic LC on homeotropic alignment layer 129
5.5.2 Printed nematic LC on planar alignment layer 135
5.5.3 Printed long-pitch chiral nematic LC on a planar alignment layer 139

5.6 Summary 141
6 Printed LC Droplet Arrays for Full Vectorial Optical Field Sensors 145
6.1 Introduction 145
6.2 LC droplet Arrays for Stokes polarimetry 147
6.2.1 Introduction to division-of-wavefront polarimetry (DoWP) 147
6.2.2 Measurement principles 148
6.2.3 Conventional Stokes polarimetry 154
6.3 An LC droplet Array Shack-Hartmann Wavefront Sensor 155
6.3.1 Wavefront reconstruction method 155
6.3.2 Focal length of the LC droplet 161
6.3.3 Spatial light modulator calibration 162
6.4 Fabrication of the LC Droplet Array 165
6.5 Simultaneous Polarization and Phase Sensing 167
6.5.1 Experimental design for full optical field measurements 167
6.5.2 Polarization measurement result 173
6.5.3 Phase measurement result 178
6.6 Intensity Retrieval Capability 186
6.7 Summary 187
7 Conclusions and Future work 190
7.1 Concluding remarks 190
7.2 Future Work 193
7.2.1 Patterned alignment layers for enhanced structured light generation 194
7.2.2 Dynamic Tuning of LC Droplets 195
7.2.3 Full Poincaré Beam-Based Structured Illumination 195
7.2.4 High resolution full optical field sensing 196

List of Abbreviations

CLC	chiral nematic liquid crystal
DLW	direct laser writing
DoD	drop-on-demand
DOP	degree of polarization
DoWP	division-of-wavefront polarimetry
EHD	electrohydrodynamic
FEM	finite element method
FWP	four-division waveplate
HCl	hydrochloric acid
HTP	helical twisting power
HWP	half-wave plate
IPA	isopropyl alcohol
ITO	indium tin oxide
LC	liquid crystal
JM	Jones matrix
MM	Mueller matrix
MMPD	Mueller matrix polar decomposition
OAM	orbital angular momentum
OLED	organic light-emitting diode
OPD	optical path difference
PDE	partial differential equation
PDLC	polymer-dispersed liquid crystal
POM	polarized optical microscopy
PSA	polarization state analyser
PSCLC	polymer-stabilized chiral nematic liquid crystal
PSG	polarization state generator

PVA	polyvinyl alcohol
QWP	quarter-wave plate
RMS	root-mean-square
SHWS	Shack-Hartmann Wavefront Sensor
SLM	spatial light modulator
SoP	state of polarisation
STED	stimulated emission depletion
UV-Vis	ultraviolet-visible spectrophotometry
VVB	vector vortex beam
WS	wavefront sensor

Chapter 1

Introduction

“Every new beginning comes from some other beginning’s end.”

Seneca

1 Introduction

This chapter provides an overview of the motivation for the research presented in this thesis, emphasizing its relevance to the advancement of LC technologies and their integration with contemporary printing methods. It emphasizes the significance of printed LC droplets as key elements in the development of next-generation optical devices. The chapter concludes with an outline of the thesis, detailing the primary objectives and contributions addressed in each chapter.

1.1 Aim and Motivation

Advancements in modern manufacturing are increasingly focused on achieving higher levels of automation and miniaturization, driven by the need for precise, cost-effective, and scalable production techniques[1-3]. Among the various fabrication methods, drop-on-demand (DoD) inkjet printing has emerged as a viable approach due to its ability to produce microscale patterns with exceptional accuracy, low cost, and high throughput[4-9]. While initially developed for graphical printing and textiles, DoD inkjet printing has expanded its utility across multiple industries through the use of functional materials as inks, enabling applications in emerging technologies[10-12].

In the last two decades, LCs have been predominantly utilized in displays and optical devices, where they are confined between glass substrates to form layers[13-17]. However, the growing adoption of competing technologies, such as organic light-emitting diodes (OLEDs), necessitates the exploration of alternative applications for

LCs[18, 19]. The inherent properties of LCs, such as the birefringence and sensitivity to external stimuli, render them highly suitable for advanced optical systems and advanced responsive materials. DoD inkjet printing introduces a robust platform for the fabrication of new LC-based devices, offering precise patterning, compatibility with a variety of alignment layers, and deposition on both rigid and flexible substrates. These attributes enable the development of miniaturized and highly versatile optical components.

This thesis aims to integrate nematic and chiral nematic liquid crystals (CLCs) with DoD inkjet printing to advance the design and fabrication of compact optical devices. By leveraging the precision and scalability of this manufacturing technique, the work seeks to create LC droplets with controlled optical properties tailored to specific functional requirements. This approach facilitates the production of highly reproducible, cost-efficient devices capable of addressing complex optical challenges.

Recent investigations have demonstrated that nematic and chiral nematic LC droplets exhibit structural and optical properties of interest for various applications, including optical modulation[20], biosensing[21], and microlasers[22-24]. The internal configuration of these droplets is strongly influenced by factors such as surface anchoring conditions and external fields. Foundational studies by J. Bajc and S. Žumer elucidated the role of electric fields and surface anchoring in determining the director configurations of LC droplets[25, 26]. Subsequent research, including the work of David

Seč, examined the effects of chiral frustration and the variation of director fields with helical pitch in chiral nematic LC droplets[27]. Additionally, studies have highlighted the potential for these droplets to exhibit multistable structures whose optical responses can be modulated through external stimuli.

These structural characteristics are critical for a range of applications, such as displays[28], tunable lenses[29], beam-steering systems[30], and biosensors[21, 31]. However, the majority of prior research has relied on microfluidic techniques to generate LC droplets, which are typically suspended in solution. In contrast, LC droplets fabricated through DoD inkjet printing are deposited on rigid or conformable surfaces, resulting in distinct non-spherical geometries. The physical properties and external field responses of such droplets, shaped by printing conditions and substrate interactions, are likely to differ from their counterparts generated using microfluidic methods. This necessitates a systematic investigation to evaluate their behaviour and potential utility under varied fabrication parameters and geometries.

By establishing a detailed understanding of printed LC droplet structures and their interaction with external factors, this thesis seeks to bridge the gap between fundamental research and practical implementation. The findings will provide a foundation for integrating LC droplets into advanced optical devices, facilitating the development of innovative, efficient, and miniaturized technologies for future applications.

1.2 Layout of the Thesis

In this thesis, Chapter 1 establishes the motivation and objectives of this thesis, focusing on the integration of LC materials with DoD inkjet printing for advanced optical applications. The chapter also details the organization and structure of the thesis, providing synopses for each chapter, including the methodologies used throughout, the experiments conducted, and simulations.

Chapter 2 will provide the necessary fundamental information about liquid crystalline materials that will underpin the thesis. Initially, the thesis focuses on the LC phases of relevance to this work — the nematic phase and the chiral nematic phase. This section will introduce the physical properties of LCs, including the optical anisotropy and the alignment properties, which are critical for manipulating the orientation and internal ordering of LCs. In addition, LCs can respond to external stimuli such as electric fields, heat and light. This background chapter also introduces inkjet printing and describes previous work related to the use of such printing processes for depositing LCs. By evaluating these properties and printing techniques, this chapter introduces printed LC materials for advanced optical applications.

In the following chapter, Chapter 3, the experimental procedures employed in this thesis will be outlined, detailing the preparation of CLC mixtures, the fabrication of glass substrates with specific alignment layers, and methods for measuring the pitch. For short-pitch CLCs, the pitch was obtained by analysing the reflection band using

UV-vis spectroscopy, while for long-pitch CLCs, the pitch was determined using the Grandjean-Cano wedge cell method.

A comprehensive overview of the structure and functionality of the inkjet printing systems is presented, demonstrating their capability and operating conditions, respectively. This chapter also introduces the process for fabricating in-plane electrode substrates before concluding with a description of the imaging techniques used in this thesis, including polarization optical microscope imaging and high-speed shadowgraphy/polarization imaging.

Chapter 4 begins by detailing the theoretical framework and methodology for simulating CLC droplets. The simulation process is introduced to provide insights into the internal ordering of droplets and their interactions with substrate alignment layers, serving as a foundation for interpreting experimental results. Following this, experimental techniques for printing chiral nematic droplets of varying concentrations of chiral dopant onto substrates with different alignment layers are described.

The chapter then presents a comparative analysis of the simulated and experimental results, focusing on the internal director configuration of the droplets and the impact of chiral dopant concentration and substrate conditions. Further, it investigates the responses of these droplets to external stimuli, such as electric fields and temperature variations, to illustrate their complex behaviour.

Chapter 5 demonstrates how printed LC droplets can be used for the generation of complex structured light fields through vectorial beam modulation. This chapter investigates how the polarization and phase characteristics of light passing through the droplets are modified, which are determined using a customized polarimeter and interferometer. Printing LC droplets with different internal configurations of the LC director on treated glass substrates is demonstrated to achieve different structured light fields.

Additionally, the chapter introduces the experimental process and details employed in this study, showing that complex light fields with different structured polarization can be achieved by manipulating droplets with different internal director profiles. Simulations of these complex structured light fields are also presented to verify the experimental results, providing a comparison between theory and experiment.

In the final research chapter, Chapter 6, a novel design of a phase and polarization sensor is presented using printed LC droplet arrays. The chapter first discusses the mechanism for measuring the polarization based on a Stokes polarimeter, and phase measurements based on the Shack-Hartmann Wavefront Sensor (SHWS) configuration. The chapter then describes how the printed devices are fabricated and how they can be used as either a polarimeter or a SHWS, presenting experimental results of the polarization field and phase separately.

Lastly, Chapter 7 summarizes the research presented in the thesis on the development of printed LC droplets and their ability to optically modulate and detect the phase and polarization characteristics of light. The creation of complex structured light as well as new phase and polarization sensors is discussed, and consideration is given to future developments using alternative LC phases. The chapter ends with a perspective on future research directions, such as extending the ability of the light field sensor to measure wavelengths to enable a full vectorial light field analysis using a single device.

Chapter 2

Background

"Nature uses only the longest threads to weave her patterns, so each small piece of her fabric reveals the organization of the entire tapestry."

Richard Feynman

2 Background

2.1 Liquid Crystals

Liquid crystals (LCs) constitute a distinct state of matter, known as a mesophase[32], that is positioned between the crystalline solid and isotropic liquid phases. LC molecules exhibit fluid-like flow while retaining the ability to self-organize into complex periodic structures at the molecular scale, depending on the specific mesophase[33]. The anisotropic molecular structure of LCs is fundamental to their unique properties, resulting in directional dependence in various physical characteristics such as refractive index and dielectric permittivity. This ordered arrangement renders LCs highly valuable for a wide range of scientific and technological applications[34, 35].

The discovery of LCs dates back to 1888, when Austrian botanist Friedrich Reinitzer observed unusual temperature-dependent optical properties in cholesteryl benzoate[36]. German physicist Otto Lehmann confirmed these observations using polarizing microscopy, identifying a new thermodynamic state of matter[37]. Although initially receiving limited attention, the field advanced significantly in the mid-20th century through the synthesis of novel LC molecules and a deeper understanding of their structure-property relationships[38]. These advancements were recognized, in part in 1991 when Pierre-Gilles de Gennes was awarded the Nobel Prize in Physics for his contributions to LCs and related soft matter systems[39], establishing the foundation for

modern LC theory[40].

While LCs dominated the display market for decades, particularly through LCD technology[41-43], the rise of advanced display systems, such as OLED and micro-LED, has shifted research focus toward exploring novel applications of LCs[18, 44, 45]. This shift has encouraged the academic community to investigate the integration of LCs with emerging technologies. One such avenue is the use of LCs in additive manufacturing techniques, such as inkjet printing, to fabricate structures with tailored optical properties.

LCs are primarily classified into two categories: thermotropic and lyotropic. Thermotropic LCs undergo phase transitions solely in response to temperature changes, whereas lyotropic LCs require specific concentration conditions to induce phase transitions, with temperature acting as an additional modulating factor[46]. This thesis focuses on thermotropic LCs for their ability to form ordered phases and exhibit distinctive optical properties, which are leveraged to investigate the fabrication of LC droplets and their optical applications using printing techniques.

2.2 Liquid Crystal Phases

Thermotropic LCs undergo phase transitions as the temperature changes[47], significantly altering their molecular arrangement and order, as shown in **Figure 2.1**. Below their melting point, they exist as crystalline solids, characterized by long-range positional and orientational order. Upon heating, they transition into the nematic phase,

where the molecules lose positional order but maintain a preferred orientation[48]. Further increasing the temperature beyond the clearing point results in the isotropic phase, where both positional and orientational order are lost, and the material behaves as a conventional liquid. Additional mesophases, such as the smectic phases with layered molecular arrangements, can also occur; however, these are not relevant to the scope of this thesis and are therefore not discussed further.

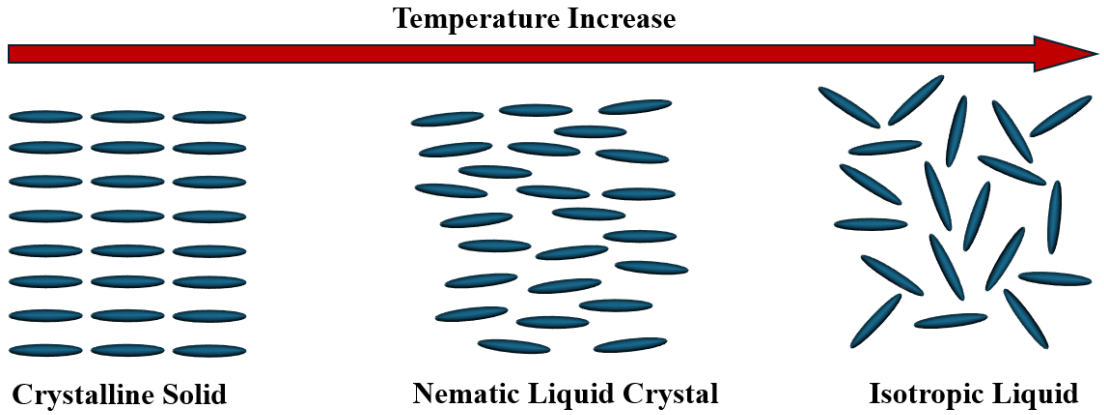


Figure 2.1 Effect of temperature on the phases of a thermotropic LC. At low temperatures, the material exists in the crystalline solid phase, exhibiting both positional and orientational order. As the temperature increases, it transitions to the nematic LC phase, which retains orientational order but lacks positional order. At higher temperatures, the material enters the isotropic liquid phase, where neither positional nor orientational order is present.

2.2.1 Nematic phase

The nematic phase, the primary LC mesophase discussed in this thesis, is characterized by long-range orientational order without positional order. The term "nematic" originates from the Greek word *nematos*, meaning "thread-like," reflecting the appearance often observed under a polarizing microscope. In the nematic phase, rod-like molecules tend to align their long axes along a preferred direction. This preferred

orientation is represented by a unit vector, $\hat{n}$, referred to as the director[49, 50], which describes the average molecular alignment within a given volume of the material (**Figure 2.2**(a)).

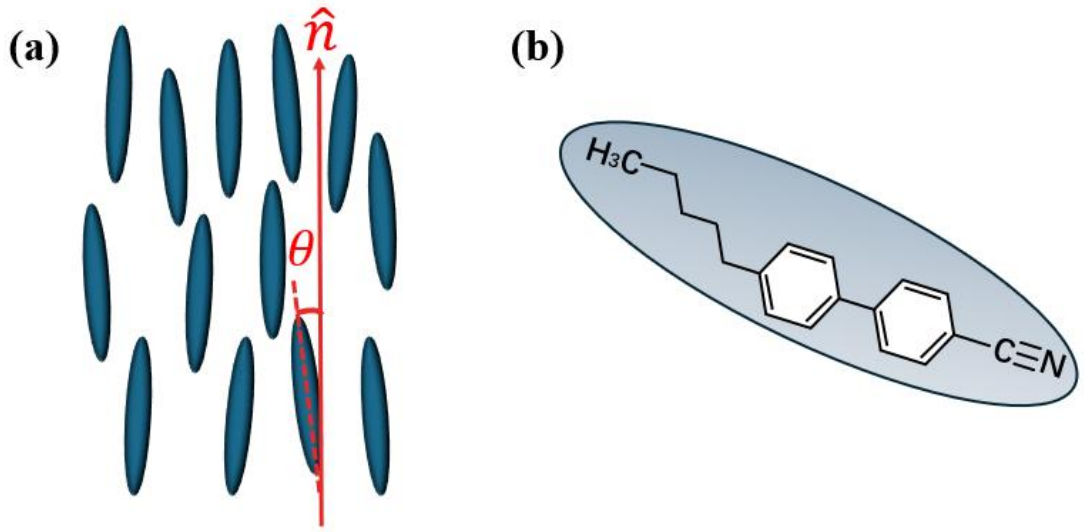


Figure 2.2 (a) Schematic representation of the nematic phase, where rod-like LC molecules exhibit long-range orientational order, aligning on average along a common direction denoted by the director $\hat{n}$. The angle θ indicates the deviation of individual molecules from the director. (b) The molecular structure of 4-cyano-4'-pentylbiphenyl (5CB), a commonly studied thermotropic nematic LC, highlighting its rod-like geometry and rigid aromatic core essential for liquid crystalline behaviour.

The degree of orientational order in the nematic phase is quantified using the scalar order parameter S, defined as:

$$S = \frac{1}{2}\langle 3\cos^2\theta - 1\rangle, \tag{2.1}$$

where θ is the angle between the long axis of an individual molecule and the director $\hat{n}$, and the angular brackets indicate an average over all the molecules in the volume[51]. When all molecules are perfectly aligned ($\theta = 0$), $S = 1$, as would occur at absolute zero. In the isotropic phase, where molecules are randomly oriented, $S = 0$[52]. In

nematic LCs, the order parameter typically ranges from 0.3 to 0.8, depending on the material and temperature[53].

Temperature plays a crucial role in determining the nematic phase's degree of orientational order. As the temperature rises, the intensified thermal motion of the molecules makes it harder for them to maintain alignment along the director, leading to a gradual decrease in the scalar order parameter, S. At the clearing point (T_c), the nematic phase transitions into the isotropic liquid phase, characterized by a complete loss of orientational order.

The molecular structure of nematic LCs often features rigid aromatic cores, such as phenyl rings, linked by flexible hydrocarbon chains. This anisotropy in molecular shape underpins their unique optical and dielectric properties. For example, the nematic LC molecule 5CB (4-cyano-4'-pentylbiphenyl) has an elongated shape that can be approximated as a prolate ellipsoid, as shown in Figure 2.2(b)[54]. Such properties allow nematic LCs to self-organize and respond to external fields, making them suitable for a wide range of optoelectronic applications.

2.2.2 Chiral nematic phase

The chiral nematic (CLC) phase, also known as the cholesteric phase, was first discovered in cholesterol esters[55]. Like the nematic phase, CLCs exhibit long-range orientational order but lack positional order. However, the distinctive feature of the CLC phase is its helical structure, where the director ($\hat{n}$), representing the average

molecular orientation, rotates periodically along an axis perpendicular to itself (**Figure 2.3**). The periodicity of this rotation is defined by the helical pitch (P), which corresponds to the distance required for the director to complete a full $360°$ rotation[56].

The helical arrangement in CLCs can be induced by introducing a chiral dopant into a nematic LC. The concentration (c) of the chiral dopant determines the pitch of the helix, allowing precise control of its periodicity. Additionally, the handedness of the chiral dopant dictates whether the director rotates in a right-handed (clockwise) or left-handed (anticlockwise) sense, resulting in a corresponding helical structure. To quantify the relationship between the dopant concentration and the resulting pitch, the helical twisting power (HTP) is used. The HTP (β) is defined as the proportionality constant between the reciprocal pitch and the dopant concentration. This relationship is mathematically expressed as[39, 57]:

$$\beta = \frac{1}{cP} \tag{2.2}$$

where c represents the concentration of the chiral dopant and P is the helical pitch. A higher HTP value indicates that a smaller pitch can be achieved for a given dopant concentration.

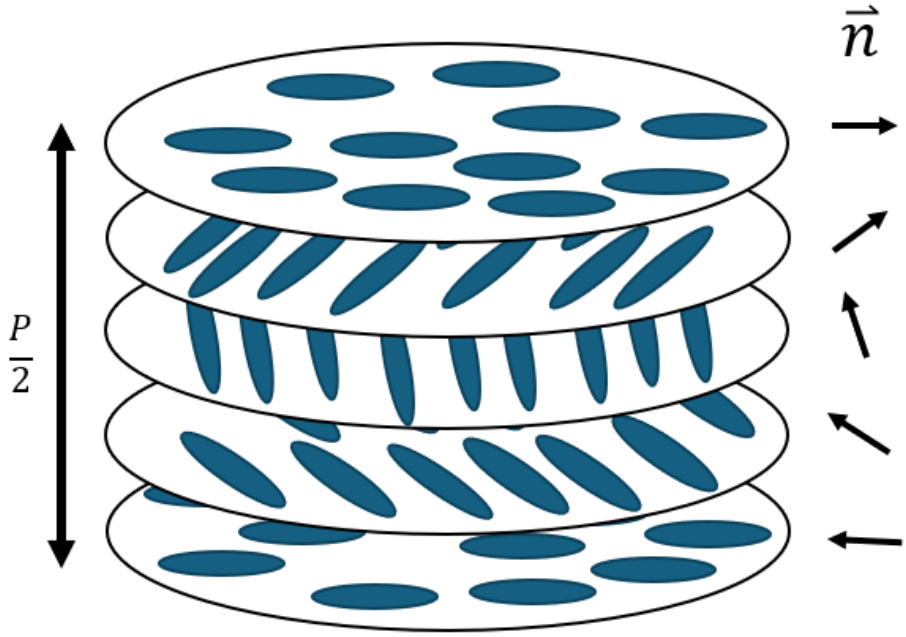


Figure 2.3 Configuration of a left-handed chiral nematic LC phase with half pitch.

2.3 Physical Properties of the Nematic Phase

Nematic LCs are typically represented as rod-like molecules, characterized by distinct long and short molecular axes. As a result, their physical properties differ depending on whether these properties are measured along the long axis or the short axis. In the nematic phase, the molecules align on average along a preferred direction, defined by the director ($\hat{n}$). To model their behaviour, the nematic phase is treated as a continuum, with its physical properties characterized relative to their orientation, either parallel or perpendicular to the director. This intrinsic anisotropy is fundamental to the unique physical properties of nematic LCs.

2.3.1 Alignment

The alignment of LC molecules on a substrate plays a critical role in determining the

performance of LC-based devices. The LC director tends to orient in a specific direction at a surface or interface, and this preferred orientation is referred to as the "easy axis"[58]. The alignment process is governed by a balance between surface interactions, elastic forces, and anchoring energies, all of which influence the LC's orientational order[59]. Different alignment strategies are employed depending on the application, with the three most common being planar, homeotropic, and tilted alignment.

In planar alignment, the LC director aligns parallel to the substrate surface, often with a slight tilt referred to as the pretilt angle. The rubbing process used to create this alignment forms microgrooves and aligns the LC molecules in the desired direction. The grooves serve as anchoring sites that guide the alignment of LC molecules, minimizing distortions and elastic energy in the bulk LC phase. This promotes alignment along the groove direction[60]. For homeotropic alignment, the LC director orients perpendicular to the substrate surface. This is typically achieved by coating the substrate with chemical surfactants, such as lecithin, which is frequently used for the printing substrate in this thesis. Tilted alignment orients the LC director at an intermediate angle relative to the substrate, typically between homeotropic (perpendicular) and planar (parallel) configurations. This type of alignment is often achieved by modifying the rubbing process or using advanced techniques like photoalignment[61].

The alignment of the LC director on a substrate is governed by the anchoring energy,

which describes how the LC director $\hat{n}$ interacts with the surface to achieve a preferred orientation. The surface alignment can be described by the surface free energy density (f_s), which accounts for deviations of the LC director from the easy axis. This energy density is given by[62]:

$$f_s = \frac{1}{2} W sin^2(\theta - \theta_0), \tag{2.3}$$

where f_s is the surface free energy per unit area, W is the anchoring strength, θ is the actual alignment angle of the LC director, and θ_0 is the angle of the easy axis. When the LC director deviates from the easy axis ($\theta \neq \theta_0$), the surface free energy increases. This energy penalty encourages the LC director to align with the easy axis, minimizing the system's overall free energy.

2.3.2 Elastic energy

In nematic LCs, the director $\hat{n}$ typically aligns uniformly in the absence of external forces or constraints, minimizing the free energy of the system[63]. This uniform alignment represents the equilibrium state, where the system is in thermodynamic stability. However, external stimuli such as electric or magnetic fields, mechanical stress, or competing boundary conditions disrupt this equilibrium, introducing distortions in the director field. These distortions increase the system's internal energy, described as elastic energy. The energy required to deform the uniform director field depends on one or a combination of three fundamental deformation types: splay, twist, and bend (**Figure 2.4**).

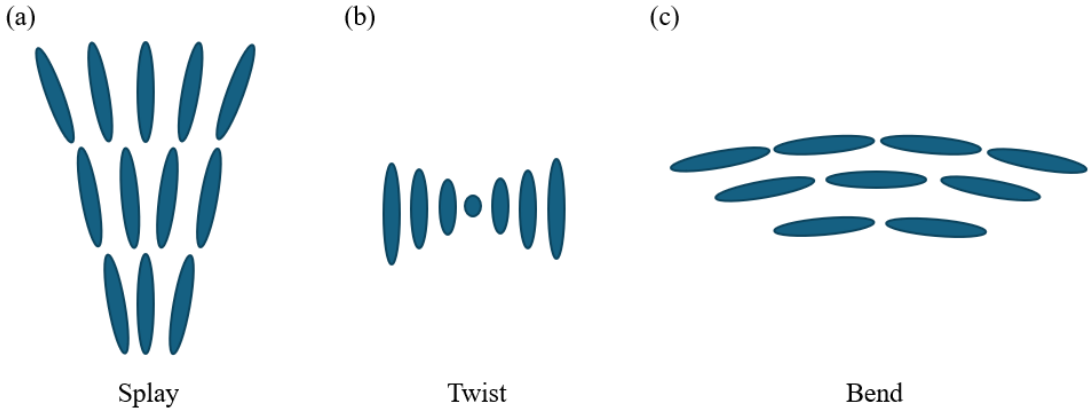


Figure 2.4 Three fundamental types of distortion that generate elastic energy: (a) Splay, (b) Twist, and (c) Bend.

The elastic energy can be considered as analogous to the energy stored in a spring under deformation. Fundamentally, this can be expressed as:

$$U = \frac{1}{2} K \Delta x^2, \tag{2.4}$$

where K is the elastic constant of the material and Δx represents the distance of the displacement. The elastic energy for the three types of LC deformation can be described by the deformation of the director $\hat{n}$. Therefore, the Δx term for splay, twist, and bend can be replaced with $\nabla \cdot \hat{n}$, $\hat{n} \cdot (\nabla \times \hat{n})$, and $\hat{n} \times (\nabla \times \hat{n})$, respectively. The elastic energy density associated with these distortions is described by the Frank-Oseen continuum theory. It combines the contributions from splay, twist, and bend into a single expression for the total elastic energy density[64, 65]:

$$f_{elastic}(\hat{n}) = \frac{1}{2} K_1 [\nabla \cdot \hat{n}]^2 + \frac{1}{2} K_2 [\hat{n} \cdot (\nabla \times \hat{n})]^2 + \frac{1}{2} K_3 [\hat{n} \times (\nabla \times \hat{n})]^2 \tag{2.5}$$

where K_1, K_2, K_3 are elastic constants for splay, twist, and bend, respectively. These constants, typically measured in piconewtons (pN), represent the energetic penalty

associated with each type of deformation.

To simplify calculations, it is common to assume $K_1 = K_2 = K_3 = K$, resulting in the one-constant approximation of the elastic energy density[66]:

$$f_{elastic}(\hat{n}) = \frac{1}{2}K[(\nabla \cdot \hat{n})^2 + (\nabla \times \hat{n})^2]. \quad (2.6)$$

This approximation is particularly useful when detailed measurements of individual elastic constants are unavailable or when the specific contributions of splay, twist, and bend are not critical to the analysis.

2.3.3 Dielectric permittivity

In a dielectric material, the molecular dipole can originate from permanent dipole moments of the molecules. In the absence of an electric field ($\vec{E}$), these dipoles may be randomly oriented, but the application of $\vec{E}$ tends to align them along the field direction, leading to polarization. The electric displacement field $\vec{D}$ is then given by,

$$\vec{D} = \varepsilon_0 \vec{E} + \vec{P}, \quad (2.7)$$

where ε_0 is vacuum permittivity, and $\vec{P}$ is the polarization density, which can be written as

$$\vec{P} = \varepsilon_0 \chi \vec{E}, \quad (2.8)$$

where χ is the electric susceptibility of the material. Inserting the expression for $\vec{P}$ Eq. (2.8) into Eq. (2.7) we get

$$\vec{D} = \varepsilon_0(1 + \chi)\vec{E} = \varepsilon \vec{E}, \quad (2.9)$$

where $\varepsilon = \varepsilon_0 \varepsilon_r$ and $\varepsilon_r = 1 + \chi$ is the relative permittivity.

In anisotropic materials such as nematic LCs, dielectric properties depend on direction $\hat{n}$. The dielectric tensor $\bar{\bar{\varepsilon}}$ characterizes this anisotropy. For a uniaxial nematic LC with the director aligned along the z-axis, the tensor is

$$\bar{\bar{\varepsilon}} = \begin{pmatrix} \varepsilon_\perp & 0 & 0 \\ 0 & \varepsilon_\perp & 0 \\ 0 & 0 & \varepsilon_\parallel \end{pmatrix}, \tag{2.10}$$

where $\varepsilon_\perp$ and $\varepsilon_\parallel$ are the dielectric permittivity perpendicular and parallel to the director, respectively. The dielectric anisotropy is defined as $\Delta\varepsilon = \varepsilon_\parallel - \varepsilon_\perp$.

To express the electric displacement field D explicitly, we start from

$$\vec{D} = \varepsilon_0 \bar{\bar{\varepsilon}} \vec{E} = \varepsilon_0 \begin{pmatrix} \varepsilon_\perp & 0 & 0 \\ 0 & \varepsilon_\perp & 0 \\ 0 & 0 & \varepsilon_\parallel \end{pmatrix} \begin{pmatrix} E_x \\ E_y \\ E_z \end{pmatrix} = \varepsilon_0 \varepsilon_\perp \begin{pmatrix} E_x \\ E_y \\ E_z \end{pmatrix} + \varepsilon_0 (\varepsilon_\parallel - \varepsilon_\perp) \begin{pmatrix} 0 \\ 0 \\ E_z \end{pmatrix}. \tag{2.11}$$

Assuming that the director $\hat{n}$ is along the z-axis ($\hat{n} = [0, 0, 1]$) and that $\left(\hat{n} \cdot \vec{E}\right) = E_z$. Then, the displacement field simplifies to

$$\vec{D} = \varepsilon_0 \varepsilon_\perp \vec{E} + \varepsilon_0 \Delta\varepsilon \left(\hat{n} \cdot \vec{E}\right) \hat{n}, \tag{2.12}$$

This expression indicates that the displacement field depends on both the magnitude and direction of the electric field relative to the director. The dielectric constants $\varepsilon_\perp$ and $\varepsilon_\parallel$ are strongly dependent on temperature and the frequency of the applied electric field.

2.3.4 Optical properties of nematic phase

The dielectric permittivity of a material varies with the frequency of the applied electric

field[67]. For example, water exhibits a relative dielectric permittivity of approximately 80 at low frequencies (below 10^8Hz) at room temperature[68, 69]. However, this value decreases to about 1.78 at optical frequencies ($10^{14} - 10^{15}$Hz) because permanent molecular dipoles cannot respond to electric fields oscillating at such high frequencies[70]. Consequently, the refractive index of a material also depends on the frequency of the incident light.

Nematic LCs display anisotropic permittivity at optical frequencies due to the alignment of their molecules along the director. The two principal dielectric permittivity (parallel and perpendicular to the director) are defined as $\varepsilon_\perp$ and $\varepsilon_\parallel$, respectively. The dielectric anisotropy is defined as $\Delta\varepsilon = \varepsilon_\parallel - \varepsilon_\perp$ [71]. At optical frequencies, the refractive index n is related to the relative optical dielectric permittivity ε_r by:

$$n = \sqrt{\varepsilon_r}. \tag{2.13}$$

Due to their anisotropic structure, nematic LCs exhibit birefringence (**Figure 2.5**), where the refractive index varies depending on the polarization and propagation direction of light relative to the director. The birefringence Δn is defined as:

$$\Delta n = n_e - n_o, \tag{2.14}$$

where n_o is the ordinary refractive index for light polarized perpendicular to the optic axis, and n_e is the extraordinary refractive index for light polarized parallel to the optic axis. Here, the optic axis is explicitly aligned with the director. When light propagates through a nematic LC at an angle φ with respect to the optic axis, the effective

refractive index n_e' experienced by the light is given by:

$$n_e' = \sqrt{\frac{{n_e}^2 {n_o}^2}{{n_e}^2 \cos^2 \varphi + {n_o}^2 \sin^2 \varphi}}. \tag{2.15}$$

This expression shows that the propagation speed of light in a nematic LC depends on the angle φ due to the anisotropic refractive indices.

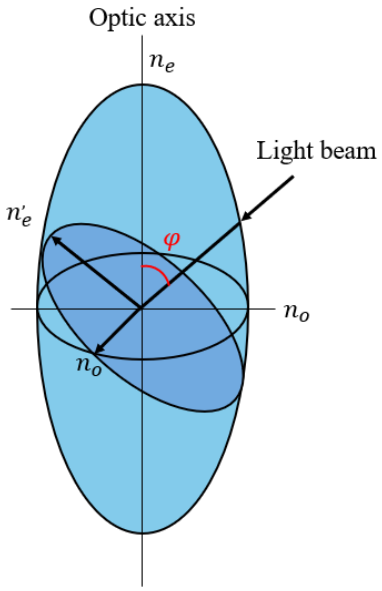


Figure 2.5 Schematic diagram of a light beam propagating at angle φ relative to the optical indicatrix.

The birefringence causes a phase difference between the ordinary and extraordinary rays as they propagate through the LC, resulting in optical retardation expressed as:

$$\delta = \frac{2\pi \Delta n d}{\lambda}, \tag{2.16}$$

where δ is the phase retardation, Δn is the birefringence, d is the cell gap, and λ is the wavelength of the incident light.

Observing LC samples placed between crossed polarizers is a frequently used

technique to investigate their optical properties in this thesis. In a polarized optical microscope, two polarizers — the polarizer and the analyser — are placed on either side of the LC sample. The orientation of the polarizer and the analyser should be orthogonal to ensure that the light beam is fully blocked in the absence of the LC sample. However, when the LC sample is introduced, it acts as a waveplate due to its birefringence, altering the state of polarisation (SoP) of the light and allowing some light to pass through the analyser. The transmitted intensity T of light passing through the LC sample between crossed polarizers is given by:

$$T = sin^2(2\chi)sin^2\left(\frac{\pi\Delta nd}{\lambda}\right), \tag{2.17}$$

where χ is the angle between the rubbing direction (LC director) and the orientation of the polarizer, Δn is the birefringence, d is the cell gap, and λ is the wavelength. Maximum transmission occurs when $\chi = 45^{\circ}$ and the optical retardation satisfies $\frac{\pi\Delta nd}{\lambda} = \frac{\pi}{2} + k\pi\ (k = 0, 1, 2, \dots)$. Transmission drops to zero, however, when $\chi = 0^{\circ}$ or 90°, or when the optical retardation is $\frac{\pi\Delta nd}{\lambda} = k\pi\ (k = 0, 1, 2, \dots)$.

Applying a voltage to the nematic LC alters the orientation of the director thereby changing the effective birefringence Δn as the director tilts in response to the electric field. This voltage-controlled modulation of the birefringence is fundamental to the operation of LCDs, allowing precise control of light transmission through changes in applied voltage. **Figure 2.6** illustrates a typical plot of light transmission as a function of applied voltage for a nematic LC cell placed between crossed polarizers.

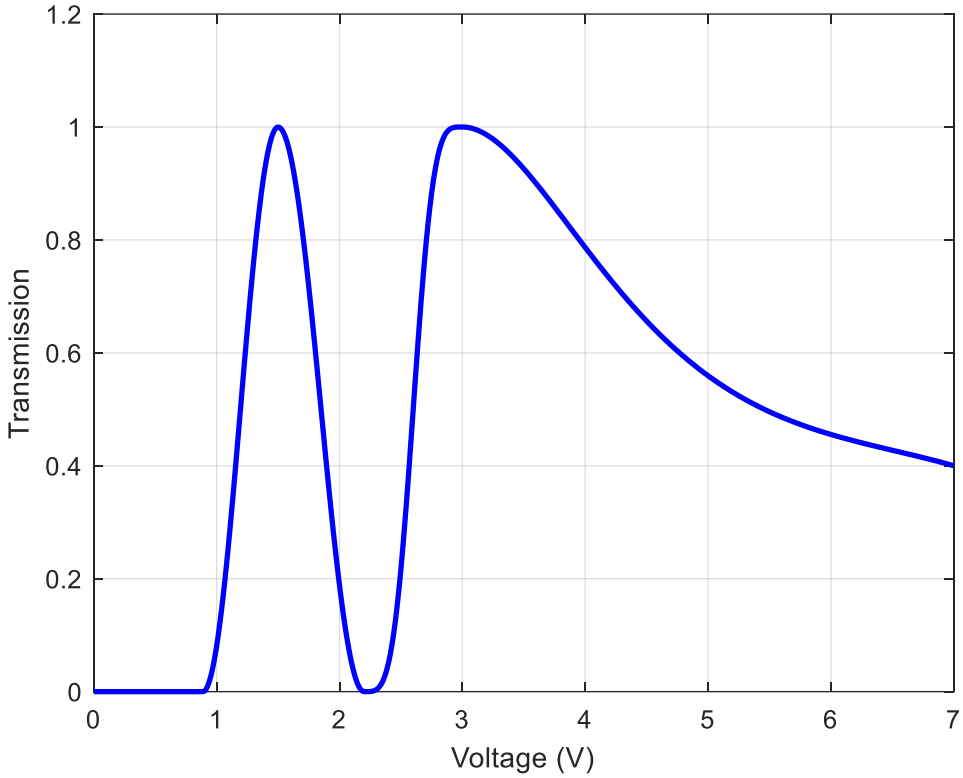


Figure 2.6 Transmission of light through a nematic LC cell (placed between polarizers with their transmission axes crossed) plotted as a function of the voltage applied to the LC.

2.4 Optical Properties of the Chiral Nematic Phase

When light propagates along the helical axis of a CLC, selective Bragg reflection of circularly polarized light occurs if the pitch P of the helix is of the order of the wavelength of the light. This helical structure acts as a one-dimensional photonic crystal, reflecting specific wavelengths that satisfy the Bragg condition[72, 73].

The circularly polarized component of light that is reflected has the same handedness as the helical structure of the LC, while the component with opposite handedness is transmitted. Since linearly polarized light can be considered as an equal superposition of left- and right-handed circularly polarized waves, the maximum

intensity of the reflected light is half that of the incident light under ideal conditions[74]. The wavelength range of the bandgap (reflection band) is determined by the ordinary (n_o) and extraordinary (n_e) refractive indices of the LC in addition to the pitch. The wavelength of the band-edges can then be described as

$$\lambda_L = n_e P, \tag{2.18}$$

$$\lambda_S = n_o P, \tag{2.19}$$

where n_e is the extraordinary refractive index (parallel to the director) and n_o is the ordinary refractive index (perpendicular to the director). λ_S corresponds to the short-wavelength band edge, and λ_L corresponds to the long-wavelength band edge of the reflection band. These relationships indicate that the position of the band edges can be controlled by adjusting either the refractive indices (n_e and n_o) or the pitch P of the helix. The bandwidth $\Delta\lambda$ of the reflection band is the difference between the long and short wavelength edges and can be calculated by:

$$\Delta\lambda = \lambda_L - \lambda_S = (n_e - n_o)P. \tag{2.20}$$

This expression shows that the bandwidth can be adjusted by altering the birefringence $\Delta n = (n_e - n_o)$ or the pitch P.

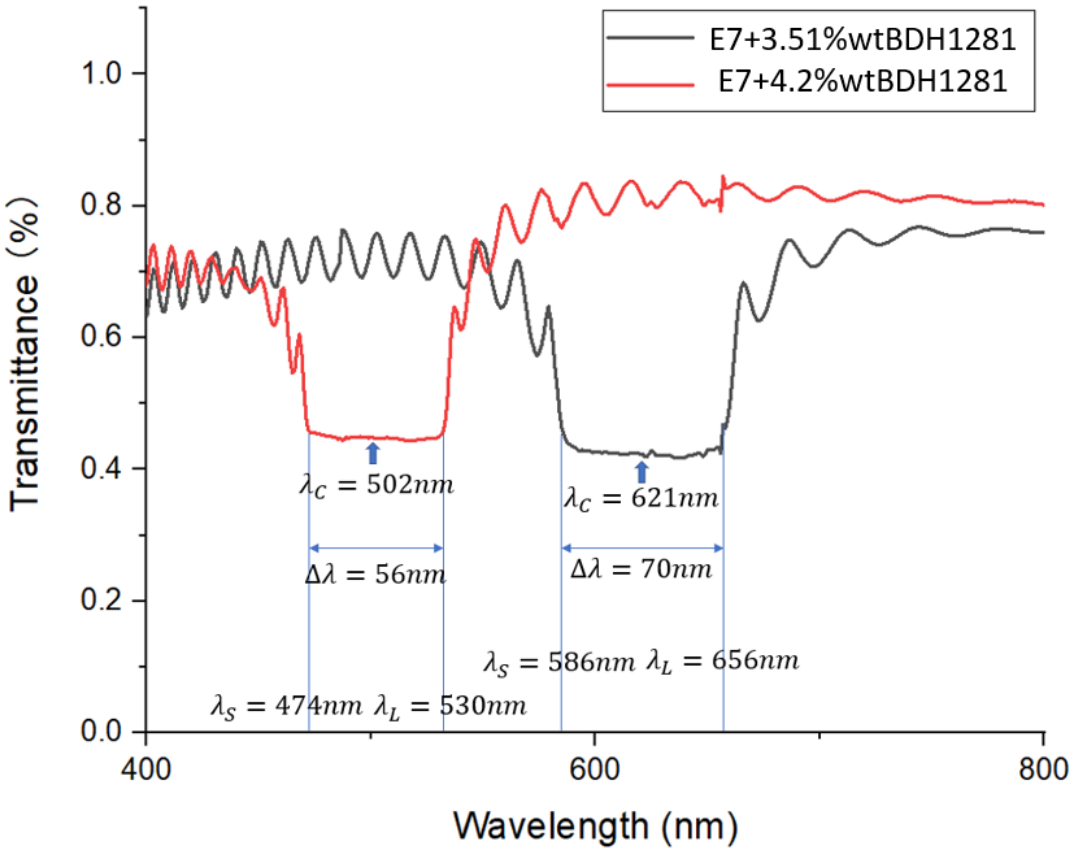


Figure 2.7 The transmission spectrum for white light of a CLC. The two spectra show the effect of the chiral dopant (BDH1281, Merck) concentration on the position of the photonic bandgap of a CLC. The transmittance of the CLC mixtures: $E7 + 3.5$ wt.% BDH1281 (black line) and $E7 + 4.2$ wt.% BDH1281 (red line). The thickness of the LC layer in each case was 5 μm and these results were obtained using a UV-Vis spectrometer at a temperature of 20℃.

The pitch P is highly dependent on the concentration of the chiral dopant in the nematic LC. **Figure 2.7** provides an example of the transmission spectrum for white light propagating along the helical axis of a CLC, the bandgap with a higher concentration of chiral dopant is located at a shorter central wavelength and its bandwidth is also narrower. This dependence allows for precise tuning of the reflection band across different wavelengths, which is valuable for applications such as tunable optical filters and reflective displays.

2.5 Printing Liquid Crystalline Materials

Combining printing technologies with LC materials has opened new avenues for creating advanced thin-film optical devices with novel functionalities. In our research group, a bespoke DoD inkjet printer was first developed by Dr Ellis Parry for fabricating LC droplets. Using this system, printed LC droplets were generated that were subsequently shown to function as microlenses with tunable focal lengths, achieved by varying the ambient temperature[29]. Additionally, a study was carried out to understand how the substrate conditions influence the alignment of the LC director in printed droplets, demonstrating that partially wettable polymer substrates can induce radial alignment of the LC director while maintaining uniform droplet boundaries[75].

Building on this foundation, further work was carried out to realise electrically tunable LC microlenses. By using DoD printing to deposit LC droplets between in-plane indium tin oxide (ITO) electrodes, Kamal *et al.* developed bifocal microlenses whose focal lengths could be dynamically switched by adjusting the applied voltage[76]. This innovation highlighted the potential of LC printing technologies for tunable optical devices. Smart windows represent another promising application of printed LC materials. For example, printed polymer-dispersed liquid crystal (PDLC) films have been used to create visually striking patterns and logos that switch between opaque and transparent states when a voltage is applied[77].

More recently, Mengmeng Li and colleagues demonstrated printed polymer-

stabilized chiral nematic liquid crystal (PSCLC) films. These smart windows can operate in both conventional modes (switching from scattering to transparent) and reverse modes (switching from transparent to scattering) under an electric field[78]. Beyond DoD inkjet printing, our group has also explored electrohydrodynamic (EHD) printing, which enables high-resolution patterning of LCs across a broad range of length scales. This technology has been instrumental for this thesis, particularly for applications requiring precise droplet deposition and control.

Inkjet printing has also been employed in diverse LC applications, including the fabrication of LC microlaser arrays[79], sensors integrating printed LC droplets into microfluidic channels for protein detection[80], and reversible photo-switchable fluorescent LC nanoparticles for information encryption and anti-counterfeiting purposes[81]. In recent years, research groups have been interested in the development and characterisation of LC droplets, but these are often targeted for use in microfluidic technology rather than being fabricated using printing technology[82-85]. By leveraging the control and scalability of printing techniques, researchers are moving toward realizing advanced optical devices such as lenses, filters, and structured light modulators[20, 86, 87]. These developments align closely with the objectives of this thesis, which emphasizes the role of LC droplets in next-generation optical devices.

2.6 Summary

This chapter has provided the foundation for understanding the printed LCs presented

in this thesis. It explores the key properties of nematic and chiral nematic phases, focusing on their molecular alignment and anisotropic optical and dielectric behaviour. Alignment techniques, essential for directing LC behaviour in devices, are discussed, including methods such as homeotropic alignment, planar alignment and photoalignment. This chapter also covers elastic energy theory, which explains LC deformations under external forces, and the optical properties that arise from their anisotropy. This understanding forms the basis for integrating LCs into advanced manufacturing processes and highlights their potential in creating functional optical devices, such as tunable microlenses and photonic components.

Chapter 3

Experimental Methods

"For want of a nail the shoe was lost; for want of a shoe the horse was lost; and for want of a horse the rider was lost, being overtaken and slain by the enemy, all for want of care about a horse-shoe nail."

Benjamin Franklin

3 Experimental Methods

3.1 Introduction

This chapter outlines the experimental methods used to prepare and study the properties and behaviour of printed LC droplets. The preparation of LC mixtures and the printing substrates is a fundamental step in this research. In addition, the chapter also describes the fabrication of a specialized substrate with which to apply electric fields to LC droplets, enabling the exploration of tunable optical properties.

The method used to examine the internal structural and optical properties of the printed LC droplets is polarized optical microscopy (POM). Additionally, the process for measuring the pitch of CLCs is described in this chapter. In this thesis, two printing techniques are utilized. Inkjet printing allows for the generation of repeatable droplet size and shape, with controlled patterns, while EHD printing enables the deposition of ultra-small volume droplets. The chapter discusses the use of two inkjet printing systems: a commercially available Jetlab-II Microfab system and a bespoke inkjet printing system developed in-house, as well as an EHD printer for higher-resolution droplet deposition. Overall, this chapter provides a comprehensive overview of the experimental procedures used for investigating printed LC droplets in this thesis.

3.2 Sample Preparation

3.2.1 Mixture preparation

At the sample preparation stage, the mixtures used in this study consisted mainly of nematic LCs and chiral dopants. The specific mixtures and their formulations are detailed in the relevant chapter. All mixtures were weighed using a precision balance (Mettler Toledo AB104S) with an accuracy of $0.1\,\mathrm{mg}$. The proportions of all components will be expressed in terms of a concentration by weight (wt.%). When preparing the mixtures, the chiral dopant was weighed first to prevent the powder from attaching to the walls of the glass container. Once the amount of powder was measured, the nematic LC was carefully added to the container. Then, a thermal diffusion method was used to make sure the components were completely mixed. The prepared mixture was then placed in an oven (Townson and Mercer 1445-2) and heated to 80℃ to transition the LC into its isotropic phase, which was necessary for thorough mixing. The mixtures were heated in the oven for several hours to ensure complete mixing. The specific duration and temperature settings for this process are detailed in the relevant chapters.

3.2.2 Substrate preparation

Glass slides must be carefully cleaned before they can be utilised as substrates to carry LC droplets. In order to remove any organic residue, the glass slides were first immersed in acetone for 5 minutes. After this soaking period, the slides were thoroughly

rinsed with deionized water to remove any remaining acetone and impurities. Lastly, a stream of nitrogen gas was used to dry the glass slides, making sure that nothing remains on the surface.

Applying alignment layers to the substrates was the next step after cleaning. There are two main types of alignment layers used: homeotropic and planar. For the homeotropic alignment layer, a lecithin film was applied to the cleaned glass slides using a spin-coating technique. This layer induces a perpendicular alignment of the LC director relative the substrate surface. For the planar alignment layer, a polyvinyl alcohol (PVA) solution was spin-coated onto the glass surface. The PVA layer was dried on the slides by briefly baking them in an oven after spin-coating. The dried PVA layer was then subjected to a mechanical rubbing process, where the surface was carefully rubbed with a specialized cloth. The alignment induced by rubbing is due to the interaction between the LC director and the oriented polymer chains in the PVA layer. However, a significant limitation of this method is that inconsistencies in the rubbing process can lead to non-uniform alignment. When LC droplets are deposited onto a substrate, this may cause the droplets to distort, producing undesired outcomes.

To address this issue, commercially available substrates with pre-treated planar alignment layers, such as those from INSTEC, were preferred. These commercial cells provide more uniform and higher-quality alignment layers. In this thesis, a common practice was to obtain these substrates by carefully splitting INSTEC cells in half,

yielding clean and pre-treated alignment layers that were ready for use.

3.3 Fabrication of In-plane Electrode Substrates

The fabrication of in-plane electrode substrates was essential for applying an electric field to the LC droplets, where the field was parallel to the substrate, thereby enabling tunable optical properties. This design was necessary because when viewed under crossed polarizers, aligning the LC director parallel to the direction of light propagation will result in a completely dark field. This phenomenon occurs because light polarized along the director passes through without altering its state of polarization and is subsequently blocked by the analyser. To achieve more interesting modulation effects, a substrate structure that allows the application of an electric field to the sides of the LC droplets was developed, as illustrated in **Figure 3.1**. The basic principle of this structure was etching a long rectangular region on a glass slide coated with an ITO layer, thereby removing the ITO in this region. LC droplets were then precisely printed into this etched region. Finally, wires were connected to the ITO on either side of the etched region, allowing a voltage to be applied across the LC droplets.

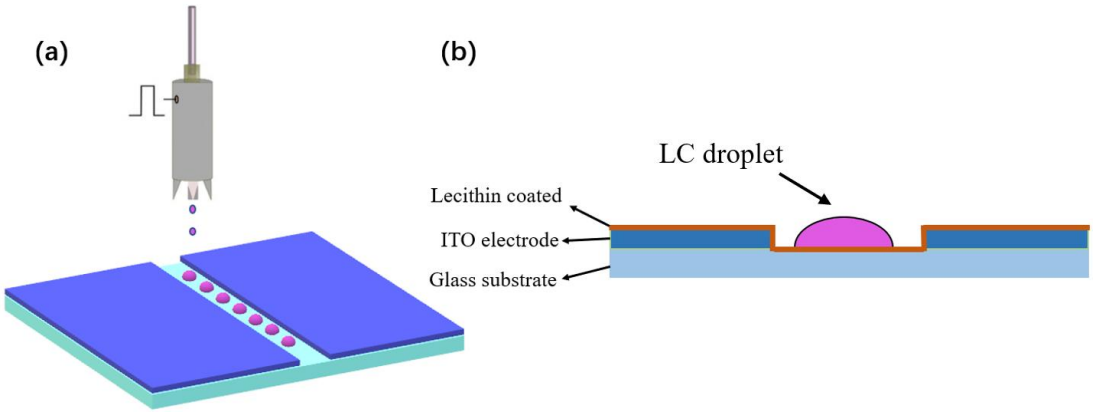


Figure 3.1 Schematic diagram of inkjet printing process. (a) the inkjet printing process for depositing LC droplets onto the in-plane electrode substrate. The printer precisely places droplets within the etched region of the ITO-coated glass slide. (b) a cross-sectional view of the in-plane electrode substrate structure. The substrate consists of a glass slide coated with an ITO electrode, with a long rectangular ITO-free region where LC droplets are deposited. The alignment layer is applied on top of the etched substrate.

The first step in the fabrication process was to identify the side of the glass slide coated with the ITO layer using a multimeter, ensuring accuracy in subsequent steps. The ITO-coated glass slides (20 × 15 mm, Ossila) were then thoroughly cleaned. This involves immersing the slides in deionized water and sonicating for 10 minutes, followed by immersion in isopropyl alcohol (IPA) and sonicating for an additional 10 minutes. After cleaning, the slides are dried using a nitrogen gun to ensure no residues remain.

Next, 2-3 drops of Photoresist (MICROPOSIT S1813 G2) were deposited onto the ITO-coated side of the glass slide. The photoresist was then spin-coated at 3000 rpm for 1 minute, ensuring an even coating without air bubbles that could cause defects. The spin-coated slides were then placed in an oven (Townson and Mercer 1445-2) and heated to 115°C for 1 minute to soft bake the photoresist.

Following the soft bake, a photomask with a $500\ \mu m$ wide and $10\ cm$ long opening is used to cover the ITO glass substrate. The substrate was exposed to ultraviolet (UV) light from a High-power UV LED system (Thorlab, 365nm, CS20K2) at an intensity of $50\ mW/cm^2$ for 60 seconds from a height of $10\ cm$. This exposure ensures the photoresist in the exposed areas is fully developed. The slides are then immersed in MICROPOSIT MF-319 developer and sonicated for 60 seconds to remove the UV-illuminated areas of the photoresist.

To etch the exposed ITO layer, a $1M$ hydrochloric acid (HCl) solution was prepared. The preparation of the $1M$ HCl solution involves careful measurement and mixing of concentrated HCl with deionized water. To prepare $20\ ml$ of 1M HCl solution, first, the volume of concentrated HCl needed was calculated. Given that concentrated HCl has a molarity of $12M$, the volume of concentrated HCl required for a 1M solution can be calculated using the dilution formula:

$$C_1V_1 = C_2V_2, \tag{3.1}$$

where C_1 is the concentration of the concentrated HCl ($12M$), V_1 is the volume of the concentrated HCl needed, C_2 is the desired concentration ($1M$), and V_2 is the final volume of the solution ($20\ ml$). Solving for V_1, we get 1.67 ml. Next, approximately 10 ml of deionized water was poured into a $100\ ml$ volumetric flask. Then, $1.67\ ml$ of concentrated HCl was slowly and carefully added to the water in the volumetric flask, ensuring the acid was added to the water to prevent a violent exothermic reaction. The

flask was then gently swirled to ensure thorough mixing of the acid and water. Finally, deionized water was added to the volumetric flask until the total volume reached exactly 20 ml. The slides are immersed in the prepared HCl solution and placed on a hot-stage set to 40 ℃ for 30 minutes. This process etched away the exposed ITO layer, leaving a long rectangular ITO-free region on the glass slide.

Finally, the slides were rinsed with acetone to remove any remaining photoresist, completing the fabrication of the in-plane electrode substrates (the procedure is summarized in **Figure 3.2**). These substrates allowed for the application of an electric field across the sides of the LC droplets, and dynamically tuning the director of LC droplets.

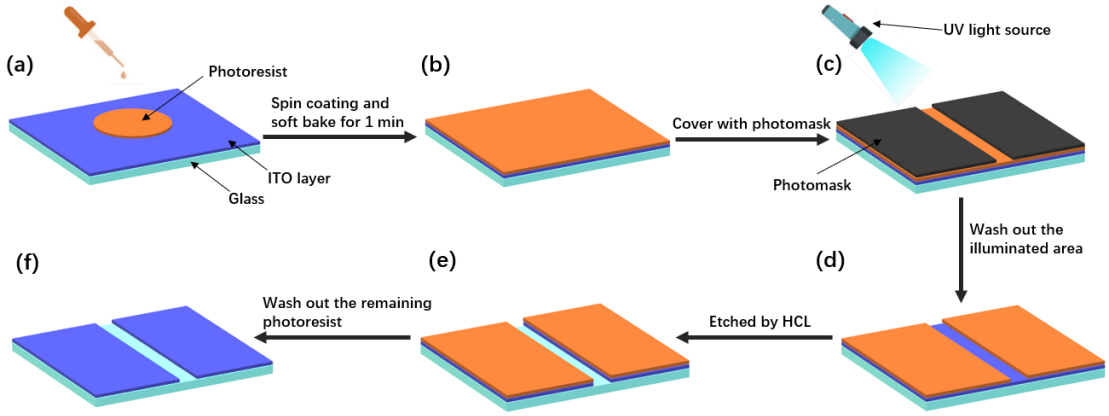


Figure 3.2 A schematic diagram of the fabrication process for the in-plane electrode substrates.

3.4 Polarized Optical Microscopy

In this thesis, a POM (principally using an Olympus BX51 microscope) was used to analyse LC droplets, providing crucial insights into their structural and optical

properties. **Figure 3.3** illustrates the basic arrangement of the optical components. The microscope operates in transmission mode, illuminated by a halogen lamp. Light emitted from the lamp first passes through a rotatable polarizer and then through the sample fixed on a central rotational stage. An objective lens with a specific magnification and numerical aperture collects the light and transmits it through another rotatable analyser before it reaches the eyepiece and/or an imaging camera. A 6-megapixel CCD camera (Retiga 20) attached to the microscope captured high-resolution images of the samples. This camera was connected to a desktop computer, where image resolution, capture, and exposure time parameters could be controlled by the Oculus software. There are two modes of observation for LC samples which are parallel polarization and crossed polarization.

Under parallel polarization conditions, as the polarized light propagates through the LC sample, the polarization direction and phase of the light changes due to the birefringence of the LC droplet. Subsequently, this altered light passes through the analyser, which is parallel to the polarizer, and only the light whose polarization direction aligns with the direction of the analyser pass through. This selective transmission makes different regions of the LC sample appear bright, depending on how the localized region changes the polarization direction of the light. Thus, parallel polarization observation reveals variations in brightness across different regions of the LC sample, which correspond to differences in the local director orientation and birefringence, enhancing the observation of LC properties. Although parallel

polarization observation enhances the visibility of sample characteristics, it often results in low overall contrast due to the alignment of the polarizers, and difficulty in detecting subtle orientation changes and defects.

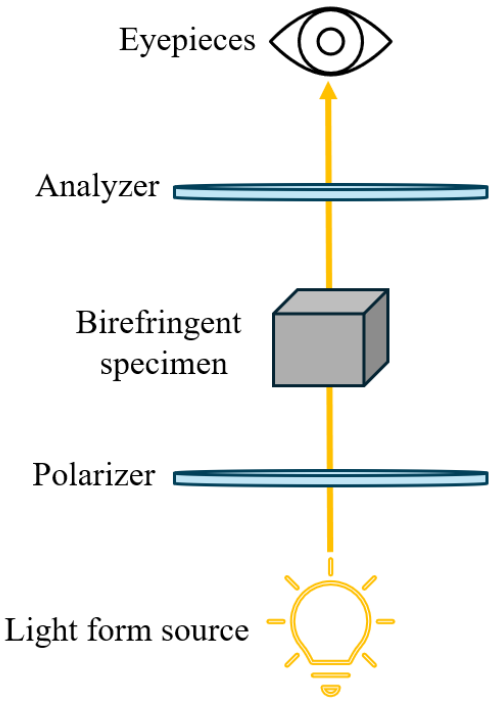


Figure 3.3 Polarized Light Microscope Configuration.

Under crossed polarization conditions, as the light propagates through the LC sample, the birefringent nature of the LC droplets significantly affects the SoP of the light, causing a change in its polarization direction. Since the analyser is perpendicular to the direction of the polarizer, only the light whose polarization direction has changed by passing through the LC sample can pass through. This method effectively highlights polarization changes caused by birefringence effects within the sample. Crossed polarization observation produces high-contrast images, allowing for clear visualization

of anisotropy, domain boundaries, and defects within the LC sample.

3.5 Pitch Measurements

In the study of printed CLC droplets, a primary focus was the investigation of the properties of the droplets formed from mixtures of neat nematic LC mixtures and varying concentrations of chiral dopant. The CLC mixture was fabricated by mixing the nematic LC, E7, and the chiral dopant, R811. E7 is a nematic LC mixture which is composed of 4-cyano-4′4′-n-pentyl-biphenyl (5CB), 4-cyano-4′4′-nheptyl- biphenyl (7CB), 4-cyano-4′4′-n-octyloxy-biphenyl, and 4-cyano-4″4″-n-pentyl-p-terphenyl. It possesses moderate birefringence ($\Delta n \sim 0.22$ at visible wavelengths at room temperature) and a positive dielectric anisotropy[88]. The nematic LC E7 was obtained from Synthon Chemicals Ltd whereas the chiral additive R811 ((R)-2-Octyl 4-[4-(Hexyloxy)benzoyloxy] benzoate), which is a low twisting power chiral additive, was obtained from Merck KGaA. Both components were used without further purification.

To accurately quantify the mixtures, it was essential to measure the pitch of the CLCs. As mentioned in Section 2.2.2, the pitch represents the distance over which the LC director completes a full 360-degree helical twist along the helix axis. By adjusting the concentration of the chiral dopant, the degree of twist can be controlled, thereby precisely tuning the pitch of the LC mixture. In other words, higher concentrations of the chiral dopant result in shorter pitches. This control is crucial for the design and fabrication of LC devices with specific optical properties. For instance, the reflective

properties and the wavelength of light that the LC can selectively reflect are directly related to the pitch. Therefore, before printing CLC droplets, determining the pitch of the mixtures was important.

However, different pitches require different measurement methods due to the physical limitations inherent in each method. Long pitches, which result from lower concentrations of chiral dopant, were measured using a method that relies on pitch jumps in varying cell width (wedge cell). While short pitches, resulting from higher concentrations, require an alternative method that relies on measuring the selective reflection band (Section 2.4).

3.5.1 Short-pitch chiral nematic liquid crystals

Ultraviolet-visible spectrophotometry (UV-Vis) is a technique used for qualitative analysis by irradiating a sample with light in the $200\,\text{nm}$ to $900\,\text{nm}$ wavelength range and analyzing the transmitted or absorbed spectrum. **Figure 3.4** illustrates the structure of a UV-Vis spectrophotometer. The system typically uses a xenon lamp for both UV and visible light. This light is directed into a monochromator, a device that isolates specific wavelengths. The monochromator achieves this by using a diffraction grating to separate the light into its individual wavelengths. By adjusting the grating, the instrument selects a precise wavelength range to pass through to the sample. The selected light then travels through the sample. As the light interacts with the sample, some wavelengths are absorbed, while others pass through. The transmitted light is

captured by a photodetector, which converts the light into an electronic signal. This signal is processed to produce an absorbance or transmittance spectrum, providing detailed information about the sample's optical properties.

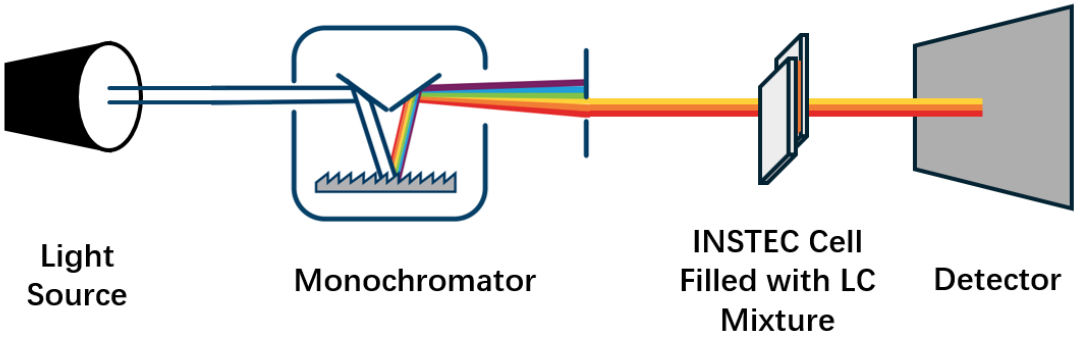


Figure 3.4 Schematic Diagram of a UV-Vis Spectrophotometer.

To measure the pitch of the CLC mixtures, we utilized the Bragg reflection properties of the CLCs. A UV-Vis spectrophotometer (Cary 8455 UV-Vis, Agilent Technologies) was employed to measure the reflection band of each CLC mixture, then the corresponding pitch was calculated according to Eq. (2.20). The specific procedure is as follows: first, the Cary 8455 UV-Vis spectrophotometer was turned on and allowed to warm up for 20 minutes, ensuring that the light source was fully warmed up and emitting the complete spectrum from 200 nm to 900 nm. A baseline measurement was then taken without any sample to check the transmission spectrum, ensuring that all wavelengths from 200 nm to 900 nm were being received. Once the baseline was confirmed, the sample was placed in the spectrophotometer, and the measurement was taken.

Figure 2.7 demonstrates that higher concentrations of the chiral dopant result in reflection bands at shorter wavelengths. The pitch of each CLC mixture was calculated, based on the central wavelength of the reflection band (λ_c) observed in the UV-Vis spectrum. This method's limitation lies in its detection range. When the pitch of the CLC mixture was outside of the detectable range, the method becomes ineffective, and alternative measurement techniques were required.

3.5.2 Long-pitch chiral nematic liquid crystals

For long-pitch CLCs, a reflection band in the visible light spectrum is absent, making it impossible to determine the pitch using a UV-Vis spectrophotometer.

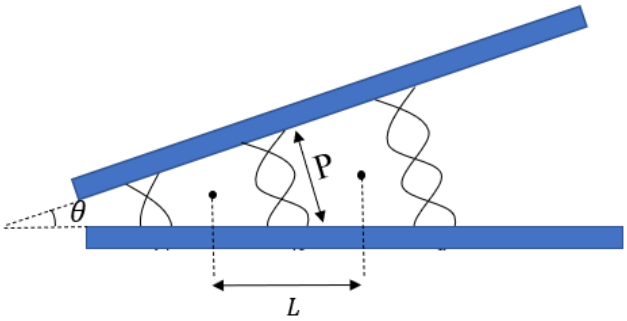


Figure 3.5 An illustration of the Grandjean-Cano wedge cell method. *L* represents the distance between the disclination lines and P is the pitch of the LC mixture.

The Grandjean-Cano wedge method was employed to measure the pitch of long-pitch CLCs. This technique relies on filling CLCs into a wedge cell that was coated with a planar alignment layer. The thickness of the wedge cell varies linearly along its length, creating a gradient of cell thicknesses. As the thickness of the cell changes, the number of helical turns of the CLCs accommodated within the cell also changes. When

the CLCs are confined within the wedge cell, the pitch of the LCs adjusts to fit a half-integer number of pitches within the cell gap, resulting in discrete pitch jumps. These pitch jumps manifest as distinct parallel lines, known as "Grandjean lines," which can be observed using a polarizing optical microscope. By measuring the distance between these Grandjean lines, the pitch of the CLCs can be determined.

The equation for the pitch can be written as

$$P = 2L\tan\theta \tag{3.2}$$

where L is the horizontal distance between the parallel disclination lines observed in the wedge cell and θ is the wedge angle (as illustrated in **Figure 3.5**). Provided that the wedge angle is known, determination of L on a POM enables the pitch to be obtained. There are two methods for determining the wedge angle: one involves using a filter and the other involves filling the wedge cell with a nematic LC.

For the first method, light passing through the wedge cell undergoes multiple reflections between the two substrates, forming interference fringes due to Fabry-Perot interference. These fringes can be described by the equation:

$$2d = m\lambda \tag{3.3}$$

where d is the height difference in cell gap between the black fringes, m is the order of the fringes, and λ is the wavelength of light. When the incident light is filtered to be approximately monochromatic, the interference fringes can be very easily observed.

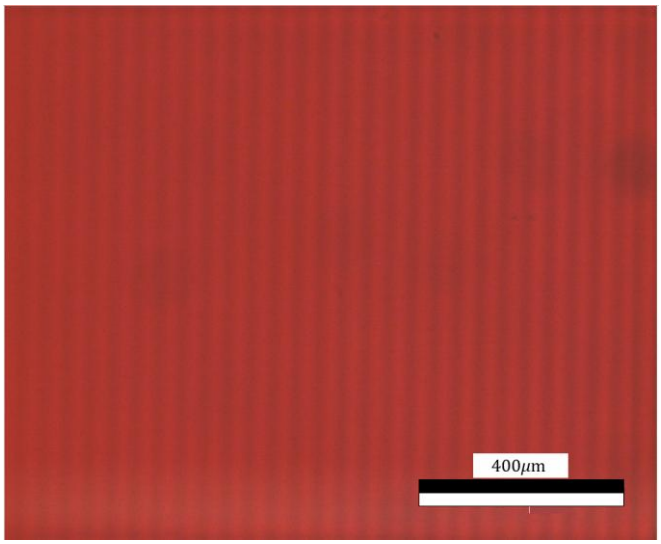


Figure 3.6 Photograph of the fringes formed as a result of light passing through a wedge cell when a white light source was filtered by a red band pass filter ($\lambda = 670 \pm 6$ nm).

Figure 3.6 shows an example of the appearance of a wedge cell using red filtered light. This photograph illustrates the fringes formed as a result of light passing through the wedge cell when a white light source was filtered by a red band pass filter ($\lambda = 670 \pm 6$ nm). In this image, 28 black fringes are visible over a total distance of $1230\mu m$. The Eq. (3.3) indicates that the corresponding difference in thickness over the 28 fringes is 9.38 μm. Therefore, the slope of the wedge cell can be calculated as follows:

$$\tan\theta = \frac{\Delta d}{d'} = \frac{9.38\ \mu\text{m}}{1230\ \mu\text{m}} = 0.00763 \tag{3.4}$$

An alternative method to measure the wedge cell angle involves using the transmission of light through a nematic LC between two crossed polarizers. According to the equation for the transmission of light through a nematic LC between crossed polarizers (Eq. (2.17)), the intensity follows a sinusoidal pattern as the cell gap increases

for certain wavelengths. This means that the light cannot pass through the cell when $\frac{\pi \Delta n d}{\lambda} = \pi, 2\pi, 3\pi, \ldots$

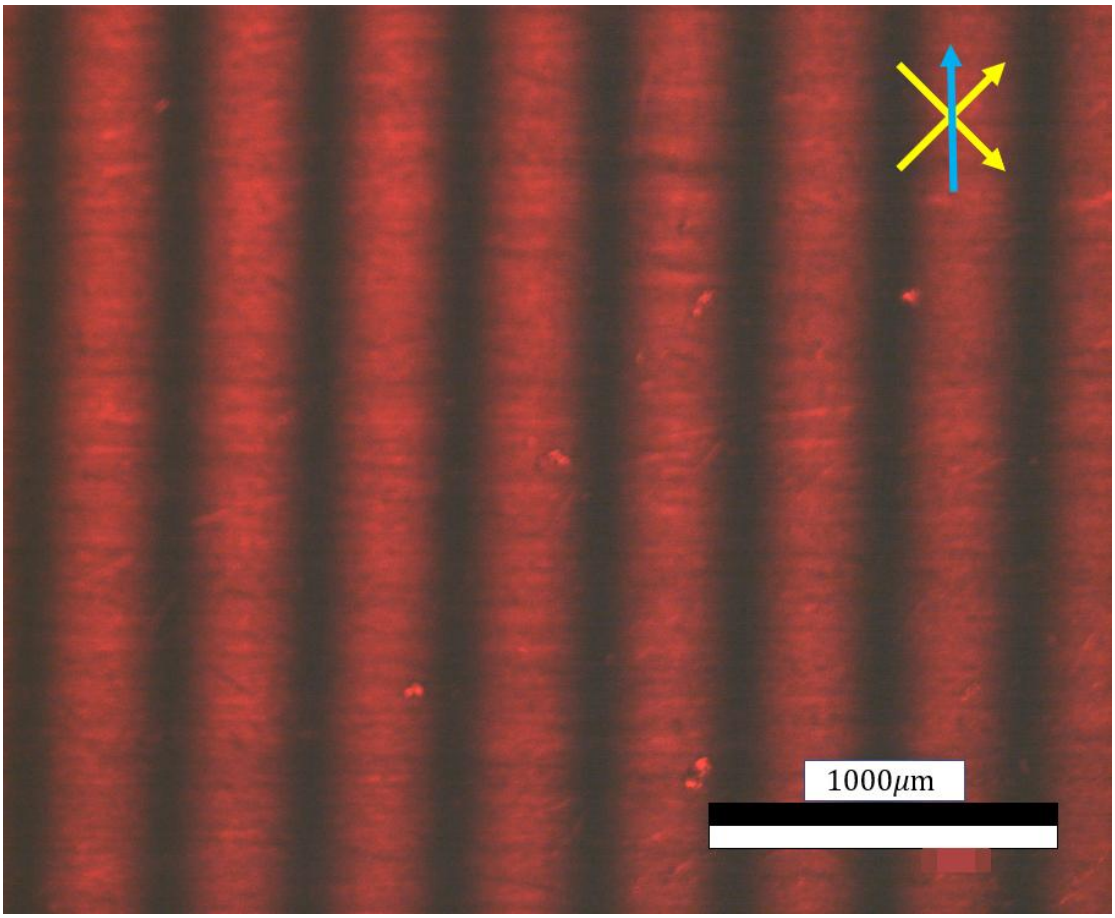


Figure 3.7 A polarized optical microscope image of a wedge cell filled with the nematic LC mixture E7 between crossed polarizers and with a red band pass filter ($\lambda = 670$nm) placed after the light source before the LC. This image was taken at a temperature of 20 ℃. The yellow single-headed arrows represent the polarization direction, and the single headed blue arrow is the alignment of the director.

Figure 3.7 shown above is an example of a POM image of a wedge cell filled with the nematic LC, E7, when viewed using a red band pass filter ($\lambda = 670 \pm 6$ nm) and crossed polarizers. In this image, eight black fringes are observed over a distance of 3150 μm. Each black fringe indicates a point where the intensity of light drops to zero.

The distance between each black fringe in this case is $393.8\ \mu m$. To find the difference in thickness of the cell between each black fringe, the following equation is used:

$$\frac{\Delta n(d+\Delta d)}{\lambda}-\frac{\Delta nd}{\lambda}=1 \tag{3.5}$$

This simplifies to:

$$\frac{\Delta n\Delta d}{\lambda}=1 \tag{3.6}$$

where the wavelength of the light is filtered with the peak at $670\ nm$ (the bandwidth of the filter is about $6\ nm$), the birefringence Δn of the nematic LC at $20\ ℃$ at a wavelength of $670\ nm$ is reported to be $\Delta n = 0.22$[88]. Here the difference in cell thickness between neighbouring regions that are defined by the dark fringes is found to be $\Delta d = 3.19\ \mu m$, which gives a slope of the wedge cell of

$$\tan\theta=\frac{\Delta d}{d'}=\frac{3.19\ \mu m}{393.8\ \mu m}=0.00816 \tag{3.7}$$

where d' is the lateral (horizontal) distance between each black fringe.

Evidently, the result carried out before the cell was filled with the nematic LC ($\tan\theta = 0.00763$) is different from that determined when the wedge cell was filled with a nematic LC ($\tan\theta = 0.00816$). It is believed that the reason for this discrepancy is that the birefringence for E7 taken from the literature was not so reliable. Given that the pre-filled measurement ($\tan\theta = 0.00763$) is independent of the uncertain birefringence value, it is considered more reliable and indicative of the actual wedge

geometry.

Once the slope of the wedge cell has been determined, the cell can be filled with the CLC mixture to measure the pitch. **Figure 3.8** shows a POM image of a wedge cell filled with a chiral nematic mixture consisting of the nematic LC, E7, and the chiral additive ($E7 + 1$ wt. % R811).

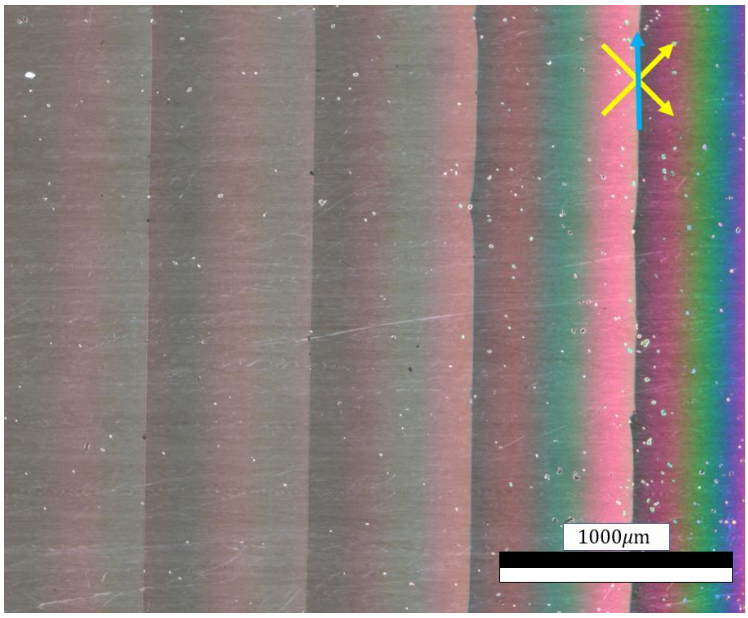


Figure 3.8 Polarized optical microscope image of a wedge cell filled with the CLC mixture ($E7 + 1$ wt. % R811). The yellow single-headed arrows represent the polarization direction, and the single-headed blue arrow is the alignment of the director.

The colourful fringes observed at the edge of the image can be explained by the equation for the transmission of light through a nematic LC between two crossed polarizers (Eq. (2.17)). When the cell thickness is very small, the fringes with maximum intensity for different wavelengths do not overlap with each other. This occurs because each wavelength of light reaches its maximum intensity at different cell thicknesses, resulting in a separation of the fringes into distinct colours. In Figure 3.8, three pitch

jumps are observed over a distance of 2011.5 μm. The pitch of the mixture can be calculated using the following formula:

$$P = 2\text{Ltan}\theta = \frac{2011.5\ \mu m}{3} \times 0.00763 \times 2 = 10.23\ \mu\text{m} \quad (3.8)$$

This result confirms that the pitch is significantly longer than the wavelength of light, classifying the material as a long-pitch CLC mixture.

3.6 Ink-Jet Printing System

In this thesis, two distinct ink-jet printing systems were utilized: the commercially available Jetlab-II from MicroFab Technologies, USA, and a bespoke inkjet printing system. This section introduces the Jetlab-II system, which is a bench-top printing station known for its high positional accuracy and repeatability in depositing small volumes of fluid.

3.6.1 MicroFab Jetlab - II

The Jetlab-II system provides precise and repeatable deposition capabilities, making it suitable for printing larger grids of droplets with high accuracy. It can print over an area of $200 \times 200\ \text{mm}^2$ with a substrate speed of up to $100\ \text{mm/s}$. This system is designed to handle multiple inks simultaneously, enhancing its versatility for complex printing tasks.

Figure 3.9 shows the construction of the Jetlab-II. This system is equipped with a PH-46 printhead, capable of supporting up to four independent fluid reservoirs, each

channel features pneumatic control, allowing for precise management of the nozzle meniscus level through positive and negative pressure, thereby ensuring optimal jetting performance. The glass substrate prepared for printing is placed on a motorized stage that can move in the $x-$ and $y-$directions, facilitating precise control over the printing position. Additionally, the printhead assembly can move in the z-direction, controlled by a separate motor. A temperature control unit is integrated with the nozzle holder and substrate to control both the printhead and substrate temperatures, ensuring controlled and consistent printing conditions.

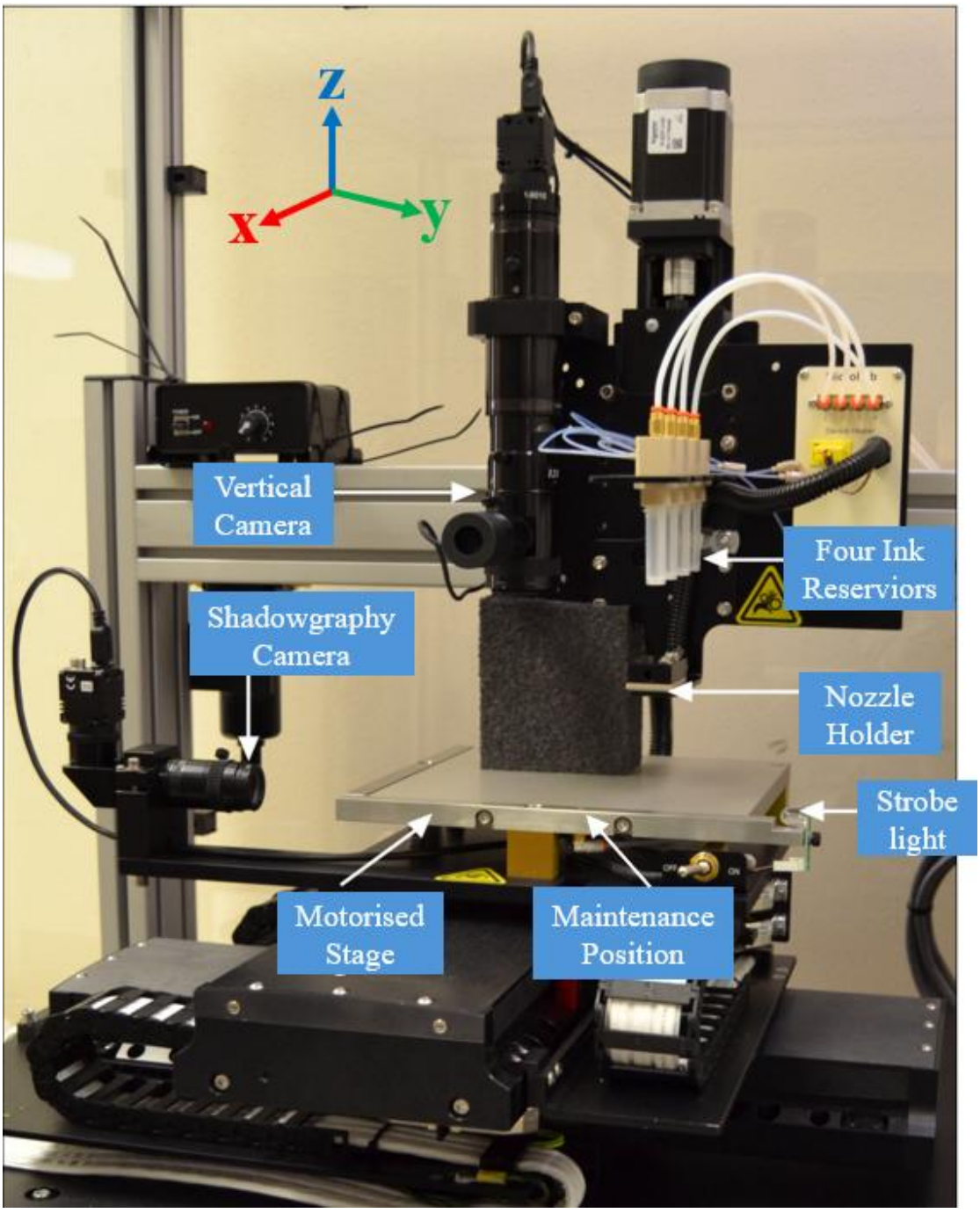


Figure 3.9 A photograph of the MicroFab Jetlab-II printer used to print LC arrays for the fabrication of optical devices in this thesis. The Jetlab-II system setup includes key components such as the camera for alignment, a shadowgraphy configuration for droplet observation, and motorized stage for precise movement of the substrate. The system is equipped with four ink reservoirs connected to the nozzle holder, which can accommodate multiple fluids. The maintenance position is a calibration area used to optimize printing parameters and ensure droplet stability before the printing process begins.

The MJ-AT-01-080-8MX nozzle used in the experiments, depicted in **Figure 3.10**, features an 80 μm orifice diameter and is driven by piezoelectricity. The nozzle's annular actuator is equipped with electrodes on both its inner and outer surfaces. The inner electrode is embedded within the nozzle structure, while the outer electrode is positioned on the external surface to enable efficient electrical connections. When a voltage difference is applied, an electric field is generated between the inner and outer electrodes, causing the piezoelectric actuator to expand radially and contract axially, thereby ejecting droplets.

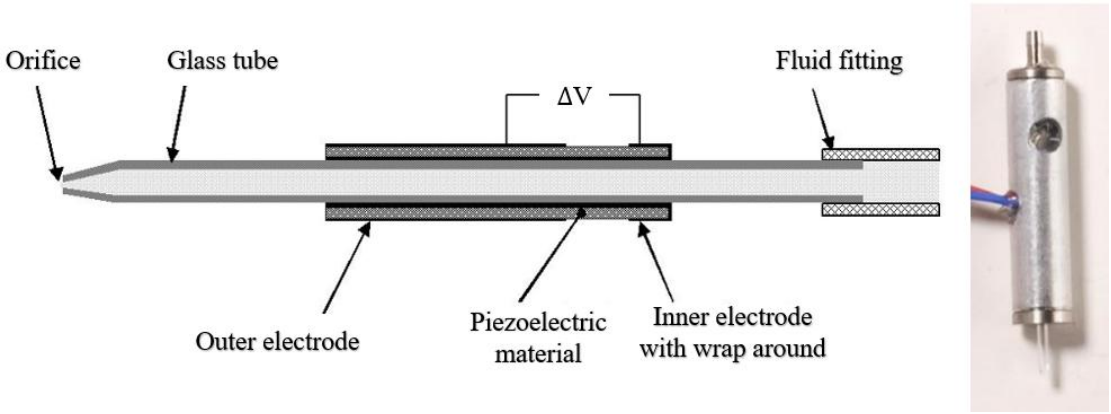


Figure 3.10 Schematic and Photograph of the MJ-AT-01-080-8MX Nozzle. The left diagram illustrates the internal structure of the MJ-AT-01-080-8MX nozzle, showing the orifice, glass tube, piezoelectric material, inner and outer electrodes, and fluid fitting. The photograph on the right shows the actual MJ-AT-01-080-8MX nozzle (orifice diameter of 80 μm) used in the Jetlab-II system.

The Jetlab-II system is controlled using the JetDrive-II software, illustrated in **Figure 3.11**. This software interface allows for the generation of waveforms, adjustment of jetting parameters according to the printhead specifications, and control over the motorized stage's movement in the *x*- and *y*-directions and the nozzle's movement in the *z*-direction. Before beginning the actual printing process, the printhead

can be positioned in the maintenance area (shown in Figure 3.9) to adjust parameters and adjust back pressure, ensuring the formation of stable and high-quality droplets. At the maintenance position, a shadowgraphy camera is aligned to capture the droplet ejection process. By adjusting the strobe delay bar, the timing of the strobe light can be synchronized with the droplet formation, enabling users to observe the droplet's shape and trajectory at specific moments in mid-air. This setup ensures precise monitoring and fine-tuning of droplet stability before printing.

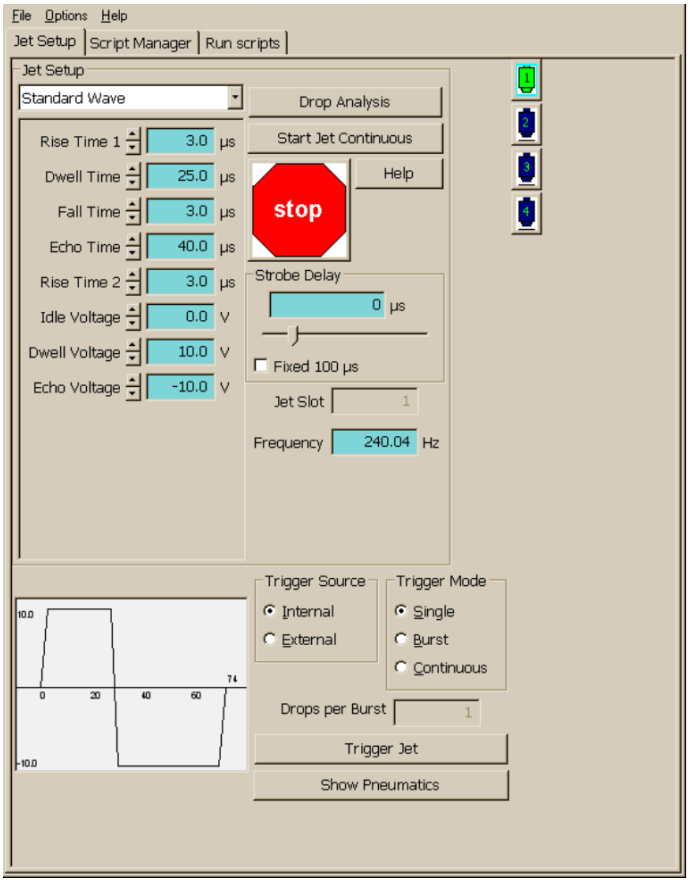


Figure 3.11 JetDrive-II Software Interface. The JetDrive-II software interface was used for controlling the Jetlab-II ink-jet printing system. This interface allows users to set up and adjust waveform parameters such as rise time, dwell time, and echo time, which control the jetting performance of the nozzles. It also provides options for adjusting strobe delay, frequency, and trigger modes. The software enables the precise control of droplet ejection and positioning on the substrate, facilitating high-precision printing of LC droplets.

Once droplet stability was confirmed, printing can commence using predefined or custom patterns available in JetDrive-II. The system achieves a droplet array positional accuracy of 5 μm. The four separate nozzles can operate simultaneously to dispense multiple inks onto the substrate in a desired pattern. Users can upload a black-and-white bitmap image to define the printing pattern. In this image, each pixel corresponds to a specific location on the substrate, determining the droplet placement. White pixels indicate positions where droplets will be deposited, while black pixels represent areas where no droplets will be printed. This method allows precise control over droplet spacing and pattern formation.

3.6.2 Bespoke Inkjet Printing System

The bespoke inkjet printing system developed in our group at Oxford was primarily designed for the detailed inspection of the dynamics of the impact process of printed LC droplets. This system incorporates a high-speed inspection camera, the Miro LAB310, which captures the dynamic changes in the droplet pattern as it impacts the substrate.

Figure 3.12 illustrates the configuration of this bespoke system. In this system, crossed polarizers are integrated to enhance the optical imaging of LC droplets. A high-intensity mercury vapor light source (89 North PhotoFluor II) directs light through a fiber optic guide and the first polarizer, illuminating the substrate. The light then passes

through the second polarizer and a 20× microscope objective, focusing the image onto the CMOS detector of the high-speed camera. This system was calibrated to capture high-speed POM videos of the droplets as they land and interact with the substrate, providing unprecedented dynamic details of the formation of director profiles within the LC droplets. The glass substrate, which holds the droplets, is mounted on a motorized $x - y$ stage, allowing precise and automated translation along both axes. This allows for precise positioning of the substrate relative to the inkjet nozzle. The system includes a static pressure pump that supplies ink to the printhead, which is equipped with an MJ-ABP-01-80 nozzle from MicroFab, featuring an 80-micron diameter nozzle. The printhead is driven by a JetDrive-II waveform generator, which controls the ejection of droplets. Additionally, the system is equipped with a detachable, temperature-controlled metal heating block, inserted into a slot adjacent to the nozzle for rapid heat transfer. Unlike closed-loop temperature control systems that rely on real-time feedback from temperature sensors, this heating block operates in an open-loop manner, as the thermal mass and close proximity to the nozzle allow rapid and stable temperature equilibration. This design facilitates quick thermal adjustments and simplifies the system while maintaining optimal printing conditions.

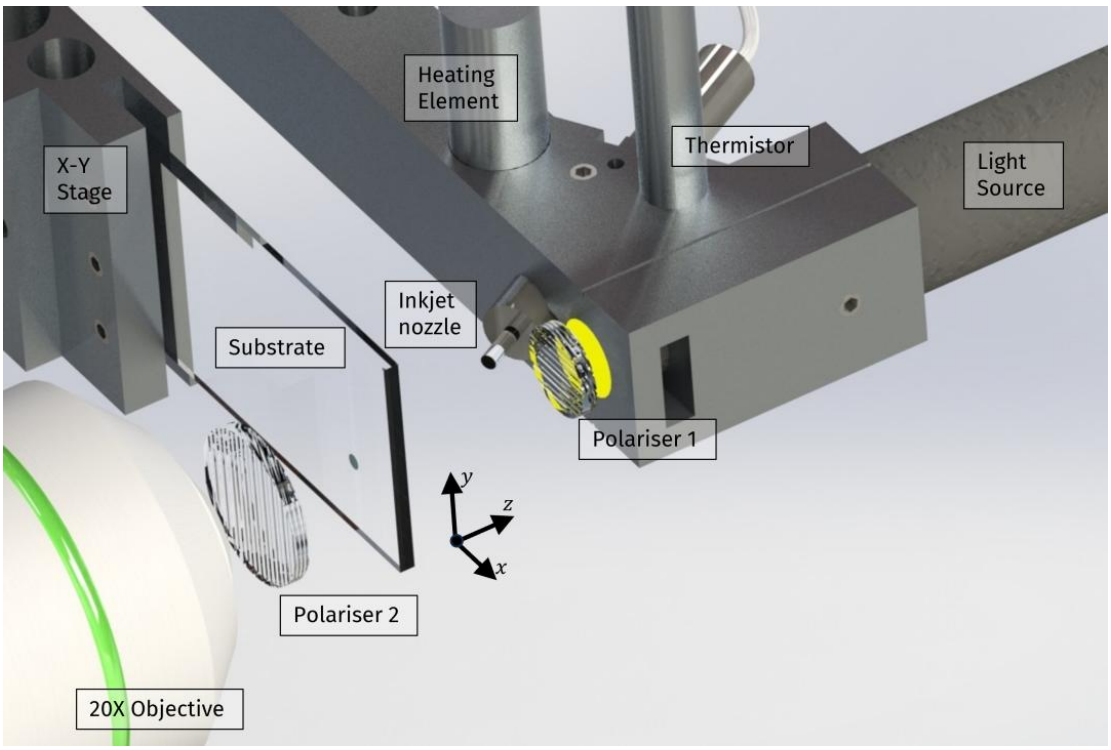


Figure 3.12 Experimental arrangement for printing and observation using the bespoke inkjet system. The high-speed CMOS camera is located after the 20× microscope lens[89].

Given the scope of this research, which involved printing various concentrations of LCs and chiral dopant mixtures, it was essential to maintain a rigorous cleaning protocol for the printhead and tubing. This protocol ensured that no residual ink or particulate matter contaminates subsequent prints. The cleaning process was performed in an environment that minimizes dust to prevent contamination. To begin with, the tubing was cleaned thoroughly. This process involved connecting the tubing to a syringe filled with IPA using a PTFE fitting. By carefully pressing the syringe, IPA was flushed through the tubing, effectively cleaning the inner walls. After flushing, a nitrogen gun was used to blow dry the interior of the tubing. The cleaned tubing was then stored in a clean, dry location to prevent any contamination.

Cleaning the nozzle, given its precision and fragility, required a meticulous approach. The nozzle was connected to a syringe filled with IPA, ensuring that the connection remains horizontal to the ground. This alignment reduced the risk of pushing any fine particles into the nozzle. By gently pushing the IPA through the nozzle, the expelled liquid stream can be observed. If the stream was straight and unbranched, the nozzle was clear. However, if the stream was crooked or bifurcated, this indicated a blockage.

In the case of a blockage, several methods were employed. Repeatedly flushing the nozzle with IPA and using the nitrogen gun to blow air through the nozzle can help dislodge any obstructing particles. If these methods were insufficient, the nozzle was submerged in IPA while a syringe was used to pull the IPA back through the nozzle, aiming to draw out the obstruction. After ensuring that the nozzle was clear, the nitrogen gun was again used to blow dry the internal passage. The nozzle was then stored in a dry, clean container to keep it free from contaminants until the next use. This comprehensive cleaning procedure ensured that the printhead and tubing remained free of any residual substances or particulates, thereby maintaining the integrity and accuracy of the printed droplets.

3.7 The EHD Printing

The EHD printing system in our lab was developed by former D.Phil. students (Waqas Kamal and Mengmeng Li), a schematic diagram (**Figure 3.13**) shows the assembly of

the EHD printing system. For this process, a substrate was placed on the centre of the translation stage, the system used two MT1-Z8 Thorlabs translation stages, allowing bi-directional (x- and y-axis) movement in 100 µm increments within a 12 mm × 12 mm range. The translation stages were controlled by independent motion controllers (KDC101, Thorlabs) connected to a computer, enabling precise movement. These controllers generated signals based on the stage motion and transmitted them to the function generator. This synchronization ensured that droplet deposition only occurred when the stage had reached the correct position, preventing issues such as droplets being printed while the stage was still moving or not yet properly aligned. A nozzle was then fixed at a distance of several millimetres directly above the substrate, which was filled with the CLC ink to be printed.

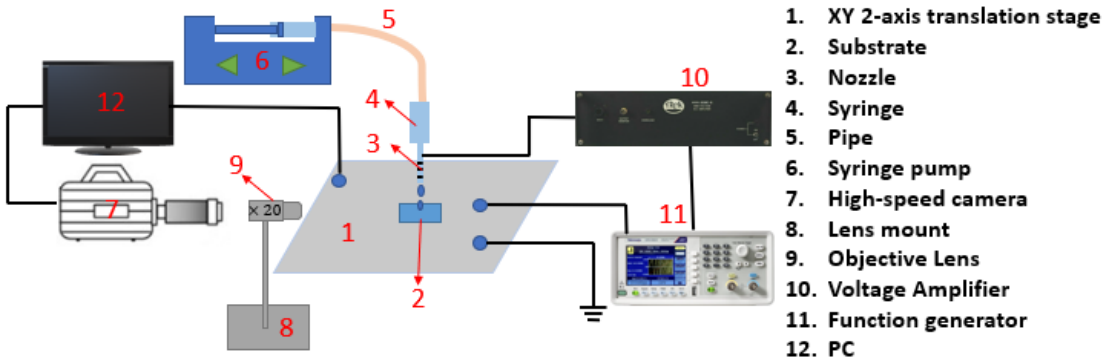


Figure 3.13 The experimental system for EHD printing of CLCs.

There are two types of nozzles used with this system: metal nozzles that are capable of printing droplets with diameters greater than 100 µm and glass nozzles that can be used for printing droplets with footprint diameters that are as small as 1 µm. The advantage of using the metal nozzles was that they are less susceptible to damage and

can be cleaned after use. The glass nozzles, on the other hand, whilst enabling the deposition of very small droplets, are very fragile and cannot be cleaned after use. Therefore, they can only be used once.

The nozzles are wrapped in copper wire and a function generator (AFG 2021 Tektronix) generates and transmits predefined waveform signals to the amplifier, creating an electric field between the nozzle and the substrate. The amplifier (Trek 609A) amplified the input signal 1000 times, achieving an output range of $0 - 10$ kV. The output signal was visualized and analysed using an oscilloscope (TBS 1000C, Tektronix) to confirm that the signal was amplified correctly and maintained the intended waveform characteristics necessary for precise operation. The translation stage was directly connected to ground, so that an electric potential difference was then formed between the nozzle and the substrate. The CLC inside the nozzle was a dielectric material that experiences a Lorentz force towards the substrate whenever the function generator produces a voltage pulse. A syringe pump (PHD-70-3009, Harvard apparatus) produces back pressure to the nozzle as the LC inks are typically of a high viscosity. A high-speed camera (Phantom V12.1) was placed on the side of the printing plate to observe the printing process and an objective lens was added to provide magnified images of the droplets as they were deposited.

3.8 Summary

In conclusion, this chapter outlined the essential experimental procedures employed to

study printed LC droplets. It detailed the preparation of LC samples, including preparing the mixture, cleaning the substrates, and fabricating in-plane etched substrates for applying electric fields. These steps ensure reliable and reproducible results. It also introduced analysis techniques, such as POM and pitch measurements, which were used to examine the structural and optical properties of the LC droplets. These methods provided insight into the director profile within droplets. The chapter also detailed the use of two inkjet printing systems: the commercially available Jetlab-II system and a bespoke inkjet printing system. Furthermore, the construction of an EHD printing system capable of printing ultra-small LC droplets has been described.

Chapter 4

Printed Chiral Nematic Liquid Crystal Droplets

"The universe is under no obligation to make sense to you."

Neil deGrasse Tyson

4 Printed Chiral Liquid Crystal Droplets

4.1 Introduction

With the rapid development of micro- and nanofabrication technologies, LC systems have progressively evolved from conventional planar films to a wide range of confined microstructures, including microparticles, microcavities, and microdroplets. This dimensional reduction has significantly broadened the functional landscape and application potential of LC materials. Among these systems, CLCs exhibit selective reflection of circularly polarized light and vivid structural coloration, underpinning applications in optical security, displays, and sensing technologies[90]. Encapsulating CLCs into droplet geometries preserves their anisotropic and responsive properties while offering enhanced dispersibility, interfacial tunability, and structural versatility[91]. Compared with planar LC films, droplet-based systems provide intrinsic advantages in size control, morphology engineering, and anchoring regulation, enabling reversible and stimulus-responsive optical behaviours[92]. As a result, CLC droplets have emerged as an important class of functional soft matter, attracting increasing interest across materials science, optics, chemistry, and bioengineering communities[93]. Despite this growing attention, existing reviews on LC microdroplets predominantly emphasize fabrication strategies or isolated optical functionalities[94], often lacking an integrated perspective linking fabrication, structural regulation, and emergent physical behaviour[95]. This gap highlights the importance of systematically studying LC

droplets themselves as fundamental photonic building blocks, motivating detailed investigations into their internal structures, interfacial effects, and structure–property relationships.

This chapter describes an investigation of printed CLC droplets, with a focus on examining the evolution of their internal director structure under varying alignment conditions and chiral dopant concentrations. The primary objective is to explore how the internal configuration of these droplets is affected by factors such as the type of alignment layer (homeotropic or planar) and the concentration of chiral dopant. Experimental observations using POM are complemented by numerical simulations based on Frank-Oseen elastic theory, implemented with COMSOL and finite difference methods. Some of the results from this chapter have been published in the paper *Soft Matter* **20**, 7493-7501 (2024).

4.2 Simulation of the LC Director Field

In this chapter, the primary focus is to investigate the physical properties and internal director profile of CLC droplets. Key factors such as the concentration of the chiral dopant, the type of alignment layer, and the droplet size are analysed to understand their impact on the internal configuration within the droplets. These parameters intricately influence the director field of the droplets, which are crucial for their resultant optical properties and potential applications.

To achieve a comprehensive understanding of these phenomena, simulations were employed to complement experimental observations. Numerical simulations based on the Frank-Oseen elastic theory equations were used to predict the internal configuration of LC droplets. These equations describe the elastic distortions in the director field due to splay, twist, and bend deformations, capturing the interplay between elastic energy and boundary constraints. To determine the equilibrium director configuration, the Frank-Oseen elastic free energy density was input into the Euler-Lagrange equations, yielding the lowest energy state that governs the LC director within the droplet. This process ensured that the simulated structures align with thermodynamic principles and minimizes discrepancies with experimental results.

4.2.1 Theoretical model

The comparison of simulation results with experimental data is critical for validating hypothesized internal director structures and explaining features observed in the POM images. Simulations provide a detailed visualization of how the LC director responds to varying chiral dopant concentrations, alignment conditions, and droplet sizes. The initial simulations focus on the simplest case of nematic LC droplets without chiral dopant. In this scenario, the droplets were printed on a homeotropic alignment layer, which ensured that the director at the droplet's base was perpendicular to the substrate. This condition eliminates axial influences and prevents variations in the director along the azimuthal direction, thereby simplifying the analysis. This controlled environment

isolates the effects of geometrical confinement and boundary conditions, offering insights into the fundamental molecular ordering within LC droplets.

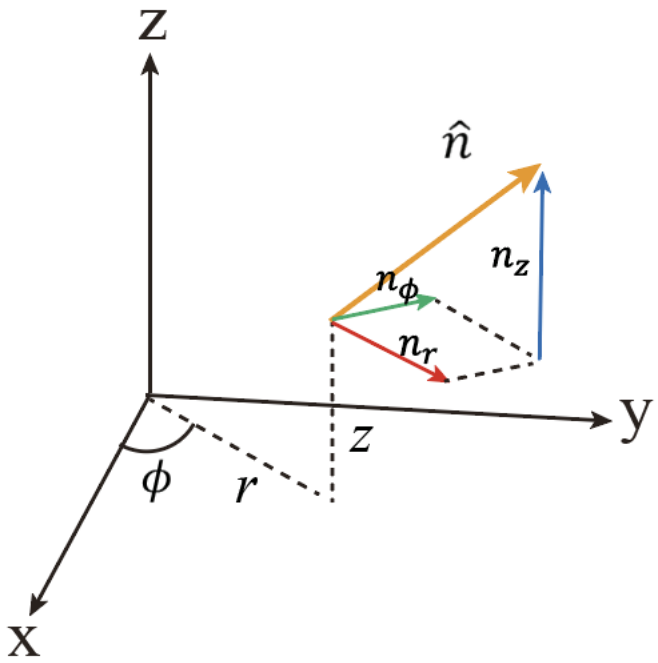


Figure 4.1 Cylindrical coordinate system used for describing the director field within a printed LC droplet. The position vector is represented by its components r (radial distance), ϕ (azimuthal angle), and z (axial position). The director vector $\hat{n}$ indicates the local molecular orientation. The director $\hat{n}$ is decomposed into three components: n_r, n_ϕ, and n_z.

To simulate the director field within a nematic LC droplet produced by inkjet printing, a mathematical model based on the Frank elastic theory (as mentioned in Section 2.3.2) was established. The orientation of the LC molecules, represented by the director field $\hat{n}$, plays a significant role in determining the droplet's optical and electrical properties. Given the inherent symmetry of the droplet, we employ the cylindrical coordinate system (r, ϕ, z) to describe the spatial positions (**Figure 4.1**). Here, r denotes the radial distance, ϕ is the azimuthal angle around the central axis, and z represents the height above the substrate. Using cylindrical coordinates aligns

with the symmetry of the droplet and simplifies the mathematical treatment by reducing the dependence of the director field on the azimuthal angle ϕ.

The director field, which represents the local average orientation of the LC molecules, is expressed as a unit vector

$$\hat{n}(r,z) = \begin{bmatrix} n_r(r,z) \\ n_\phi(r,z) \\ n_z(r,z) \end{bmatrix}. \tag{4.1}$$

The components n_r, n_ϕ, and n_z correspond to the radial, azimuthal, and axial components of the director, respectively. Due to the droplet's radial symmetry and uniform boundary conditions produced by homeotropic alignment layer in the azimuthal direction, the director components do not depend on ϕ, leading to:

$$\frac{\partial n_r}{\partial \phi} = \frac{\partial n_\phi}{\partial \phi} = \frac{\partial n_z}{\partial \phi} = 0. \tag{4.2}$$

Thus, the director field varies only with respect to r and z, further reducing the complexity of the system. The total elastic free energy of the LC droplet is determined by the spatial variation of the director field. According to the Frank elastic theory, the free energy density accounts for three fundamental deformation modes: splay, twist, and bend, as discussed in Section 2.3.2 The elastic free energy density is given by:

$$f(\vec{n}) = \frac{1}{2}K_1[\nabla \cdot \hat{n}]^2 + \frac{1}{2}K_2[\hat{n} \cdot (\nabla \times \hat{n})]^2 + \frac{1}{2}K_3[\hat{n} \times (\nabla \times \hat{n})]^2, \tag{4.3}$$

where K_1, K_2, K_3 are the splay, twist, and bend elastic constants, respectively. These constants quantify the energetic penalties associated with each type of deformation.

To compute $f_{elastic}$, we need explicit expressions for the divergence $(\nabla \cdot \hat{n})$ and curl $(\nabla \times \hat{n})$ of the director field in cylindrical coordinates. The divergence of a vector field in cylindrical coordinates is expressed as:

$$\nabla \cdot \hat{n} = \frac{1}{r}\left[n_r + r\frac{\partial n_r}{\partial r}\right] + \frac{\partial n_z}{\partial z} = \frac{n_r}{r} + \frac{\partial n_r}{\partial r} + \frac{\partial n_z}{\partial z}. \tag{4.4}$$

The curl of a vector field in cylindrical coordinates is given by:

$$\nabla \times \hat{n} = \begin{pmatrix} -\frac{\partial n_\phi}{\partial z} \\ \frac{\partial n_r}{\partial z} - \frac{\partial n_z}{\partial r} \\ \frac{1}{r}\left[n_\phi + r\frac{\partial n_\phi}{\partial r}\right] \end{pmatrix} = \begin{pmatrix} -\frac{\partial n_\phi}{\partial z} \\ \frac{\partial n_r}{\partial z} - \frac{\partial n_z}{\partial r} \\ \frac{n_\phi}{r} + \frac{\partial n_\phi}{\partial r} \end{pmatrix}. \tag{4.5}$$

The splay term involves $(\nabla \cdot \hat{n})^2$, the twist term is given by

$$\hat{n} \cdot (\nabla \times \hat{n}) = -n_r\frac{\partial n_\phi}{\partial z} + n_\phi\left(\frac{\partial n_r}{\partial z} - \frac{\partial n_z}{\partial r}\right) + n_z\left(\frac{n_\phi}{r} + \frac{\partial n_\phi}{\partial r}\right), \tag{4.6}$$

and the bend term is given by

$$\hat{n} \times (\nabla \times \hat{n}) = \begin{pmatrix} n_\phi\left(\frac{n_\phi}{r} + \frac{\partial n_\phi}{\partial r}\right) - n_z\left(\frac{\partial n_r}{\partial z} - \frac{\partial n_z}{\partial r}\right) \\ n_z\frac{\partial n_\phi}{\partial z} - n_r\left(\frac{n_\phi}{r} + \frac{\partial n_\phi}{\partial r}\right) \\ n_r\left(\frac{\partial n_r}{\partial z} - \frac{\partial n_z}{\partial r}\right) + n_\phi\frac{\partial n_\phi}{\partial z} \end{pmatrix}. \tag{4.7}$$

Each term in the elastic free energy density can now be calculated. Now substitute Eqs. (4.4), (4.6), (4.7) into Eq. (4.3) to calculate the resultant elastic free energy density:

$$f = \frac{1}{2}K_1\left(\frac{n_r}{r} + \frac{\partial n_r}{\partial r} + \frac{\partial n_z}{\partial z}\right)^2 + \frac{1}{2}K_2\left[-n_r\frac{\partial n_\phi}{\partial z} + n_\phi\left(\frac{\partial n_r}{\partial z} - \frac{\partial n_z}{\partial r}\right) + n_z\left(\frac{n_\phi}{r} + \frac{\partial n_\phi}{\partial r}\right)\right]^2 + \frac{1}{2}K_3\left\{\left[n_\phi\left(\frac{n_\phi}{r} + \frac{\partial n_\phi}{\partial r}\right) - n_z\left(\frac{\partial n_r}{\partial z} - \frac{\partial n_z}{\partial r}\right)\right]^2 + \left[n_z\frac{\partial n_\phi}{\partial z} - n_r\left(\frac{n_\phi}{r} + \frac{\partial n_\phi}{\partial r}\right)\right]^2 + \left[n_r\left(\frac{\partial n_r}{\partial z} - \frac{\partial n_z}{\partial r}\right) + n_\phi\frac{\partial n_\phi}{\partial z}\right]^2\right\}. \tag{4.8}$$

Due to the complexity of these expressions, further simplification and exact computation for specific configurations require numerical methods. In this work, we employ the symbolic toolbox in MATLAB to symbolically derive and simplify the terms.

To determine the equilibrium configuration of the director field that minimizes the total free energy in a nematic LC droplet, the variational principle is applied to f for each component of the director field $n = (n_r,\ \ n_\phi,\ \ n_z)$. This leads to the Euler-Lagrange equations:

$$n_r: \quad \frac{\partial f}{\partial n_r} - \frac{\partial}{\partial r}\left(\frac{\partial f}{\partial\left(\frac{\partial n_r}{\partial r}\right)}\right) - \frac{\partial}{\partial z}\left(\frac{\partial f}{\partial\left(\frac{\partial n_r}{\partial z}\right)}\right) = 0, \tag{4.9}$$

$$n_\phi: \quad \frac{\partial f}{\partial n_\phi} - \frac{\partial}{\partial r}\left(\frac{\partial f}{\partial\left(\frac{\partial n_\phi}{\partial r}\right)}\right) - \frac{\partial}{\partial z}\left(\frac{\partial f}{\partial\left(\frac{\partial n_\phi}{\partial z}\right)}\right) = 0, \tag{4.10}$$

$$n_z: \quad \frac{\partial f}{\partial n_z} - \frac{\partial}{\partial r}\left(\frac{\partial f}{\partial\left(\frac{\partial n_z}{\partial r}\right)}\right) - \frac{\partial}{\partial z}\left(\frac{\partial f}{\partial\left(\frac{\partial n_z}{\partial z}\right)}\right) = 0. \tag{4.11}$$

These equations are highly nonlinear and challenging to solve analytically. To address

this, a numerical approach based on the relaxation method was employed, which is an effective numerical strategy, converting the complex steady-state problem into a manageable dynamic evolution process. The relaxation method introduces a virtual time parameter t, transforming the static equilibrium problem into a dynamic iteration process, allowing the director field to gradually change to the minimum energy configuration. In this framework, the director field components n_r, n_ϕ, n_z are treated as functions of the virtual time t.

To simulate the iterations of the system towards equilibrium, dynamic equations are introduced:

$$\frac{\partial n_i}{\partial t} = -\left(\frac{\partial f}{\partial n_i} - \frac{\partial}{\partial r}\left(\frac{\partial f}{\partial\left(\frac{\partial n_i}{\partial r}\right)} \right) - \frac{\partial}{\partial z}\left(\frac{\partial f}{\partial\left(\frac{\partial n_i}{\partial z}\right)} \right) \right), \tag{4.12}$$

where $i = r, \phi, z$. It dictates that the rate of change of the director field components is proportional to the negative gradient of the free energy density. This ensures that the system iterates towards a state of minimum free energy. Given the complexity of these equations, the specific forms of these equations were derived and simplified in MATLAB using the symbolic toolbox. Director field generation

To build the orientational distribution of molecules within nematic LC droplets deposited on a homeotropic alignment layer based on the above equations, a custom C program was developed to numerically simulate the director field configuration. The simulation begins by defining the material properties and essential parameters of the LC, including its elastic constants, radial and axial grid resolution, iteration step size,

and total number of iterations. These parameters ensure numerical accuracy and computational stability. The spatial domain of the droplet is represented on a 2D grid in cylindrical coordinates, due to the radial symmetry of the droplet. At every point within the droplet, the director is set so that it follows the outward normal of this curved surface. Additionally, on the substrate and along the central axis, the director is explicitly fixed to point vertically, ensuring that the homeotropic boundary conditions are satisfied. This means that at the surface of the droplet, the LC director is oriented perpendicular to the surface, pointing toward the outside of the droplet. The computational domain was divided into a grid, with nodes representing positions in the droplet. For each node, the first- and second-order spatial derivatives, as well as mixed derivatives, were computed. The temporal derivatives $\frac{\partial n_i}{\partial t}$ were calculated using the relaxation Eq. (4.12). The director field components were updated iteratively using an explicit time-stepping scheme:

$$n_i^{(k+1)}(r,z) = n_i^{(k)}(r,z) - \gamma \frac{\partial n_i}{\partial t}, \tag{4.13}$$

where $n_i^{(k)}(r,z)$ denotes the i^{th} component of the director field at the k^{th} iteration. γ is the relaxation parameter that controls the step size. Proper selection of γ is crucial to ensure numerical stability and convergence. After each iteration, the director field vectors were normalized to maintain their unit length. This ensures that the physical constraint

$$n_r^2 + n_\phi^2 + n_z^2 = 1 \tag{4.14}$$

is preserved. Neglecting this constraint during the minimization process could lead to unphysical solutions where the director length changes arbitrarily to reduce the free energy.

Boundary conditions were reimposed at each iteration to enforce homeotropic anchoring at the droplet surface and alignment surface. Through repeated iterations, the director field adjusted dynamically, reducing the total free energy and eventually converging to a stable equilibrium configuration. As a result, this C program generates three key output files for visualizing and analysing the director field distribution within the nematic LC droplet. Specifically, the files capturing the director tilt, twist, and retardance (the optical phase delay induced by the director field) are utilized to construct detailed representations of the droplet's internal director orientation and optical properties.

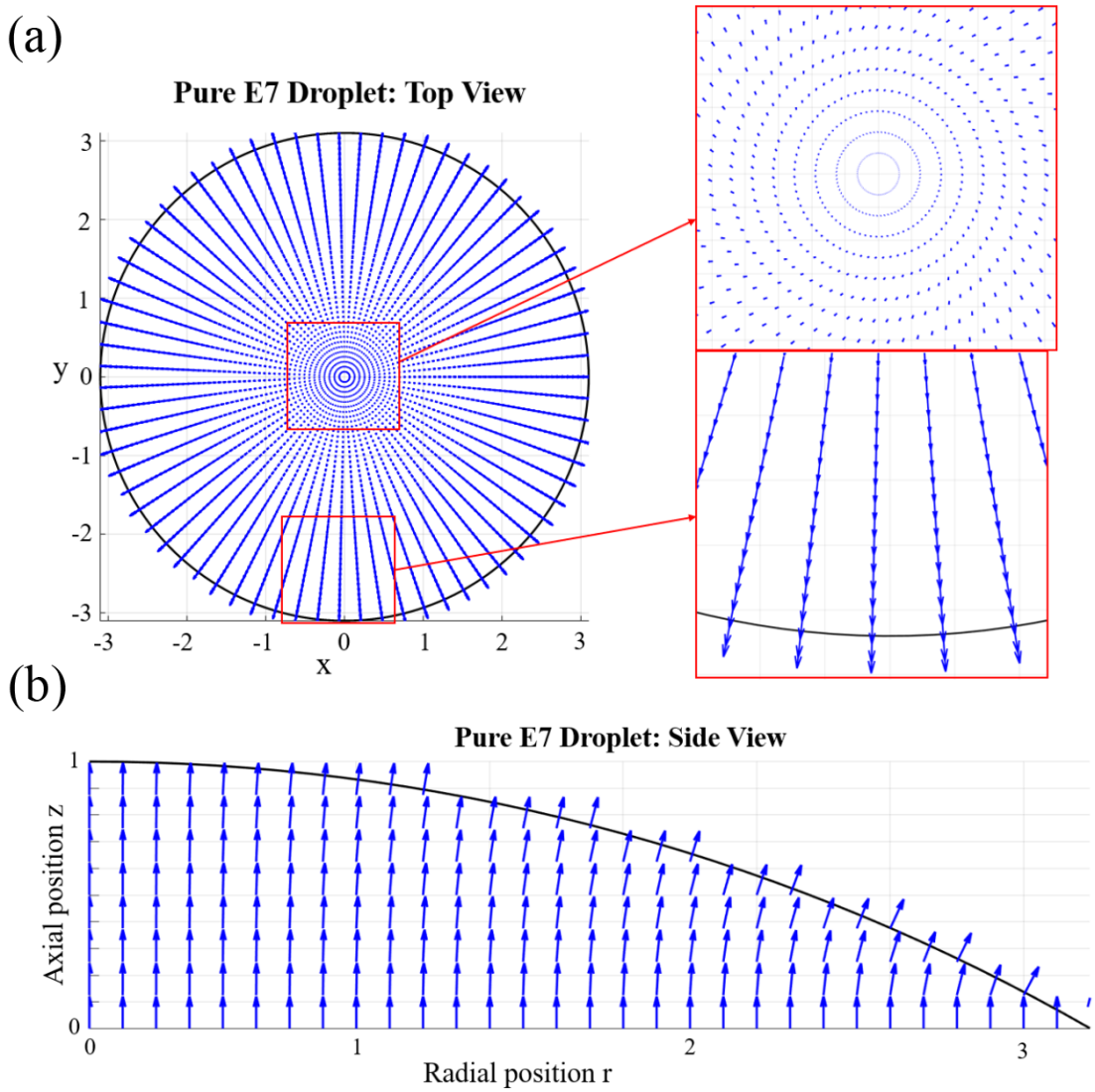


Figure 4.2 Simulated director field of a printed nematic LC (E7) droplet. (a) Top view: director at the centre is vertically aligned, transitioning smoothly to a radial orientation near the surface due to perpendicular anchoring. Insets show detailed transitions at the centre and edge. (b) Side view: director tilts progressively from vertical at the centre to radial near the droplet surface.

The tilt file provides the tilt angle of the director field at each grid point in the droplet, representing the angular deviation of the director from the vertical z-axis. This tilt angle, $\theta(r,z)$, is calculated using $\sin^{-1} n_z(r,z)$, where $\theta(r,z)$ the angle between the director and the z-axis, $n_z(r,z)$ is the axial component of the director. The tilt angle reveals how the director orients relative to the droplet's central axis and

indicates the extent of splay and bend deformations. This file is particularly useful for visualizing the director alignment throughout the droplet and is employed to generate cross-sectional views of the director field. The twist.dat file captures the twist angle of the director field, defined as the rotation of the director around the vertical z-axis. The twist angle, $\psi(r,z)$, is computed as $\tan^{-1}\frac{n_\phi(r,z)}{n_r(r,z)}$, where $\psi(r,z)$ represents the in-plane rotation of the director field, $n_r(r,z)$ and $n_\phi(r,z)$ are the radial and azimuthal components of the director, respectively. This file identifies regions where twist deformations occur, which are typically minimal in the absence of chirality or external fields.

Figure 4.2 presents the director field configuration of a nematic LC droplet (E7) from both the top view (Figure 4.2(a)) and side view (Figure 4.2(b)). In the top view, the director at the centre of the droplet is predominantly aligned perpendicular to the substrate, reflecting the homeotropic boundary condition. This indicates that the LC director at the core exhibits a vertical orientation relative to the substrate. However, because the droplet forms a curved (spherical cap) shape, the surface normal tilts away from the vertical as one moves toward the edge. To satisfy the homeotropic anchoring at the droplet surface, the initial director field is set to follow this local surface normal. In simple terms, as the radial distance increases, the director gradually tilts outward in accordance with the curvature of the droplet, ensuring that it remains perpendicular to the surface. The inset magnifies the central region, showing the near-perfect vertical alignment of the director at the core. Despite slight deviations caused by minor

numerical inaccuracies inherent to the simulation process, the twist component is negligible, consistent with the assumption of no significant azimuthal variation in the director field.

In the side view, the director points straight up along the vertical axis at the centre of the droplet. Moving outward, the director undergoes a progressive tilt, aligning increasingly with the radial direction near the surface of the droplet due to the homeotropic boundary condition. This configuration ensures that the director field satisfies the hypothesis of smooth alignment from the vertical orientation at the droplet's centre to a tangential orientation near the surface. Overall, the simulation confirms that the twist component of the director field is negligible as expected, because the droplet lacks chirality and is constrained by symmetric boundary conditions. Slight variations in twist observed at the boundaries are minimal and do not significantly affect the overall director configuration.

4.2.2 Simulating POM images

Simulating the appearance of LC droplets under crossed polarizers provides a powerful means of validating numerical models. By comparing the simulated POM images of droplets with experimental observations, we can assess the accuracy of our simulations. The first step involved utilizing the retardance file generated by the C program which quantified the phase difference introduced between the ordinary and extraordinary rays as polarized light traverses the anisotropic medium. This retardance is a function of the

director field components n_r, n_ϕ, and n_z, as well as the refractive indices n_e, and n_o corresponding to the extraordinary and ordinary axes of the LC, respectively. The retardance δ at any point can be expressed as:

$$\delta(r,\phi,z) = \frac{2\pi d\left(\sqrt{\frac{n_e{}^2 n_o{}^2}{n_e{}^2\cos^2\theta + n_o{}^2\sin^2\theta}} - n_o\right)}{\lambda}, \tag{4.15}$$

where d is the thickness of the droplet along the light path, λ is the wavelength of the incident light, and $\theta(r,z)$ the angle between the director and the z-axis. The intensity I of the transmitted light through the analyser can be expressed by:

$$I(r,\phi,z) = I_0 sin^2(2\chi)\, sin^2\left(\frac{\delta(r,\phi,z)}{2}\right)$$

$$\text{with } \chi(r,\phi,z) = (\phi + \psi(r,z)) - \theta_p, \tag{4.16}$$

where I_0 is the initial light intensity, and θ_p is the fixed orientation of the polarizer. The angle $\psi(r,z)$ is the local twist angle of the director field, while ϕ is the azimuthal coordinate of the droplet. The term $\chi(r,\phi,z)$ thus quantifies the effective angular deviation between the in-plane orientation of the director and the polarizer. The transmitted light depends on the product of the two sine-squared terms, maximum transmission is achieved only when the director is optimally misaligned with the polarizer (i.e., when $\sin^2(2\chi)$ is large) and when there is large retardance.

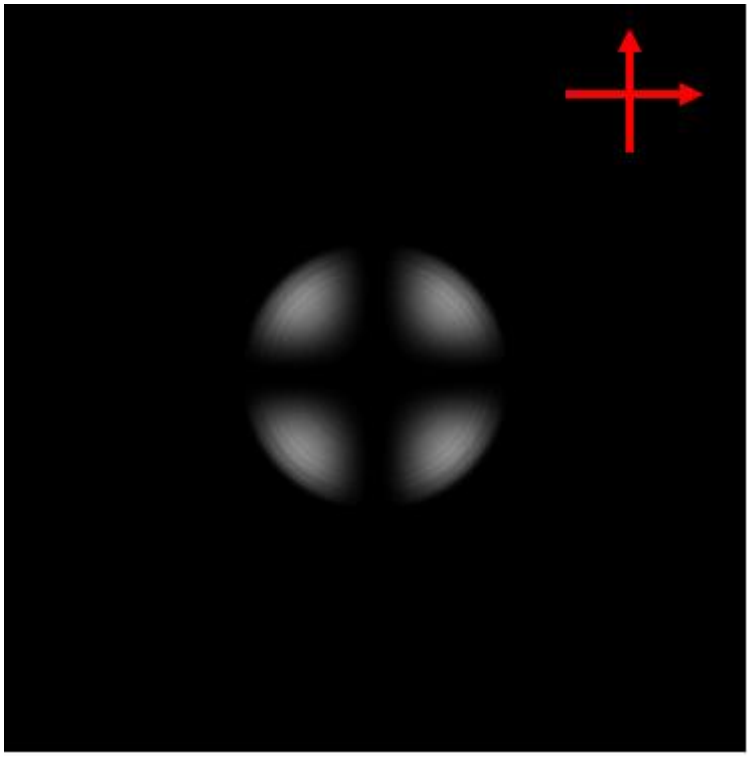


Figure 4.3 Simulated POM image of a nematic LC droplet on a homeotropic alignment layer under crossed polarizers. The single-headed red arrows indicate the orientation of the polarizer and analyser.

Figure 4.3 illustrates the simulated appearance of a nematic LC droplet deposited on a homeotropic alignment layer under crossed polarizers. The observed pattern features two perpendicular black crosses aligned with the polarizer and analyser axes, which is directly related to the simulated internal director field (Figure 4.2). At the centre of the droplet, the LC director remains vertical, aligned with the z-axis due to the homeotropic anchoring at the substrate. In this region, the transmitted light experiences minimal birefringence because the optical axis of the LC aligns with the propagation direction of the incident light. As a result, the SoP of the transmitted light remains unchanged and is fully blocked by the analyser, producing the central dark area.

Moving radially outward, the LC director gradually tilts from the vertical to a more radial orientation. This tilt leads to birefringence, where the polarization of the incident light is modified as it passes through the droplet. However, in two specific directions aligned with the polarizer axes, the LC director tilt to the direction that align to the polarizer direction. In these regions, the tilt of the LC director does not induce any resultant polarization change in the transmitted light, causing two dark lines to appear along these axes. In the regions between these dark lines, where the LC director is neither parallel nor perpendicular to the polarizer axes, the transmitted light undergoes partial polarization rotation. This results in varying brightness in these areas. The brightness is highest where the LC director is at an angle of approximately $45°$ to the polarizer directions, as this maximizes the effective birefringence. Additionally, at the edge of the droplet, the LC director is most radially tilted, further enhancing the birefringence and contributing to the higher transmitted intensity observed near the boundary.

4.2.3 Simulation of chiral nematic LC droplets

In this work, the focus extended beyond the study of nematic LC droplets to include an investigation of how the introduction of chiral dopant influences the internal structure of the LC droplet. To simulate the director field of a CLC droplet deposited on a homeotropic alignment layer, we build upon the previously established framework for nematic LC droplets. Under the conditions of radial symmetry and a uniform homeotropic alignment layer, the director field components (n_r, n_ϕ, and n_z) are still

independent of the azimuthal angle ϕ. This simplification remains valid for chiral nematic droplets, as the chirality introduces a preferred twist without breaking the radial symmetry.

Chiral dopants impose a helical twist on the director field, requiring the inclusion of a chirality-dependent term in the Frank-Oseen elastic free energy density, expressed as:

$$f(\vec{n}) = \frac{1}{2}K_1[\nabla \cdot \hat{n}]^2 + \frac{1}{2}K_2[\hat{n} \cdot (\nabla \times \hat{n}) - q_0]^2 + \frac{1}{2}K_3[\hat{n} \times (\nabla \times \hat{n})]^2, \quad (4.17)$$

where $q_0 = \frac{2\pi}{P}$, and P denotes the pitch of the CLC. Key modifications introduced by chirality are reflected in the twist term $[\hat{n} \cdot (\nabla \times \hat{n}) - q_0]$. This term captures the inherent helical structure imparted by the chiral dopant, inducing non-zero twist angles even in the absence of external perturbations. While the divergence $[\nabla \cdot \hat{n}]$ and bend $[\hat{n} \times (\nabla \times \hat{n})]$ terms remain unchanged. The modified free energy density equation is then used to derive the Euler-Lagrange equations that govern the equilibrium configuration of the director field[96, 97]. The derivation is performed in MATLAB, leveraging its symbolic computation toolbox to handle the complexity introduced by the chirality term q_0.

The iterative relaxation method used previously for nematic droplets was adapted to minimize this modified free energy. Initial conditions for the director field were defined based on the boundary conditions: the homeotropic alignment layer enforces perpendicular alignment at the substrate, while the LC-air interface enforces

perpendicular alignment at the interface. Key outputs of the simulation include files which record the tilt angles, twist angles, and retardance values within the droplet, as before.

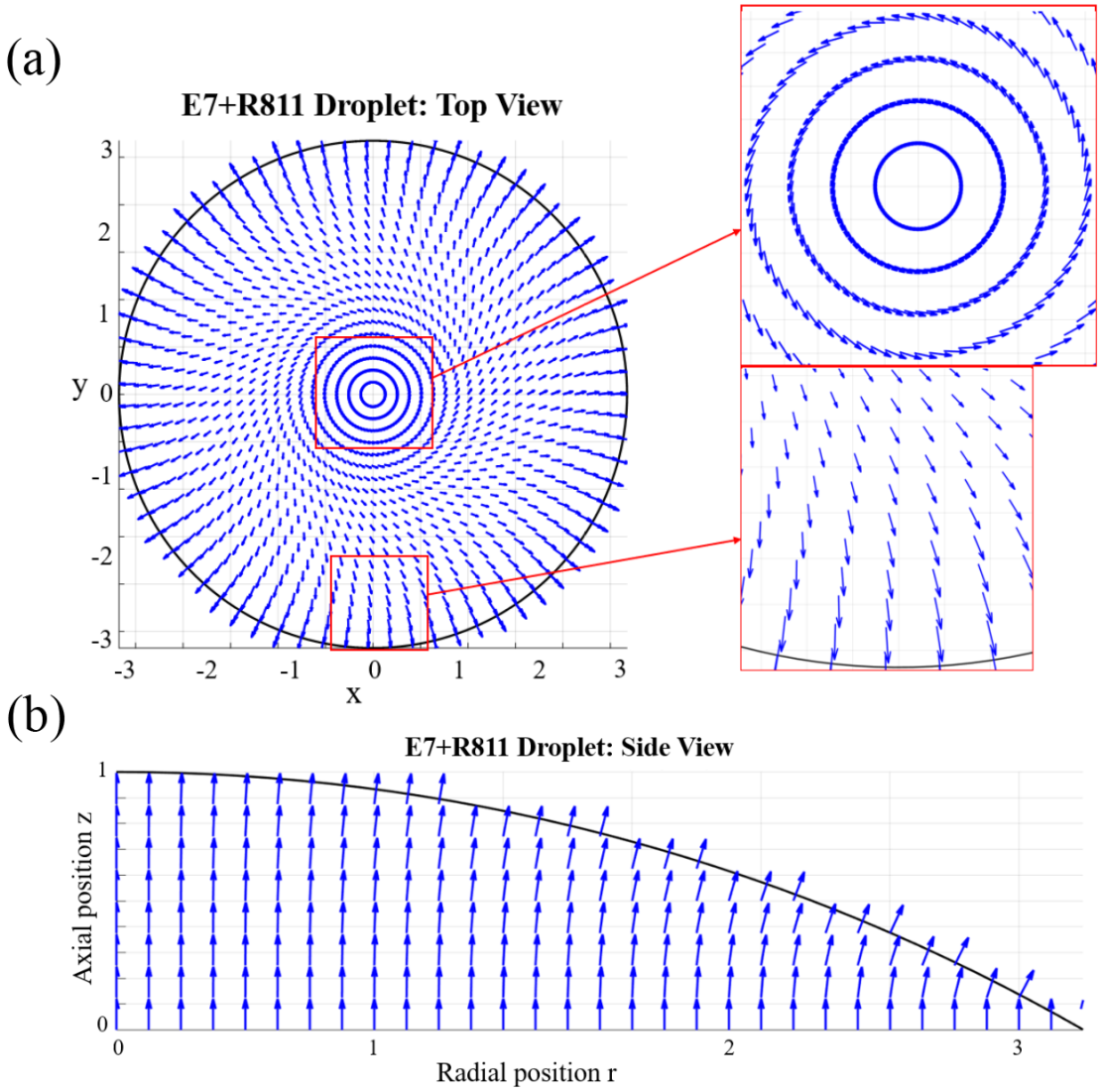


Figure 4.4 Simulated director field of an E7 droplet doped with a right-handed chiral dopant ($q_0 = -1.6\mu m^{-1}$). (a) Top view: the director field exhibits a helicoidal structure, where the twist induced by the chiral dopant creates a clockwise pattern consistent with right-handed chirality. (b) Side view: the director tilt shows a gradient from vertical orientation at the droplet centre to a radial orientation near the surface.

Based on the simulation data, the visualized director field within the CLC droplet,

presented as a top view and a side view (**Figure 4.4**), provides insights into the internal molecular orientation. The top view illustrates a concentric alignment pattern. Near the droplet centre, the director remains predominantly vertical, indicated by vectors aligned along the axial direction. This behaviour is consistent with the perpendicular anchoring condition at the LC-air interface. Moving radially outward, the director tilts progressively away from the vertical axis and aligns increasingly in the radial direction. This transition results from the balance between elastic forces and the chiral term q_0, which induces a helical twist in the director field. The azimuthal component of the twist becomes apparent, forming a clockwise spiral structure indicative of the chiral dopant's influence, which imposes a right handedness to the molecular arrangement. The side view confirms the transition observed in the top view. Near the droplet base, the director aligns vertically due to the homeotropic anchoring condition. Closer to the droplet surface, the director tilts outward, aligning perpendicularly to the curved surface. This distribution reflects the radial symmetry imposed by the homeotropic alignment layer and uniform boundary conditions.

Simulating the optical response of CLC droplets under crossed polarizers using the same method (Eq. (4.16)), we obtain **Figure 4.5**. The distinct patterns observed in the images are a result of the interaction between the director field of the CLC droplets and polarized light under crossed polarizers. The spiral structures in both Figure 4.5(a) and (b) arise from the intrinsic helicoidal arrangement of the LC director induced by the left-handed ($q_0 = +1.6$) and right-handed ($q_0 = -1.6$) chiral dopants, respectively.

The handedness of the dopant determines the direction of the twist in the director field, which directly affects the transmitted light intensity patterns.

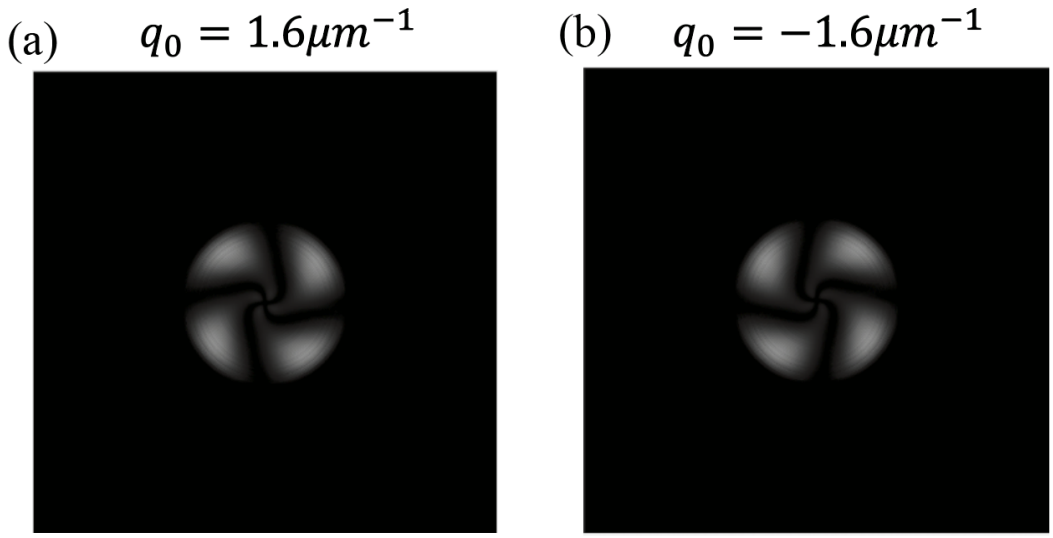


Figure 4.5 Simulated POM images of CLC droplets under crossed polarizers. (a) Left-handed chiral dopant ($q_0 = 1.6\ \mu m^{-1}$), showing a counterclockwise spiral. (b) Right-handed chiral dopant ($q_0 = -1.6\ \mu m^{-1}$), displaying a clockwise spiral.

For Figure 4.5(a) with left-handed chirality, the director field twists in a counterclockwise direction as it moves radially outward. This results in a spiral pattern of optical retardance. Under crossed polarizers, regions where the director aligns parallel to one of the polarizers remain dark, while regions with intermediate tilt and twist cause birefringence, creating the bright bands in the spiral pattern. The counterclockwise orientation of the bands reflects the left-handed chirality of the dopant. For Figure 4.5(b) with right-handed chirality, the director field twists in the opposite, clockwise direction.

Simulating CLC droplets with higher concentrations of chiral dopants need a more advanced modelling approach due to the increased complexity of the director field. At

higher concentrations, the pitch of the helical structure becomes shorter, leading to stronger gradients in the director configuration and potentially more pronounced defects. These effects introduce additional challenges, such as higher-order elastic deformations and potential coupling between elastic and surface anchoring effects. To address these complexities, I collaborated with another D.Phil student, Alva C. J. Orr, who specialized in Lattice Boltzmann simulations of LC droplets. This provided the expertise and resources necessary to extend our initial work to higher-order simulations, ensuring the accuracy and reliability of results for droplets with highly chiral compositions.

4.2.4 COMSOL simulations

To model the director configuration of CLC droplets printed onto a planar alignment layer which do not have radial symmetry, COMSOL Multiphysics was employed due to its capability to solve complex partial differential equations (PDEs) through the finite element method (FEM). Unlike the homeotropic alignment case, where the director field could be simplified by assuming no dependence on the azimuthal angle ϕ, the planar alignment scenario requires a full three-dimensional treatment of the director field. Consequently, the previously developed custom simulation code was no longer suitable, necessitating the use of COMSOL's flexible PDE-solving framework.

Due to the increased complexity of the CLC case, I first focussed on simulating nematic LC droplets without the inclusion of a chiral dopant. This allowed us to

simplify the elastic free energy formulation while still capturing the fundamental director configurations under planar anchoring conditions. In the absence of chirality, we adopted the one-constant approximation, assuming that the three Frank elastic constants are equal, i.e., $K_1 = K_2 = K_3$. Under this assumption, the free energy density simplifies to:

$$f(\vec{n}) = \frac{1}{2}K[(\nabla \cdot \hat{n})^2 + (\nabla \times \hat{n})^2], \tag{4.18}$$

To find the equilibrium director configuration, we minimize the total free energy with respect to the three Cartesian components of the director, n_x, n_y, and n_z. This minimization was carried out by applying the Euler-Lagrange equation as before. For instance, by varying the free energy with respect to n_x, we derive a PDE of the form:

$$0 = K\left(-\frac{\partial^2 n_x}{\partial x^2} - \frac{\partial^2 n_x}{\partial y^2} - \frac{\partial^2 n_x}{\partial z^2}\right), \tag{4.19}$$

A viscous term (with rotational viscosity γ) was introduced and we write a time-dependent PDE:

$$-\gamma \frac{\partial n_x}{\partial t} = -K\nabla^2 n_x, \tag{4.20}$$

where $\nabla^2 = \frac{\partial^2}{\partial x^2} + \frac{\partial^2}{\partial y^2} + \frac{\partial^2}{\partial z^2}$ is the Laplacian operator. Similar equations were obtained for n_y and n_z, forming a system of three coupled PDEs that describe the time evolution of the director field. Because the director must remain a unit vector ($|n| = 1$), we include a penalty term in the free energy of the form

$$f_\mu = \frac{\mu}{4}\left(n_x^2 + n_y^2 + n_z^2 - 1\right)^2, \tag{4.21}$$

with a large constant μ to enforce the constraint. When this term was added, the system of PDEs becomes:

$$-\gamma \frac{\partial n_i}{\partial t} = -K\nabla^2 n_i + \mu\left(n_x^2 + n_y^2 + n_z^2 - 1\right)^2 n_i, \qquad i = x, y, z. \tag{4.22}$$

For implementation in COMSOL, these equations were rewritten in a standard form required by the finite element solver. In our case, by letting $\hat{n} = \left(n_x, n_y, n_z\right)$, the system takes the form:

$$\gamma \frac{\partial \hat{n}}{\partial t} - \nabla \cdot (K\nabla \hat{n}) + a\hat{n} = 0 \tag{4.23}$$

where

$$K = \begin{pmatrix} K & 0 & 0 \\ 0 & K & 0 \\ 0 & 0 & K \end{pmatrix}$$

$$\gamma = \begin{pmatrix} \gamma & 0 & 0 \\ 0 & \gamma & 0 \\ 0 & 0 & \gamma \end{pmatrix}$$

$$a = \begin{pmatrix} \mu\left(n_x^2 + n_y^2 + n_z^2 - 1\right)^2 & 0 & 0 \\ 0 & \mu\left(n_x^2 + n_y^2 + n_z^2 - 1\right)^2 & 0 \\ 0 & 0 & \mu\left(n_x^2 + n_y^2 + n_z^2 - 1\right)^2 \end{pmatrix}$$

By discretizing the spatial domain and applying time-stepping until a steady state was reached, COMSOL solves these coupled PDEs and provided the equilibrium director field. **Figure 4.6** illustrates the simulated director field of a nematic LC droplet printed on a planar alignment layer, with the planar orientation along the *x*-axis. In Figure 4.6(a), a top-down perspective clearly shows that the director near the droplet base was predominantly horizontal, reflecting the planar anchoring. As the director extends

toward the droplet surface, it progressively tilts and becomes nearly vertical close to the top interface.

Figure 4.6(b), viewed from the side, provides further insight into this vertical transition. A green dashed line marks a notable boundary along the central *y*-axis cross-section, where the director field switches orientation from pointing upward to pointing downward. The planar alignment at the substrate forces the LC director at the base to lie horizontally, while the free surface of the droplet, which tends to favour homeotropic alignment, imposes an opposing constraint. As the LC director adjusts between these two conditions, a region develops where the orientation must switch abruptly. This abrupt change often results in the formation of a defect line (or disclination), which is clearly marked by the green dashed line.

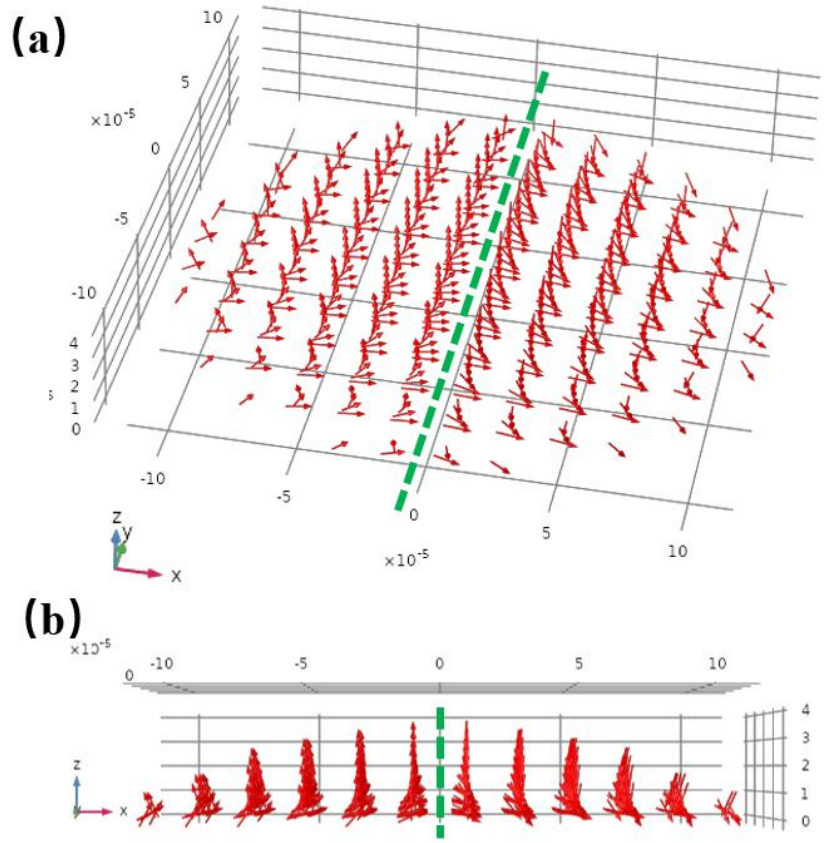


Figure 4.6 COMSOL simulation of the director distribution in a nematic LC droplet printed on a planar alignment layer (alignment along the *x*-axis). (a) Top view. (b) Side view. The green dashed line indicates the central *y*-axis where the director reverses direction either side of the line, suggesting a possible disclination line.

4.3 Printed Chiral Nematic LC Droplet

To gain further insight into the behaviour of CLC droplets, this section focuses on the experimental results obtained from printing and observing these droplets under controlled conditions. Building on the preceding theoretical and simulation analyses, the experimental investigation seeks to validate and expand upon the predicted internal director field and optical properties. By systematically varying the chiral dopant concentration and maintaining precise control over droplet deposition and alignment conditions, the study aims to establish a comprehensive understanding of how chirality

influences the structure and optical response of printed LC droplets.

4.3.1 Chiral nematic LC droplet on a homeotropic alignment layer

To minimize the impact of individual droplet variability and ensure reliable observations, we typically deposit a 10×10 array of droplets for each experiment. This approach allows for the identification of the most representative configuration for droplets of a specific size, chiral concentration, and alignment layer conditions. Using the MJ-AT-01-080 inkjet printing nozzle with a diameter of $80\,\mu m$, the droplet diameter can be controlled on the alignment layer to approximately $120 \pm 10\,\mu m$. Each droplet achieves a contact angle of $32.3°$ and a maximum height of $28.4\,\mu m$ (**Figure 4.7**).

To begin the study, a nematic LC (E7) was printed onto a homeotropic alignment layer coated onto a glass substrate. The alignment layer was prepared by spin-coating a 0.02 wt.% solution of lecithin in IPA onto clean glass substrates. This process ensured uniform homeotropic anchoring at the droplet-substrate interface. The printed droplets were then observed on a POM to analyse their optical characteristics.

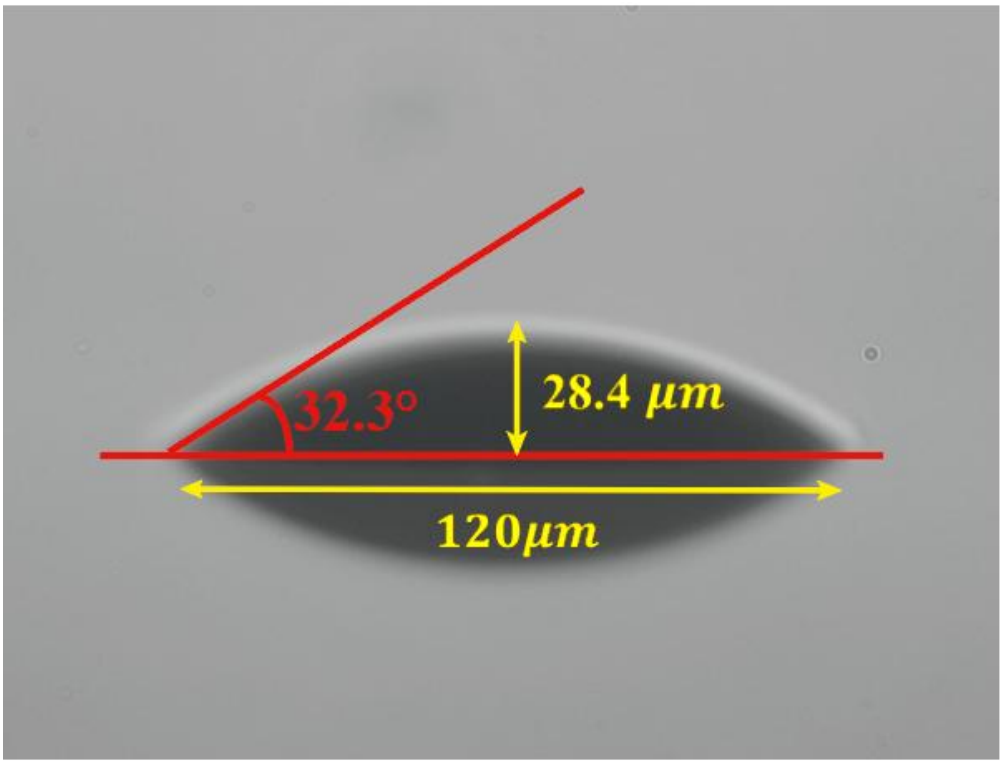


Figure 4.7 Shadowgraph image (Side view) of a nematic LC droplet printed onto a homeotropic alignment layer that was coated onto a glass substrate. The droplet dimensions were as follows: base diameter of 120 μm, height of 28.4 μm, and a contact angle of 32.3°.

Figure 4.8(a) shows a POM image of a printed nematic LC (E7) droplet under crossed polarizers. It closely matches the simulated pattern of a nematic droplet on a homeotropic alignment layer (Figure 4.8(b)), further validating the accuracy of the simulation and the reliability of our prediction of the director field within the droplet. Like the simulation, the image obtained from experiment shown in Figure 4.8(a) displays two orthogonal black crosses aligned with the polarizer axes, consistent with the homeotropic alignment at the substrate and the expected radial director configuration. This agreement highlights the robust correlation between the predicted and experimentally observed optical properties, affirming the effectiveness of the

simulation approach.

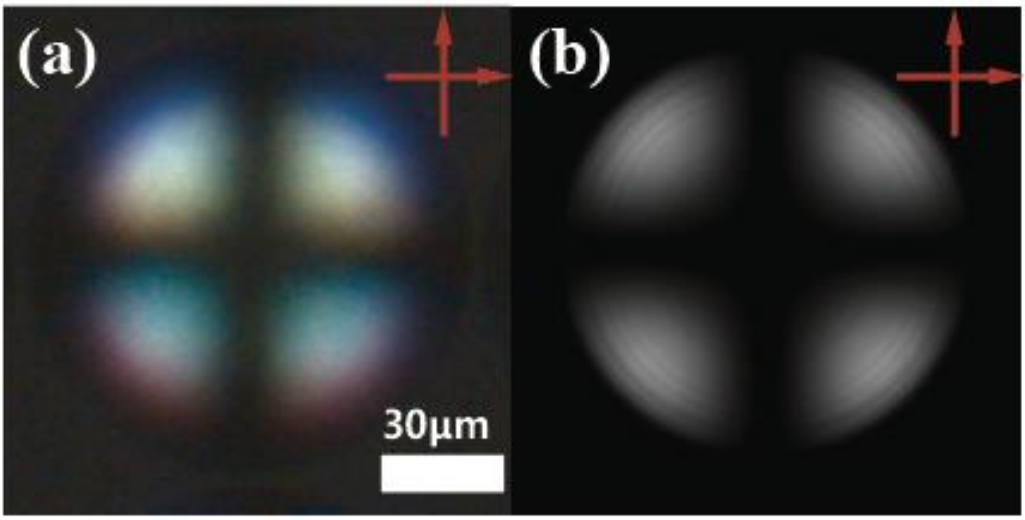


Figure 4.8 POM images of a printed nematic LC (E7) droplet deposited on a homeotropic alignment layer on a glass substrate. The characteristic black cross aligns with the polarizers' orientation, indicated by the single-headed red arrows. (a) Experimental result and (b) simulation result.

Next, experiments were carried out for printed CLC droplets (E7 and chiral dopant, R811) at concentrations of $0.1\,\text{wt.\%}\,\text{R811}$ and $0.4\,\text{wt.\%}\,\text{R811}$ with pitch of $100\,\mu\text{m}$ and $25\,\mu\text{m}$, respectively. Both mixtures were printed onto a homeotropic alignment layer, and the droplet size was controlled to a diameter of $120\,\mu\text{m}$ for all droplets in the array.

In **Figure 4.9**(a), the printed droplet of the $\text{E7} + 0.1\,\text{wt.\%}\,\text{R811}$ mixture is shown. A subtle clockwise spiral pattern is observed, indicating the onset of twist within the droplet. At this concentration, the introduction of R811 leads to a very long pitch chiral nematic, which induces a weak but detectable twist in the LC director field. This spiral formation arises as the chiral dopant induces a twist in the LC director field and occurs as the system minimizes its elastic free energy, with the chiral dopant favouring

a gradual director rotation across the droplet. The balance between the elastic resistance to deformation and the chiral torque imposed by R811 results in the formation of a nascent helical structure.

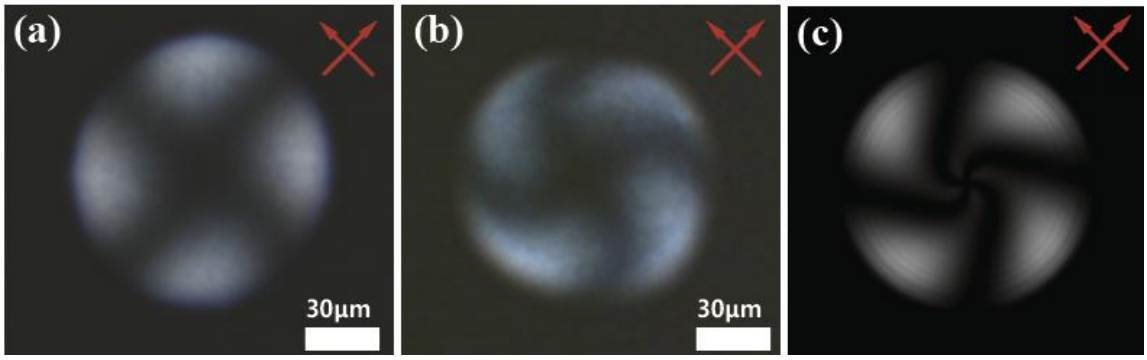


Figure 4.9 POM images (experiments and simulations) of printed chiral nematic LC droplets on a homeotropic alignment layer coated onto a glass substrate. (a) POM image of a droplet of $\mathrm{E7} + 0.1\ \mathrm{wt.\%}\ \mathrm{R811}$ ($P = 100\ \mu\mathrm{m}$), showing a weak clockwise spiral pattern. (b) POM image of a droplet $\mathrm{E7} + 0.4\ \mathrm{wt.\%}\ \mathrm{R811}$ ($P = 25\ \mu\mathrm{m}$) exhibiting a clear spiral structure. (c) Simulated POM image for a printed CLC droplet with a right-handed chiral dopant ($q_0 = -0.25\ \mu\mathrm{m}^{-1}$), reproducing the spiral texture observed in the experimental images. Single-headed red arrows indicate the polarizer and analyser orientations.

In Figure 4.9(b), the droplet printed with $\mathrm{E7} + 0.4\ \mathrm{wt.\%}\ \mathrm{R811}$ exhibits a significantly more obvious spiral structure. The increased concentration of R811 reduces the helical pitch, amplifying the twist throughout the droplet, resulting in a well-defined spiral pattern. This transition from a faint spiral at $0.1\ \mathrm{wt.\%}$ to a clear spiral at $0.4\ \mathrm{wt.\%}$ demonstrates the progressive influence of chirality on the director field as the system evolves toward an energy-minimized state. Moreover, the experimental observations and the simulation results are in close agreement. The simulated optical pattern (see Figure 4.9(c)) reproduces the spiral texture seen in the POM images, confirming that the imposed chiral dopant concentration consistently

modifies the LC director field. This strong correlation validates both the experiment and the simulation approach, reinforcing the conclusion that the evolution of the spiral structure is directly linked to the increasing chirality in the system.

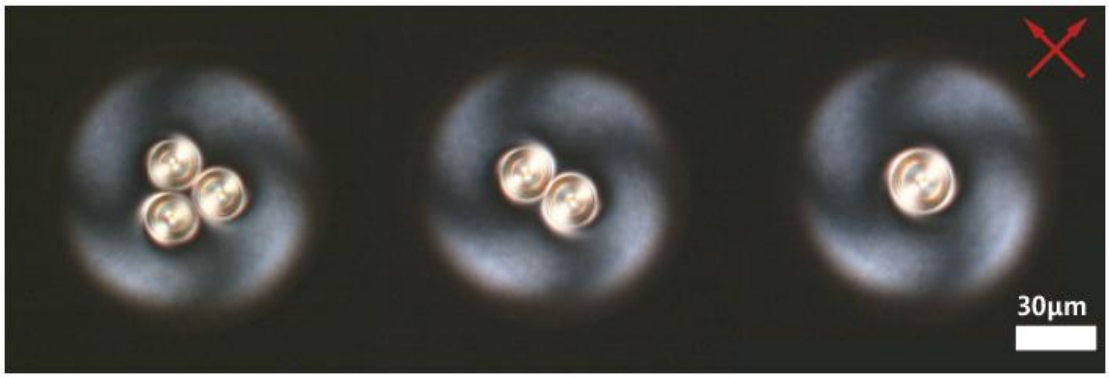


Figure 4.10 POM images of printed CLC droplets composed of $E7 + 0.5\ \text{wt.}\%\ \text{R811}$ ($P = 20\ \mu\text{m}$). The droplet diameter is $120\ \mu\text{m}$. The images show three possible configurations: droplets with three, two, or one bright circular region at the centre.

As the concentration of the chiral dopant (R811) further increases, the behaviour of the LC droplets becomes more complex. **Figure 4.10** shows the results for droplets composed of $\text{E7} + 0.5\ \text{wt.}\%\ \text{R811}$, where the pitch is reduced to $20\ \mu\text{m}$. The droplets, printed onto a homeotropic alignment layer and with a controlled diameter of $120\ \mu\text{m}$, reveal unique internal structures that differ significantly from those observed at lower concentrations, and are now no longer reproduced with the simulations presented in Section 4.2.3.

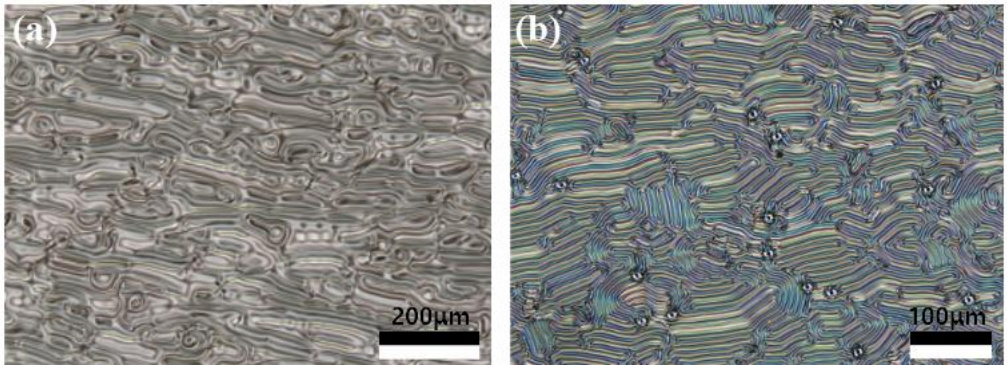


Figure 4.11 POM images of a CLC texture filled in glass cells with different alignment layers. (a) POM image of a homeotropic cell with thickness of 20 µm filled with E7 + 0.5 wt. % R811 ($P = 20$ µm). (b) POM image of a planar cell with thickness of 20 µm filled with E7 + 1 wt. % R811 ($P = 10$ µm) under electric field applied ($V = 14\ V_{pp}, f = 1$ kHz). These images show the characteristic fingerprint texture of the CLC phase, resulting from the helical arrangement of the director field.

At this concentration, a transition is observed where bright, circular structures emerge within the droplets. The formation of these circular features can be attributed to the mismatch between the bulk chiral twist and the homeotropic boundary conditions. This frustration arises because the chiral dopant imposes a helical twist in the LC director field, while the homeotropic anchoring constrains the director at the boundaries to align perpendicularly to the substrate. At this concentration, the helical pitch (20 µm) becomes smaller than the droplet height (28.4 µm), the LC director can no longer smoothly accommodate the twist across the confined geometry. These bright regions indicate localized increases in optical retardance caused by abrupt changes in the LC director orientation, resembling the fingerprint textures observed in **Figure 4.11**.

Figure 4.10 demonstrates three distinct configurations of these internal structures: droplets with one, two, or three bright circular regions. This variation arises due to small fluctuations in the thermal quenching process and the droplet's initial conditions during

printing. Inside the printhead, the LC mixture is heated to 70℃, a temperature above the clearing point of the nematic phase, ensuring that the material remains in the isotropic liquid state for reliable ejection and droplet formation. Upon deposition onto the substrate, the droplets rapidly cool to room temperature (20℃) due to thermal contact with the substrate surface. This rapid quenching induces a phase transition from the isotropic state back to the chiral nematic phase. The variation in the number of the internal structures arises due to small fluctuations in the cooling process and the droplet's initial conditions during printing. The most frequently observed configuration is a single bright circular region at the droplet centre, as this represents the most stable energy-minimized state. Droplets with two or three circular regions occur less often and appear to represent less energetically favourable states, in which the LC twist is divided into separate localized regions rather than forming a continuous, uniform pattern.

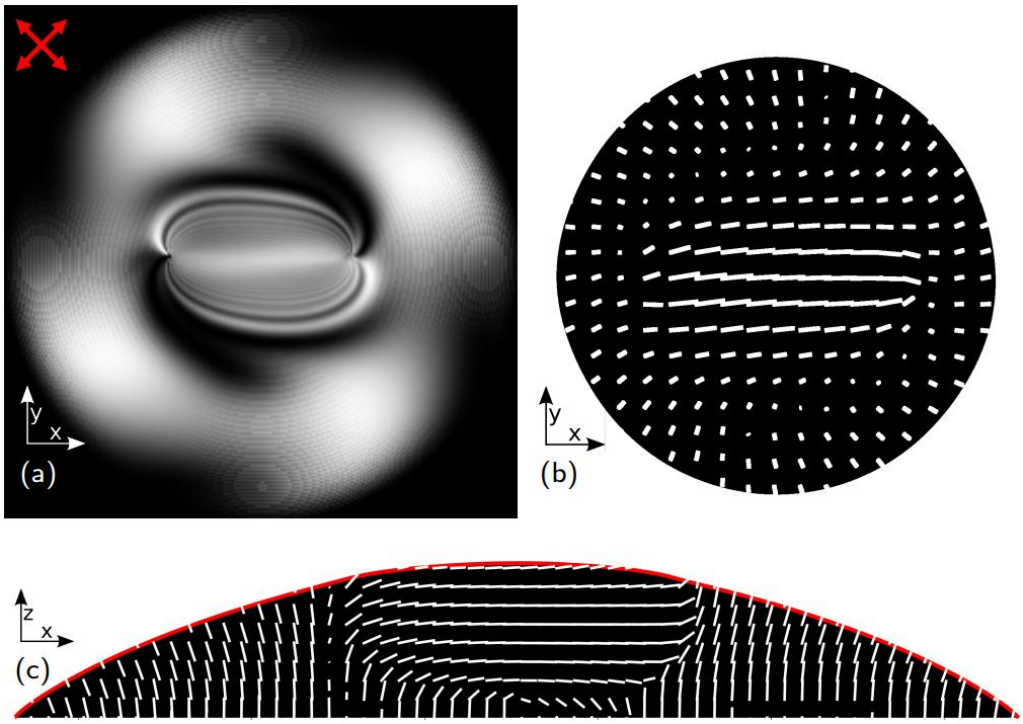


Figure 4.12 Q-tensor simulation results of a CLC droplet ($E7 + 0.5\,wt.\%\,R811$)**.** (a) Simulated POM texture under crossed polarizers, showing a bright localized structure. (b) Top view of the director field in the *x-y* plane, illustrating the helical twist. (c) Side view of the director field in the *x-z* plane, showing the vertical development of the chiral twist and its central localization. These results were obtained by Alva Orr.

The numerical simulations (**Figure 4.12**) confirm this behaviour, showing that as the pitch decreases relative to the droplet height, the LC director field evolves from a uniformly twisted homeotropic state to a configuration in which the inherent conflict between the natural chiral twist and the imposed boundary conditions is resolved by concentrating the twist into specific regions. In other words, instead of displaying a smooth, continuous twist, the droplet minimizes its overall elastic energy by concentrating the twist into discrete regions - frustration. These regions appear as sharp transitions or defect lines in the director field, which reflect the system's attempt to reconcile the natural chiral twist with the conflicting boundary conditions imposed by

the droplet geometry. The numerical simulations are provided by Alva C. J. Orr, as published in the article *Topologically Frustrated Structures in Inkjet Printed Chiral Nematic Liquid Crystal Droplets - Experiments and Simulations*. The simulation method is based on a Q-tensor method that can naturally handle defects, disorder, and isotropic-nematic phase transitions, which are challenging for traditional director-only models.

The Q-tensor method models LCs using a symmetric, traceless 3×3 matrix Q that encapsulates both the director and the degree of order. In a uniaxial nematic state, Q can be expressed as

$$Q = S\left(\hat{n} \otimes \hat{n} - \frac{1}{3}I\right), \tag{4.24}$$

where $\hat{n}$ is the director and S is the scalar order parameter. The total free energy of the system is given by the sum of bulk and surface energies:

$$F = \int_V (F_d + F_t + F_e) dV + \int_S F_s \, dS \tag{4.25}$$

The thermotropic energy F_t governs phase behaviour and has minima corresponding to either isotropic or nematic states, while the elastic energy F_d penalizes spatial variations in Q through gradient terms. An applied external field contributes an energy F_e that biases the orientation of Q. The equilibrium configuration is found by minimizing F, leading to a set of Euler-Lagrange equations for the independent components of Q. These nonlinear, coupled equations are typically solved numerically using methods such as finite elements or finite differences. A common approach is to

simulate the time evolution of Q using a gradient descent equation:

$$\gamma \frac{\partial Q}{\partial t} = -\frac{\delta F}{\delta Q}, \tag{4.26}$$

which ensures that the free energy decreases over time until a steady state is reached. Then, boundary conditions, either through strong anchoring or via a surface energy term F_s, are applied to model the influence of substrates. These simulations (**Figure 4.12**) reveal that the circular regions correspond to areas where the director aligns nearly parallel to the substrate, resulting in concentrated regions of twist.

Due to the spherical-cap geometry, the droplet exhibits a non-uniform thickness — being thicker at the centre and thinner near the edges. Because the formation of the helix requires a minimum thickness to complete its twist, the thicker central region supports a more fully developed helix. In contrast, the thinner regions near the edges limit the number of helical turns, resulting in a compressed helix. This spatial variation in thickness thus leads to a corresponding variation in the helical structure across the droplet. Due to the droplet's spherical-cap geometry, the edges are thinner than the centre. This reduced thickness at the edge region limits the extent to which the helix can develop, causing the twist distortion to be concentrated in the thicker central region.

At an even higher chiral dopant concentration of $\mathrm{E7} + 0.63\ \mathrm{wt.\%}\ \mathrm{R811}$, the behaviour of the CLC droplets becomes increasingly complex. The pitch at this concentration further decreases to $16\ \mu\mathrm{m}$. **Figure 4.13** shows POM images of droplets printed with this mixture, where the previously observed bright circular regions have

grown significantly. At this concentration, some of the internal structures begin to merge, forming interconnected and irregular patterns.

The further reduction in the helical pitch increases the frustration between the chiral twist and the homeotropic boundary conditions. This causes the twist to expand and redistribute within the droplet, resulting in the growth of localized distortions. As the pitch becomes smaller relative to the droplet height, the regions of concentrated twist can no longer remain isolated. Instead, they begin to merge, creating larger, interconnected domains.

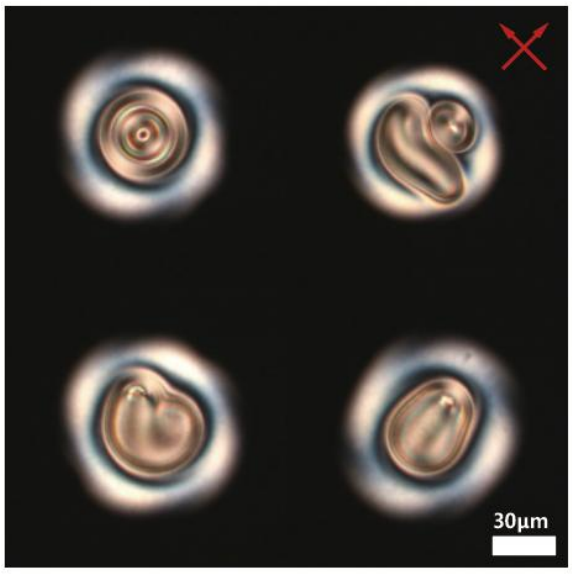


Figure 4.13 POM images of CLC droplets composed of 0.63 wt. % R811 ($P = 16$ µm).

As the concentration of the chiral dopant increases further, the internal structures of the CLC droplets undergo a significant evolution, gradually transitioning toward the fingerprint texture. **Figure 4.14**(a-d) present POM images of droplets composed of E7 mixed with 0.75 wt. % R811 ($P = 13.3$ µm), 1 wt. % R811 ($P = 10$ µm)

2 wt. % R811 ($P = 5$ µm), and 4 wt. %R811 ($P = 2.5$ µm) respectively. At these higher concentrations, the internal distortions grow increasingly elongated and interconnected, eventually forming the characteristic fingerprint-like patterns.

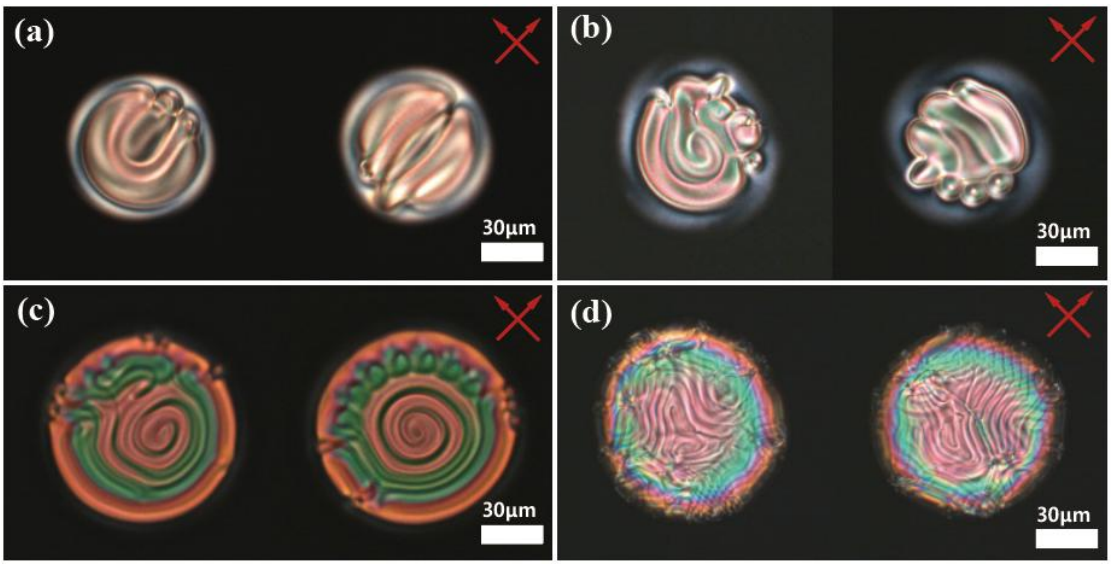


Figure 4.14 POM images of CLC droplets with increasing chiral dopant concentration: (a) E7 + 0.75 wt. % R811 ($P = 13.3$ µm), (b) E7 + 1 wt. % R811 ($P = 10$ µm), (c) E7 + 2wt. % R811 ($P = 5$ µm), and (d) E7 + 4 wt. % R811 ($P = 2.5$ µm).

For E7 + 0.75 wt. % R811 (Figure 4.14(a)), the localized structures observed at lower concentrations expand and elongate, starting to form more interconnected domains. For E7 + 1 wt. % R811 (Figure 4.14(b)), these regions become better defined, displaying increased alignment and periodicity. At higher concentrations, such as E7 + 2 wt. % R811 (Figure 4.14(c)) and E7 + 4 wt. % R811 (Figure 4.14(d)), the structures fully transition into the fingerprint texture, characterized by distinct and periodic stripe-like patterns (similar to Figure 4.11). This confirms that the localized distortions observed at lower concentrations are the precursors to the fingerprint texture. The increasing chirality reduces the pitch further, forcing the system into a tightly

modulated, periodic configuration.

Under polarized light, the high-contrast regions in the texture correspond to areas where the director is aligned parallel or perpendicular to the polarizers. Since these regions occur at intervals of half a helical turn, the stripe spacing in the fingerprint texture is expected to correspond to half of the helical pitch, $\frac{P}{2}$. However, experimental measurements reveal that the fingerprint texture exhibits a periodicity P_{eff} that is significantly longer than the intrinsic pitch P of the mixture.

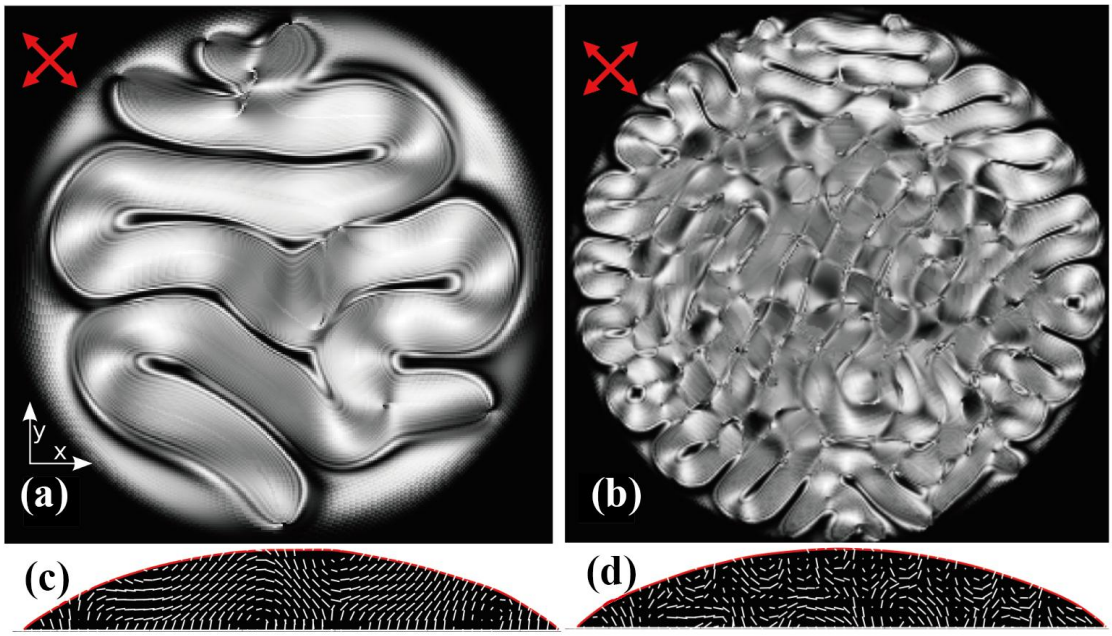


Figure 4.15 Q-tensor simulations results of CLC droplets. (a) and (b) show POM textures, illustrating the transition from irregular structures to a periodic fingerprint texture. (c) and (d) show cross-sectional director field configurations in the *x*-*z* plane. These results were obtained by Alva Orr.

According to the Q-tensor simulation results (**Figure 4.15**), the extended periodicity observed in the fingerprint texture can be attributed to distortions in the helix caused by the confined geometry of the droplet and the homeotropic anchoring at the

boundaries. In a spherical-cap droplet, the centre is thicker than the edges. Since a complete helical twist requires a certain minimum thickness, the thicker centre can accommodate more twists while the thinner edges cannot support as many. As a result, the helical structure appears to be more fully developed in the centre and compressed near the boundaries. This curvature-induced distortion leads to an effective redistribution of the twist, with thicker regions exhibiting an expanded pitch.

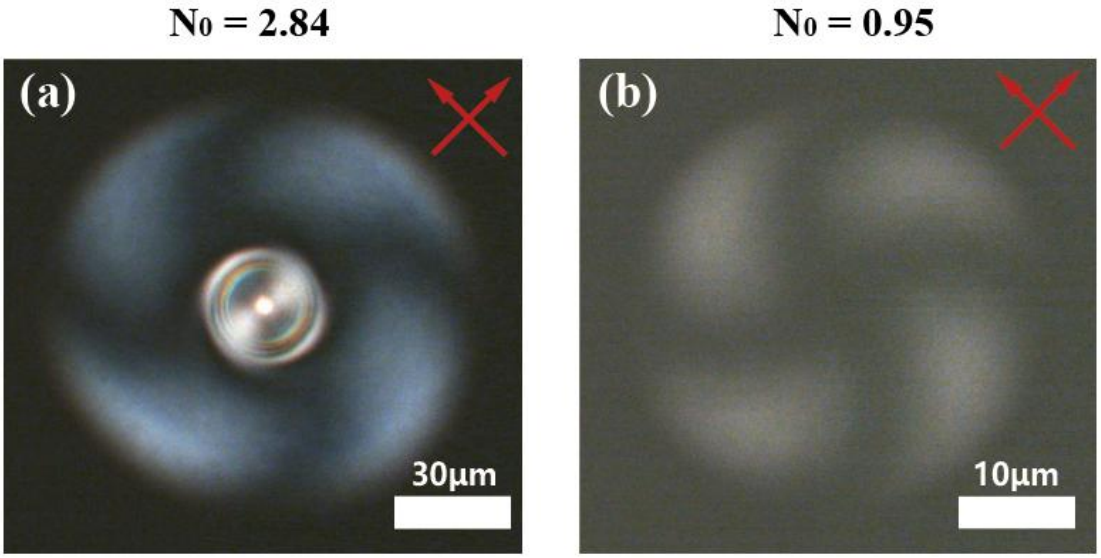


Figure 4.16 POM images (experiments) of printed CLC droplets composed of $E7 + 0.5$ wt. % R811 with different droplet size. (a) Droplet height: 28.3 μm, printed via inkjet printing ($N_0 = 2.84$); (b) Droplet height: 9.5 μm, printed via EHD printing ($N_0 = 0.95$).

Figure 4.16 presents POM images of CLC droplets composed of the same mixture, $E7 + 0.5$ wt. % R811 ($P = 20$ μm), but with differing droplet sizes. In Figure 4.16(a), the droplet has a height of 28.3 μm, while in Figure 4.16(b), the droplet has a significantly smaller height of 9.5 μm. Both droplets maintain the same contact angle, ensuring that the difference in their internal structures arises purely from their differing dimensions. The larger droplet in Figure 4.16(a) was printed using inkjet printing, while

the smaller droplet in Figure 4.16(b) was printed using EHD printing, as such small dimensions cannot generally be achieved using conventional inkjet printing techniques. Despite being prepared from the same mixture, the two droplets exhibit entirely distinct optical patterns. This difference highlights the influence of droplet size on the internal configuration of the chiral nematic phase.

To quantify the effect of droplet size on the observed structures, it is necessary to introduce the concept of a helicity parameter, N_0, which characterizes the relationship between the pitch of the CLC mixture and the geometric confinement imposed by the droplet. In spherical droplets, N_0 provides a dimensionless measure of how the twist interacts with the enclosing geometry. Specifically, N_0 is defined as:

$$N_0 = \frac{2h}{P}, \tag{4.27}$$

where h is the height of the droplet, and P is the pitch of the chiral nematic phase. The parameter N_0 tracks the ratio of the length scale over which the chiral nematic naturally twists by π to the characteristic size of the confining droplet. A larger N_0 indicates that multiple chiral twists can fit within the droplet, whereas a smaller N_0 signifies that the droplet's dimensions are too small to accommodate the full development of the helix.

The helicity parameter N_0 provides a comprehensive framework to analyse and classify the behaviour of CLC droplets across a wide range of conditions, allowing for the development of a regime diagram. **Figure 4.17** illustrates this regime, showcasing

droplets composed of CLC mixtures printed onto a homeotropic alignment layer, with N_0 values spanning from 0 to 22.64. The images demonstrate how the internal structures of the droplets evolve systematically as N_0 increases, offering a unified perspective on the interplay between droplet geometry, confinement, and the pitch.

At low N_0 values (e.g., $N_0 = 0$ and $\mathrm{N}_0 = 0.566$) optical textures reflect the suppression of the twist within the droplet. For $N_0 = 0$, where the material is purely nematic ($P = \infty$), the observed structure is a basic cross pattern. When a small degree of chirality is introduced, as in $N_0 = 0.566$, the twist begins to develop but remains highly constrained by the droplet geometry, resulting in weak distortions.

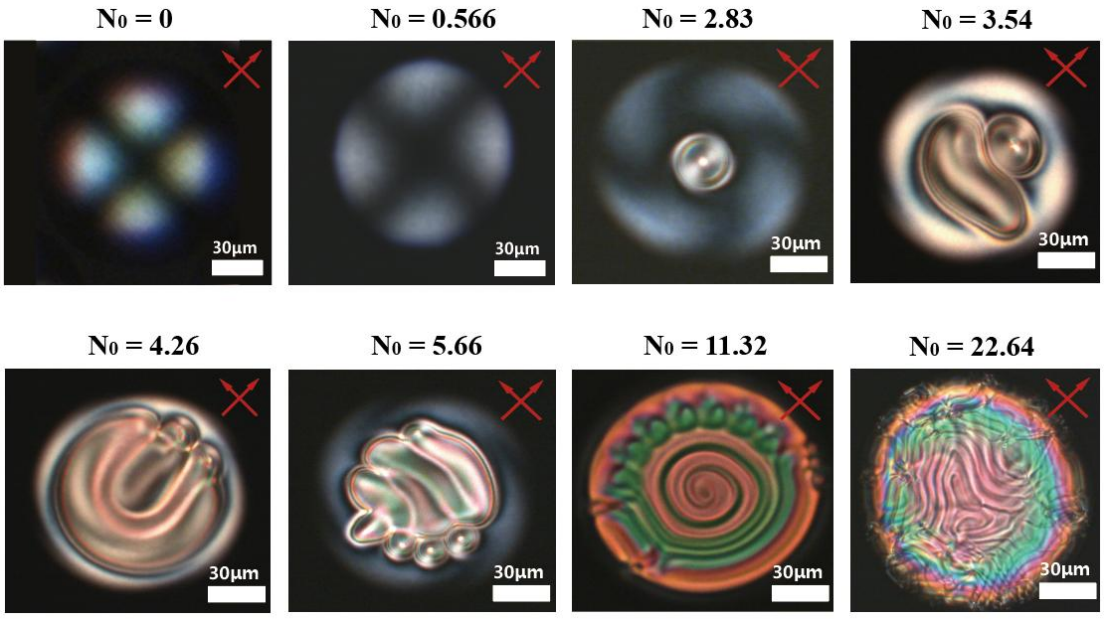


Figure 4.17 POM images (experiments) of CLC droplets printed on a homeotropic layer with varying helicity parameters (N_0), illustrating the evolution of the internal director profile.

As N_0 increases to intermediate values (e.g., $N_0 = 2.83$ and $\mathrm{N}_0 = 3.54$), the helix becomes more prominent within the droplet, giving rise to distinct optical patterns. The development of periodic modulations is evident, but these structures are still

influenced by boundary constraints and exhibit incomplete fingerprint textures. By $N_0 = 4.26$ and $N_0 = 5.66$, the chiral nematic phase adapts to the geometric confinement more effectively, forming more defined and continuous modulations. The periodicity and complexity of these patterns continue to increase as the droplet accommodates multiple twists. At larger N_0 values (e.g., $N_0 = 11.32$ and $N_0 = 22.64$), the fingerprint texture is fully developed, with periodic stripe patterns clearly observed across the droplet.

4.3.2 Chiral nematic LC droplet on a planar alignment layer

The following section presents the experimental results of CLC droplets deposited on a planar alignment layer, where the helicity parameter N_0 is used as a key metric to characterize the director configurations. Based on the previously discussed regimes, a series of images for a range of printed droplet condition were acquired under crossed polarizers to illustrate the evolution of the director field as N_0 increases from 0 to 24 (**Figure 4.18**).

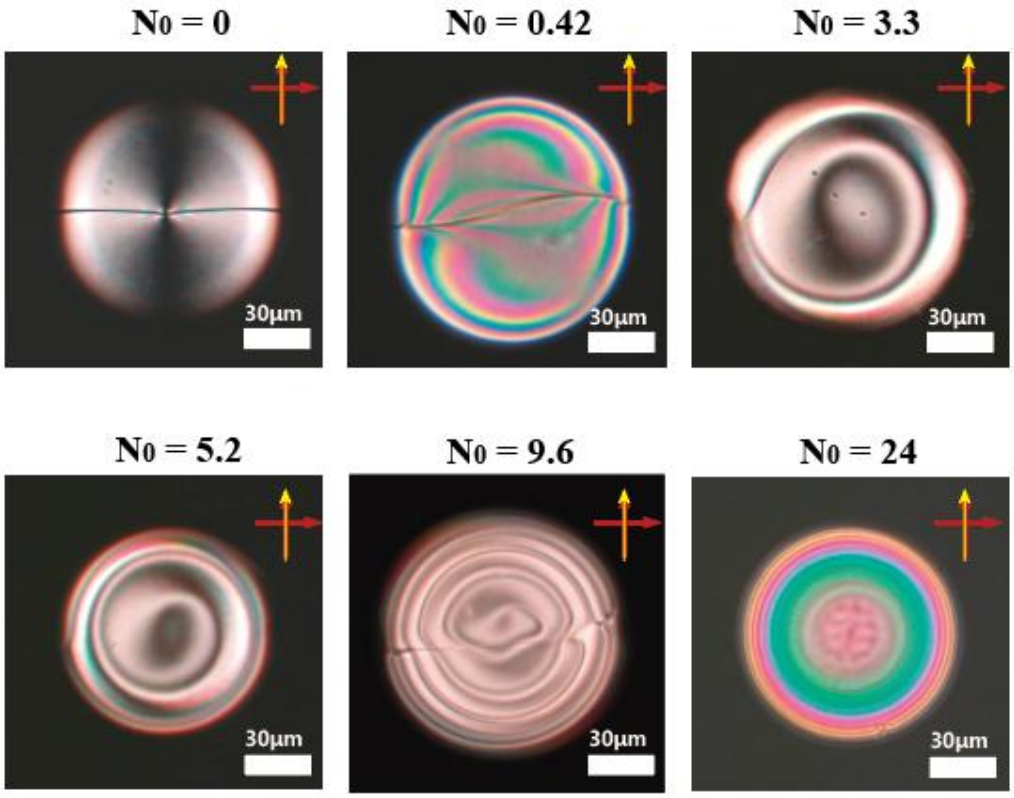


Figure 4.18 POM images of CLC droplets printed on a planar alignment layer with varying helicity parameters (N_0), illustrating the evolution of the internal director profile.

When $N_0 = 0$, no chiral dopant is present, and the droplet behaves as an achiral nematic. In this state, a thin horizontal line is observed running through the centre of the droplet, perpendicular to the planar anchoring direction (indicated by the single-headed yellow arrow). This line corresponds to the region where the director orientation reverses — a feature consistent with our simulation results presented in Figure 4.6. The upper and lower regions of the droplet display a gradual darkening, indicative of a smooth tilt in the director orientation towards the polarizer, while the left and right sides remain relatively uniform. As chiral dopant is added, even at low concentrations (e.g., $N_0 = 0.42$), the central disclination line begins to distort. The previously straight line

now exhibits a slight twist, indicating that the director field is starting to adopt a helical configuration. With further increases in N_0 (for example, at $N_0 = 3.3$), this defect line is progressively displaced towards the periphery of the droplet, and a spiral-like structure becomes evident in the central region. The observed changes suggest that the director field undergoes a continuous transformation from a simple nematic alignment to a more complex twisted state as the chiral dopant concentration increases. At even higher values of N_0 (such as $N_0 = 5.2$ and $N_0 = 9.2$), the spiral distortion becomes more pronounced, with the number of visible turns increasing and the defect line being pushed further outward. At $N_0 = 24$, the spiral structure is extremely dense, signifying that the internal director field has undergone substantial twisting and that the helical pitch is very short.

Although a direct simulation of chiral nematic droplets on planar substrates remains beyond our current capability, the experimental results and the previously discussed nematic simulation suggest a mechanism due to 'pitch jumps'. As described in Section 3.5.2, a CLC confined in a height-varying geometry can exhibit discrete changes in the number of helical pitches at critical thicknesses. In the droplet geometry, the surface curvature naturally creates a height profile that is largest at the centre and decreases radially outward. In an achiral nematic droplet, the director near the substrate is essentially horizontal, while it tilts toward the vertical as it approaches the curved free surface (Figure 4.6).

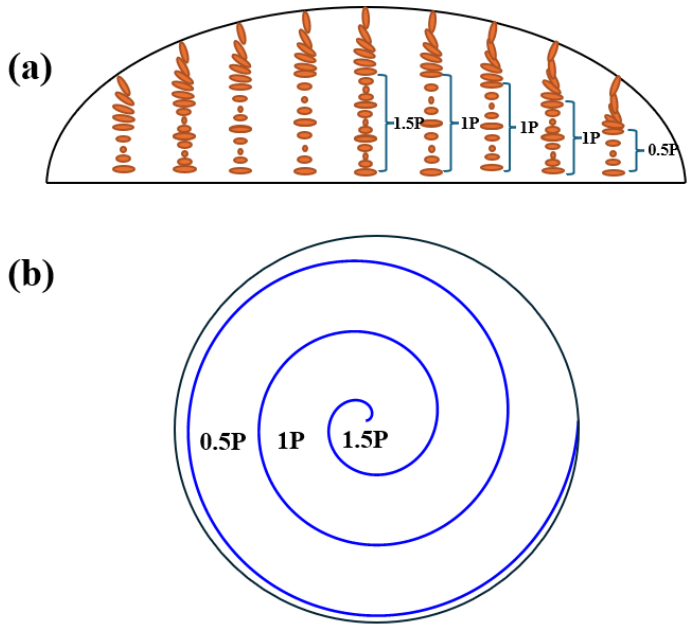


Figure 4.19 Conceptual schematic of a CLC droplet on a planar alignment layer. (a) Side-view cross-section illustrating discrete pitch jumps (e.g., 0.5P, 1P, 1.5P) at critical thicknesses. (b) Top-down view showing a spiral defect line, hypothesized to minimize elastic energy by distributing the twist helically.

Once chirality is introduced, the director at the droplet's surface is initially constrained to be perpendicular to the local curvature by the anchoring conditions. However, moving deeper into the droplet, the influence of this surface condition gradually diminishes, allowing the intrinsic chirality to dominate. In these inner regions, the director field forms a helical structure, with the helix pitch varying according to the local droplet thickness. As illustrated schematically in **Figure 4.19**(a), the droplet's vertical thickness covers several segments of the intrinsic pitch, resulting in discrete jumps in the local twist. Viewed from above, these discontinuities manifest as disclination lines. Rather than forming concentric rings, the disclination lines tend to be in a lower-energy arrangement by winding into a spiral pattern, as suggested in Figure

4.19(b). Such a spiral arrangement reduces elastic distortions along the droplet boundary and allows the director field to transition smoothly between different helical regions. Consequently, as the chiral dopant concentration increases and the pitch shortens, the spiral pattern tightens, and the disclination lines become more numerous.

4.4 Summary

This chapter has investigated the internal director configurations of printed CLC droplets under different alignment conditions and chiral dopant concentrations. For droplets on homeotropic alignment layers, the director field transitions smoothly from a vertical orientation at the centre to a radial arrangement near the surface at low dopant levels, whereas at high concentrations the structure evolves into the characteristic fingerprint texture. In contrast, droplets on planar alignment layers exhibit more complex behaviour, experimental observations suggest that discrete pitch jumps lead to the formation of spiral defect structures within the droplet. These findings highlight the significant influence of both geometric confinement and chiral dopant concentration on the internal structure of CLC droplets, thereby providing a robust theoretical framework that will support subsequent investigations in this thesis. The following chapter builds on this framework by employing printed droplets with tailored internal configurations to generate structured light fields and to explore their application, including the use of full Poincaré beams for polarization detection.

Chapter 5

Printed LC Droplets for Structured Light Generation

"You can't control the wind, but you can adjust your sails."

Popular proverb

5 Printed LC droplets for structured light generation

5.1 Introduction

In this chapter, I will explore the generation of complex structured light based on printed LC droplets, a term that refers to electromagnetic fields with specific spatial distributions of phase and polarization[98]. In this context, complex beams with non-uniform polarization distributions, known as vector beams, have become crucial in modern optics[99-102]. They play essential roles in applications including quantum information processing, optical trapping and manipulation, and high-density optical data storage[103-107]. Equally important are beams with helicoidal phase fronts, referred to as vortex beams, which usually carry orbital angular momentum (OAM)[108-110] and have been demonstrated to be useful in modern optical communications[111, 112], super-resolution microscopy[113, 114], and optical tweezers[115-117]. When both the polarization and phase structures are combined, the resulting beams are known as vector vortex beams (VVBs)[118-128], which further expand the capabilities and applications of structured light.

LC spatial light modulators (SLMs) are widely used to generate VVBs by manipulating both phase and polarization[129-134]. However, achieving spatially varying phase and polarization typically requires complex optical setups that often incorporate multiple SLMs[129, 135], which significantly increases both the cost and the technical

complexity of the system. As an alternative, passive components have been investigated for generating VVBs, offering lower energy consumption and reduced costs. Examples of such passive components include Q-plates[136, 137], metasurfaces[123, 138, 139], glass cones[128], and GRIN lenses[119-121, 140-142]. While these methods provide advantages such as high precision and customization, they are frequently challenged by issues such as complex fabrication processes, high production costs, or the need for bulky optical assemblies.

Recently, micro-droplet printing technology has gained significant attention due to its ability to precisely pattern complex functional fluids at the microscale on various substrates[29]. This method enables rapid and efficient fabrication of a wide range of "inks," thereby significantly enhancing production throughput. As a result, micro-droplet printing is increasingly employed to deposit diverse materials, including organic light-emitting substances, particle suspensions, conductive polymers, and metalloids, which broadens its industrial and technological applications[77, 143-146]. Despite these advantages, one aspect of micro-droplet printing that has been less explored is its intrinsic spatially varying birefringence, which arises from the unique director configurations within the LC droplets.

Traditionally, such spatial variation in birefringence has been regarded as a limitation, particularly in the creation of functional microlenses[76]. Rather than viewing the spatially varying birefringence of LC droplets as a drawback, in this project, I

exploit it for the generation of diverse structured light fields. By harnessing micro-droplet printing, I deposit LC droplets onto substrates treated with different alignment layers. The understanding of how droplet geometry, anchoring, and chirality determine internal configurations, established in Chapter 4, guides the selection of droplet designs for generating specific structured light fields in this work. The structured light generated by these printed droplets includes beams that exhibit skyrmionic structures with two units of OAM, beams with azimuthal or radial polarization patterns, and beam with polarization singularities. This approach provides a simple and compact method for generating complex structured light using LC droplets. In doing so, it not only paves the way for novel LC droplet designs but also expands the range of potential applications in optical manipulation and information processing. The results presented in this chapter have been submitted for publication in *Advanced Optical Materials*.

5.2 Fundamental Concepts in Optics

In view of the extensive optical content in the following chapters, I will introduce the fundamental principles that govern the interaction of light with anisotropic media such as LCs. The section explains the basic nature of light (polarization and phase), and how these properties evolve when light encounters various optical elements. In addition, I will discuss methods to measure and interpret these effects, offering a foundation that supports the detailed optical experiments and analyses presented later in this thesis.

5.2.1 Polarization and phase

Light is an electromagnetic wave, and its behaviour can be described by the electric field if we only consider the corresponding response from matter. For a beam propagating in the *z*-direction, the oscillations of the electric field occur in the xy-plane, which is perpendicular to the direction of propagation[147]. In the spatial domain, the electric field of a monochromatic wave can be expressed as a function of z and time t using an exponential form. At a given initial position $z = z_0$ and time $t = t_0$, the electric field can be written as

$$\begin{aligned}\vec{E}(z,t) &= \vec{E}(z_0,t_0)\exp\left[i\left(\frac{2\pi}{\lambda}(n+ik)z-\omega t+\delta_E(z_0,t_0)\right)\right]\\ &= E_x(z,t)\vec{\boldsymbol{x}} + E_x(z,t)\vec{\boldsymbol{y}}\\ &= E_x(z_0,t_0)\exp\left[i\left(\frac{2\pi}{\lambda}(n+ik)z-\omega t+\delta_x(z_0,t_0)\right)\right]\vec{\boldsymbol{x}}\\ &+ E_y(z_0,t_0)\exp\left[i\left(\frac{2\pi}{\lambda}(n+ik)z-\omega t+\delta_y(z_0,t_0)\right)\right]\vec{\boldsymbol{y}}\end{aligned} \tag{5.1}$$

where $\vec{E}(z_0,t_0)$, and $\delta_E(z_0,t_0)$ are the initial electric field and phase, respectively. For the components in xy-plane, $E_x(z_0,t_0)$, $E_y(z_0,t_0)$ and $\delta_x(z_0,t_0)$, $\delta_y(z_0,t_0)$ are their amplitudes and phases initially, ω is the angular frequency, and $k = \frac{2\pi}{\lambda}$ is the wave number.

The disturbance of a plane time-harmonic wave in the xy-plane may occur in

different ways. If the electric field oscillates along a single, fixed direction, the wave is linearly polarized. If the electric field vector rotates continuously at the wave frequency, tracing out a circle when the amplitudes of the x and y components are equal or an ellipse when they are unequal, the wave is circularly or elliptically polarized. If the oscillations occur in a disorganized way, the light is said to be depolarized[148, 149].

For a fully polarized beam, the SoP is determined by the amplitudes of the x and y components and the phase difference $\delta = \delta_y(z_0, t_0) - \delta_x(z_0, t_0)$. When the amplitudes are equal, a phase difference of $0°$ or $180°$ leads to linear polarization at $45°$ or $-45°$ relative to the x-axis. A phase difference of $\pm 90°$ results in circular polarization, and any other phase difference produces elliptical polarization[148].

5.2.2 Jones vectors and Stokes vectors

Jones vectors offer a concise mathematical representation of a polarized state of a light beam[148-151]. In this formalism, when a beam interacts with an optical interface — the plane of incidence is clearly defined by the beam direction and the surface normal. In these cases, the electric field can be decomposed into two orthogonal components: the *p*-polarized component (parallel to the plane of incidence) and the *s*-polarized component (perpendicular to the plane of incidence)[152]. The electric field can be expressed as

$$\vec{E}(z,t) = E_p + E_s = A_p e^{i\phi_p}\,\hat{\boldsymbol{p}} + A_s e^{i\phi_s}\,\hat{\boldsymbol{s}}, \tag{5.2}$$

and the corresponding Jones vector is defined as

$$\vec{J} = \begin{pmatrix} E_p \\ E_s \end{pmatrix} = \begin{pmatrix} A_p e^{i\phi_p} \\ A_s e^{i\phi_s} \end{pmatrix}. \tag{5.3}$$

This representation naturally incorporates both the amplitude and the phase of the field.

In many practical situations, light is only partially polarized or even completely depolarized[148-150]. In these cases, the electric field's trajectory in the chosen xy-plane becomes partially or entirely disordered during propagation. This increased disorder means that simply specifying two complex numbers is insufficient to capture the complete statistical behaviour of the light field[148, 150]. To overcome this limitation, the Stokes vector is used. The Stokes vector is a four-element real vector defined in terms of measurable intensities:

$$\vec{S} = \begin{bmatrix} S_0 \\ S_1 \\ S_2 \\ S_3 \end{bmatrix} = \begin{bmatrix} \langle E_p {E_p}^* + E_s {E_s}^* \rangle \\ \langle E_p {E_p}^* - E_s {E_s}^* \rangle \\ \langle E_p {E_s}^* + E_s {E_p}^* \rangle \\ i\langle E_p {E_s}^* - E_s {E_p}^* \rangle \end{bmatrix} = \begin{bmatrix} I_p + I_s \\ I_p - I_s \\ I_{45^\circ} - I_{-45^\circ} \\ I_R - I_L \end{bmatrix}. \tag{5.4}$$

In this formulation, S_0 represents the total intensity of the light beam, while S_1 quantifies the difference in intensities between the parallel and perpendicular polarizations. The parameters S_2 and S_3 represent the differences in intensity between orthogonal polarization components, with S_2 quantifying the difference between $+45°$ and $-45°$ linear polarization and S_3 quantifying the difference between right and left circular polarizations. These intensities — I_p, I_s, I_{45°, $-I_{45^\circ}$, I_R, and I_L — are obtained through measurements that average the light intensity over time, thus inherently incorporating the statistical nature of the electric field.

For a fully polarized beam, both the Jones vector and the Stokes vector completely characterize the SoP, but they present the information in different forms. The Jones vector, composed of complex amplitudes, captures both the magnitude and the relative phase between two orthogonal polarization components. The Stokes vector, obtained from four intensity measurements, conveys the same information through its elements: S_0 gives the total intensity, while S_1, S_2, and S_3 encode the amplitude difference and the sine and cosine of the relative phase between the components. In this representation, the degree of polarization (*DOP*) is defined as

$$DOP = \frac{\sqrt{{S_1}^2+{S_2}^2+{S_3}^2}}{S_0} \tag{5.5}$$

and for a fully polarized beam, $DOP = 1$. However, for partially polarized or depolarized light, the DOP is less than one[148-150]. In these cases, the Stokes vector represents the beam as an incoherent superposition of a completely polarized component and an unpolarized component.

When a monochromatic light beam propagates, its electric field vector in the xy plane can trace an elliptical path if a phase difference exists between its x and y components. For example, a phase delay $\delta = \delta_y(z_0, t_0) - \delta_x(z_0, t_0)$ between its components[149]. In **Figure 5.1**(a), the lengths of the ellipse's major and minor axes can be identified within the dotted rectangle, while the solid box indicates the outer boundary of the ellipse when projected onto the x and y axes. The parameters χ and φ are used to describe the ellipticity, and the orientation of the major axis,

respectively[149, 152].

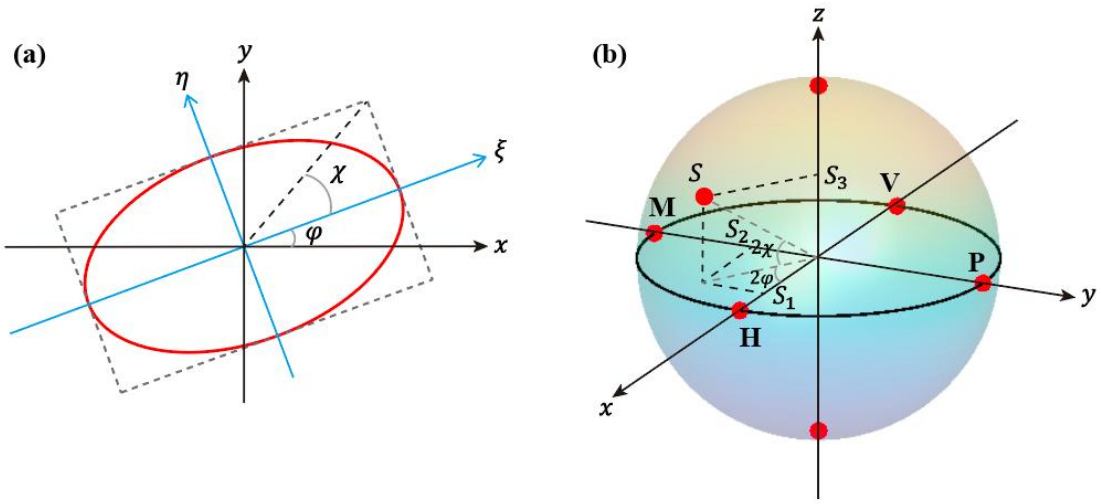


Figure 5.1 The Polarization ellipse and Poincaré sphere. (a) The Polarization ellipse to represent the SoP of light. (b) Poincaré sphere to represent the SoP of light.

In Figure 5.1(b), the same SoP are represented on the Poincaré sphere, which is a three-dimensional coordinate system defined by the normalized Stokes parameters $\left(\frac{S_1}{S_0}, \frac{S_2}{S_0}, \frac{S_3}{S_0}\right)$. Standard SoPs, such as horizontal (H), vertical (V), $\pm 45°$ (M and P), and left-handed or right-circular (L and R), appear at distinct locations on the sphere's surface[149, 152]. The coordinates of any point on the surface of the sphere can be related back to the ellipse parameters in the xy plane, allowing one to move seamlessly between the geometric description of the polarization ellipse and the more global view offered by the Poincaré sphere.

5.2.3 Vectorial light responses

In linear optics, when a fully polarized light beam interacts with an optical element or material, its SoP undergoes a transformation that can be completely described by a

2×2 Jones matrix (JM)[149, 153]. In the Jones formalism, a fully polarized beam is represented by a two-component complex vector, and the action of an optical system is modelled as a linear transformation on this vector. Specifically, if the input beam is described by the Jones vector, then the output beam after passing through an optical element is given by

$$\vec{J}_{out} = J\vec{J}_{in}, \tag{5.6}$$

where $J = \begin{pmatrix} J_{pp} & J_{ps} \\ J_{sp} & J_{ss} \end{pmatrix}$ is the JM[149]. Each element J_{ij} in this 2×2 complex matrix represents the effect of the optical element on the corresponding polarization component. The JM not only accounts for amplitude changes and phase shifts but also preserves the absolute phase information of the beam. Since the matrix contains four complex elements, it possesses eight real degrees of freedom. This full description is particularly important in applications where details of the input and output vectorial beams, including their absolute phases, must be accurately represented.

When using the Stokes vector, the transformation of a light beam's SoP is described by a 4×4 matrix known as the Mueller matrix (MM)[154]. In this formalism, the light's SoP is represented by a four-element Stokes vector, and when light interacts with an optical object, the object's optical properties are characterized by its Mueller matrix M. The transformation is expressed as

$$\vec{S}_{out} = M\vec{S}_{in} = \begin{pmatrix} m_{11} & m_{12} & m_{13} & m_{14} \\ m_{21} & m_{22} & m_{23} & m_{24} \\ m_{31} & m_{32} & m_{33} & m_{34} \\ m_{41} & m_{42} & m_{43} & m_{44} \end{pmatrix} \cdot \vec{S}_{in}, \tag{5.7}$$

where $\vec{S}_{in}$ is the input Stokes vector and $\vec{S}_{out}$ is the output Stokes vector after the light passes through the object.

5.2.4 Mueller matrix decomposition methods

In optical systems, a retarder is an element that has a fast axis and an orthogonal slow axis[155]. When polarized light of a given frequency passes through a retarder, the component of the light that is aligned with the fast axis propagates more quickly than the component aligned with the slow axis, which introduces a relative phase difference between these two components[156]. This phase difference alters the overall SoP; in the Poincaré sphere representation, it appears as a rotation of the polarization vector along the surface of the sphere.

A common method for extracting the retarder properties — specifically, the retardance (i.e., the phase difference between the light components aligned with the fast and slow axes) and the fast axis orientation (i.e., the direction along which the light experiences the least phase delay) — from a measured MM is the Mueller matrix polar decomposition (MMPD) proposed by Lu and Chipman in 1996[157]. In this approach, the measured Mueller matrix M is decomposed into three submatrices corresponding to depolarizer, retarder, and diattenuator effects:

$$M = M_D M_R M_\Delta, \tag{5.8}$$

where M_D is the diattenuator matrix, M_R is the retarder matrix, and M_Δ is the

depolarizer matrix. The diattenuator matrix M_D characterizes the differential attenuation of orthogonal SoPs, effectively describing how the sample preferentially absorbs light based on its polarization orientation. The retarder matrix M_R quantifies the phase delays introduced between orthogonal polarization components as light propagates through the material. Finally, the depolarizer matrix M_Δ describes the extent to which the sample depolarizes the incident light, representing the loss of polarization purity due to scattering or other randomizing processes. The retarder submatrix is typically expressed in block form as

$$M_R = \begin{pmatrix} 1 & 0 \\ 0 & m_R \end{pmatrix} \tag{5.9}$$

with m_R being a 3×3 rotation matrix that represents the effect of the retarder on the state of polarization. The overall retardance δ, which quantifies the phase difference between the fast and slow axes, is determined by treating m_R as a rotation matrix and is given by

$$\delta = cos^{-1}\left[\frac{tr(m_R)-1}{2}\right] \tag{5.10},$$

where $tr(m_R)$ denotes the trace of the matrix m_R, defined as the sum of its diagonal elements. This fast axis corresponds to the SoP that experiences the greatest phase change. To find its orientation, the rotation axis S_R, which is by definition the fast axis of the retarder, can be determined by calculating the eigenvector of m_R (with subscript starting from 1) by applying Eq. (5.12) and Eq. (5.13):

$$a_i = \frac{1}{2\,sin\,\delta}\sum_{j,k=1}^{3} \varepsilon_{ijk}\,(m_R)_{jk}, \tag{5.11}$$

$$\vec{S}_R = (1, a_1, a_2, a_3)^T, \tag{5.12}$$

where ε_{ijk} is the Levi-Civita symbol. The fast axis of a retarder corresponds to a certain SoP on the Poincaré sphere. Light with this SoP undergoes the fastest phase change when passing through the retarder.

5.3 Fabrication of LC droplets

In this project, LC droplets were prepared using the processes described in Chapters 3 and 4. For all printed droplets in this chapter, I employed the nematic LC mixture E7 (Synthon Chemicals Ltd), which is characterized by a moderate birefringence (Δn) of approximately 0.21-0.26 at visible wavelengths at room temperature, and exhibits positive dielectric anisotropy[158]. In the case of chiral nematic droplets, the low twisting power chiral dopant, R811 ((R)-2-Octyl 4-[4-(Hexyloxy)benzoyloxy] benzoate; Merck KGaA), used in the previous chapter, was added to E7 at various concentrations as detailed later.

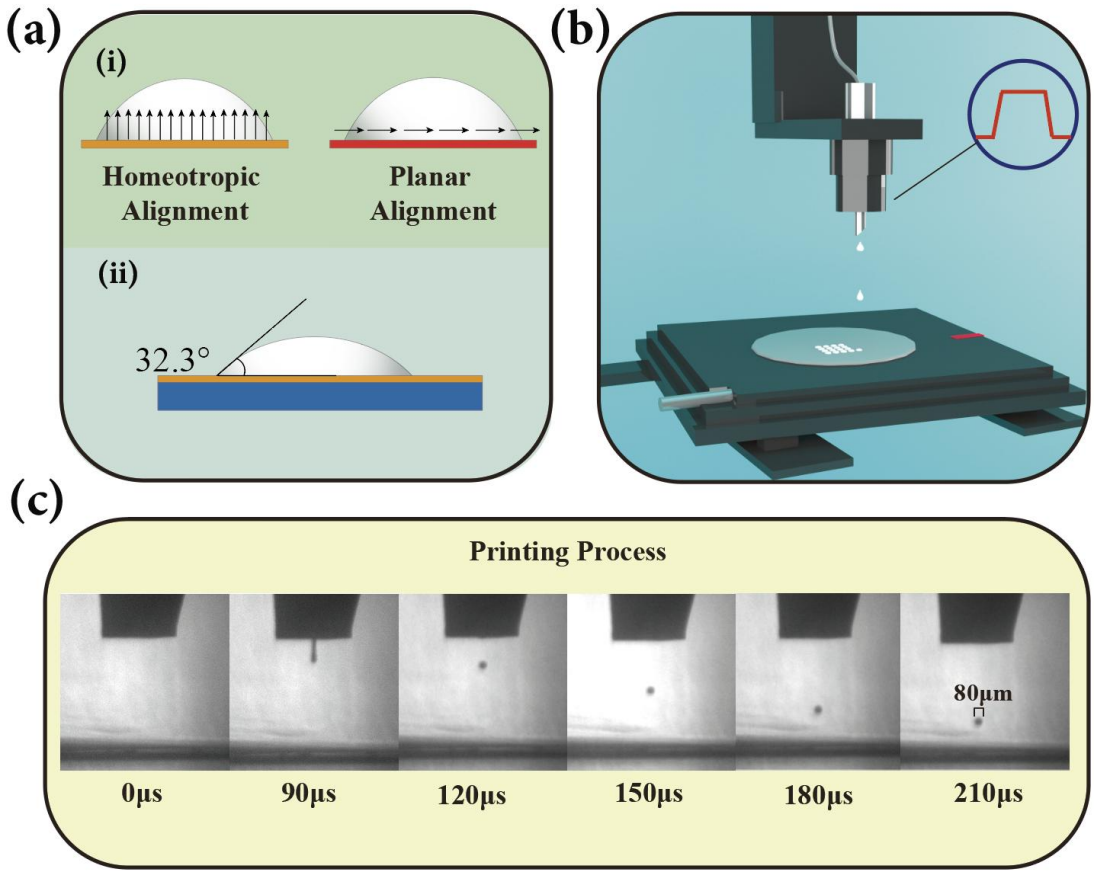


Figure 5.2 Schematic representation and visualization of the LC droplet array printing process. (a) (i) Side-view schematic illustrating how planar and homeotropic alignment layers dictate the LC-glass interface orientation, thereby influencing the droplet alignment. (ii) Side-view illustration of a series of LC droplets positioned on a glass substrate with an alignment layer, depicting the droplet's spherical cap shape and contact angle of 32.3°. (b) Diagram of the inkjet printing process, in which an applied voltage deforms the piezoelectric printhead, generating pressure waves that eject LC droplets through the nozzle (see Chapter 3). (c) Time-lapse shadowgraph images showing the morphological evolution of the LC droplets in air at intervals of 30 μs during printing.

The substrate preparation follows the procedures described in Section 3.2.2. Briefly, for homeotropic alignment, a 0.02 wt.% lecithin solution in IPA was spin-coated onto the substrate at 1200 rpm, whereas for planar alignment, a PVA solution was spin-coated and then baked at 70℃ for 30 seconds before being mechanically rubbed to

establish a preferential direction. Regardless of the substrate treatment, the air/LC interface naturally favours homeotropic alignment. In the experiments, the LC droplet samples consisted of a matrix of droplets with a contact angle of 32.3°, all deposited on a treated transparent glass substrate, as illustrated in **Figure 5.2**(a).

The fabrication of the droplets was achieved using the DoD inkjet printing process illustrated in Figure 5.2(b) (and discussed in detail in the previous chapters), which is well-suited to efficient and reliable mass production. In this process, the MicroFab Jetlab II system equipped with the MJ-AT-01-080-8MX printhead featuring an 80 μm nozzle was employed. The printing was driven by a trapezoidal voltage waveform, ensuring precise droplet deposition. The system was controlled by a computer, which allowed for high automation and precise adjustment of both the printing location and droplet size. An XY-motorized stage was used to achieve accurate positioning, with a separation of 150 μm between each droplet.

During printing, the printhead was maintained at a temperature of 70 ℃, which is above the clearing point (58 ℃) of E7. Operating at this temperature keeps the LC in the isotropic phase, reducing the viscosity and facilitating effective droplet formation, as depicted in Figure 5.2(c). Each droplet was formed with an in-flight diameter of roughly 80 μm and a volume of around 180 picolitres, retaining a spherical shape as it travelled through the air. For applications requiring larger droplets on the surface, multiple droplets were deposited at the same location to control the overall size.

5.4 Vectorial Optical Characterization of LC Droplets

To characterize the vectorial properties of the LC droplets, I utilized two methods — Mueller polarimetry and Mach-Zehnder interferometry. Mueller polarimetry was employed to study the polarization characteristics of the LC droplets, enabling polarization information to be obtained through decomposition of the MM. To examine the phase properties, a Mach-Zehnder interferometer was used, which provided accurate measurements of phase variations induced by the droplets. In the following sections, the details of both experimental platforms, including their configurations and operational principles are introduced.

5.4.1 Mueller polarimetry

Mueller polarimetry is an optical technique for fully characterizing how an optical sample alters the SoP of incident light by measuring its complete 4×4 MM[159], the schematic diagram is shown in **Figure 5.3**. In our system, a 633 nm He-Ne laser light source (HNLS008L-EC, Thorlabs) was used, and the light was first modulated by a polarization state generator (PSG) that consisted of a fixed polarizer (P1; LPVISC050, 510 – 800 nm, Thorlabs) and a rotating quarter-wave plate (QWP1; WPQSM05-633, 633 nm, Thorlabs). The modulated light, with a well-defined state of polarization, then illuminated the sample under investigation. After interaction with the sample, the emerging light is analyzed by a polarization state analyser (PSA), which included another rotating quarter-wave plate (QWP2; WPQSM05-633, 633 nm, Thorlabs) and a

second fixed polarizer (P2; LPVISC050, 510 – 800 nm, Thorlabs). The final SoP was recorded by a camera (DCC1545M, 1280 × 1024, Monochrome Sensor, Thorlab) that serves as the detector. The two QWPs rotate continuously at fixed speeds such that the rotation angle of QWP1, ϕ_1, is related to that of QWP2, ϕ_2 (for example, $\phi_1 = 5\phi_2$).

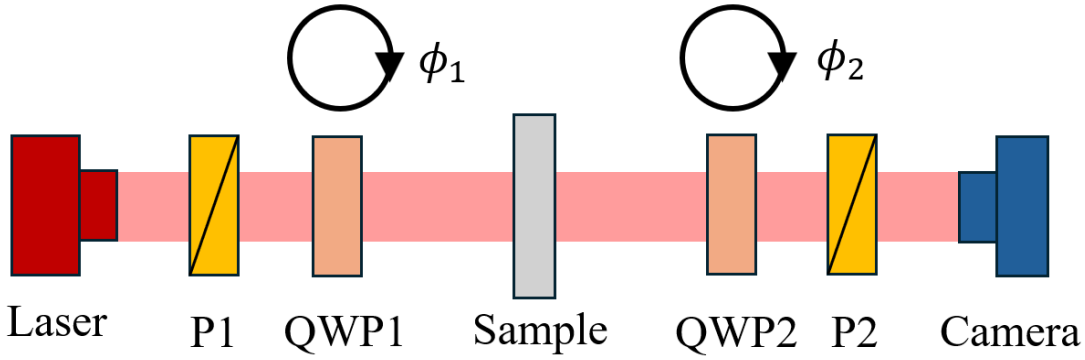


Figure 5.3 Schematic of the MM imaging polarimetry system. Light from a He-Ne laser passes through a fixed polarizer (P1) and a rotating quarter-wave plate (QWP1), interacts with the sample, and then is analyzed by another rotating quarter-wave plate (QWP2) and a second fixed polarizer (P2) before being recorded by the camera. The angles ϕ_1 and ϕ_2 indicate the rotation of QWP1 and QWP2, respectively.

As the waveplates rotate, the output intensity fluctuates according to the combined modulation effect of both plates. These periodic fluctuations can be analysed using Fourier analysis to separate the different harmonic signals that correspond to the various elements of the MM. In other words, the different rotational speeds ensure that the transmitted intensity contains distinct periodic features that facilitate the reconstruction of all 16 MM elements[160].

For each measurement, the overall system, represented by the product of the Mueller matrices of the individual components, transforms the input Stokes vector $\vec{S}_{in}$ into the output Stokes vector $\vec{S}_{out}$ according to

$$\vec{S}_{out}^{(q)} = M_{P2} M_{QWP2}^{(q)} M_{Sample} M_{QWP1}^{(q)} M_{P1} \vec{S}_{in} \tag{5.13}$$

where the superscript q indicates the measurement corresponding to a specific QWP1 angle. Since the intensity of the light is given by the first element S_0 of the output Stokes vector, the measured intensity $I^{(q)}$ is recorded for each setting. As QWP1 rotates continuously, the output intensity becomes a periodic function of its angle. This periodicity allows the intensity to be expressed as a Fourier series:

$$I^{(q)} = a_0 + \sum_{n=1}^{12} \left(a_n \cos\left(2n\phi_1^{(q)}\right) + b_n \sin\left(2n\phi_1^{(q)}\right) \right) \tag{5.14}$$

where a_n and b_n are the Fourier coefficients that describe the modulation of the intensity due to the continuously changing orientation of QWP1. These Fourier coefficients are directly related to the contributions of the various elements of the sample's MM. By extracting the coefficients from the measured intensity data, one can reconstruct the full 16-element MM of the sample. This complete MM provides a comprehensive description of the sample's polarization response, thereby enabling a systematic analysis of how the sample (the printed LC droplet) modulates the SoP[161-163].

5.4.2 The Mach-Zehnder Interferometer

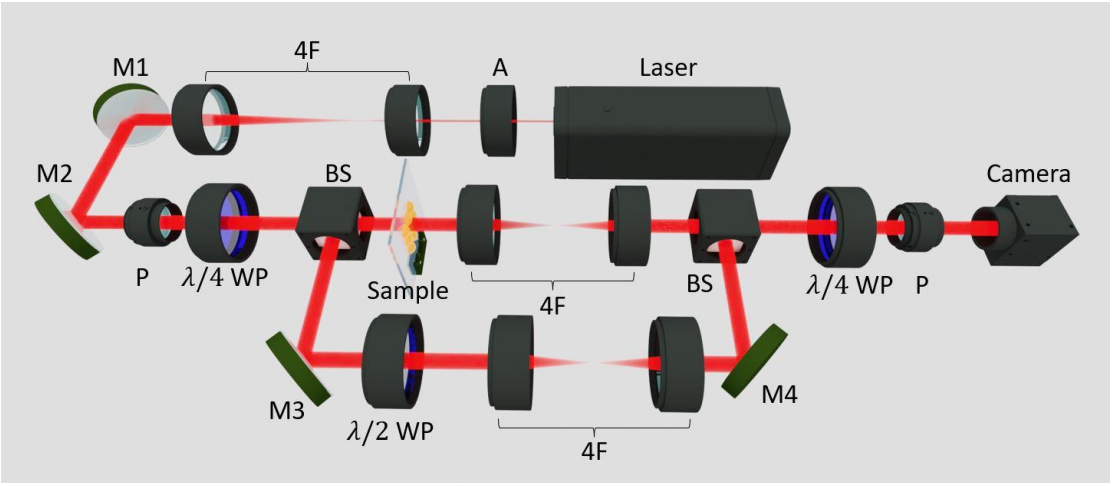


Figure 5.4 Diagrammatic representation of the Mach-Zehnder interferometer assembly used to characterize the structured light generated the LC droplet array. A collimated, polarized laser beam is split into sample and reference arms; the sample arm passes through the droplet array, while mirrors and waveplates in the reference arm match its path length and polarisation. The two beams recombine to form interferograms recorded by the camera.

The Mach-Zehnder interferometer is a well-established optical instrument used to study the phase properties of materials[164-166]. In our system (see **Figure 5.4**), a 633 nm He-Ne laser beam (HNLS008L-EC, Thorlabs), after passing through an attenuator, was expanded by a two-lens 4*f* (AC254-100-A-ML, $f = 100$ mm, ARC: 400-700 nm, Thorlabs) optical system and adjusted to be parallel and collimated using two mirrors (BB03-E02, 400-750 nm, Thorlabs). The beam was then converted to left circular polarization using a PSG composed of a polarizer (LPVISC050, 510- 800 nm, Thorlabs) and a QWP (WPQSM05-633, 633 nm, Thorlabs). Afterward, a beam splitter (BS043, 400-700 nm, Thorlabs) directs part of the beam (the signal arm) through the LC droplet array on a glass substrate, while the other part (the reference arm) bypasses the sample. Each arm is subsequently imaged by its own 4*f* system.

By design, the signal arm's beam undergoes a phase shift due to the droplet array's refractive index and thickness variations, whereas the reference arm remains unaffected. When the two beams recombine at the second beam splitter, any phase difference introduced by the droplet array manifests as a change in the interference pattern. This pattern, captured by the camera (DCC1545M, 1280 ×1024, Monochrome Sensor, Thorlabs), encodes the local phase information of the LC droplets. The PSA after the BS enables precise control and filtering of the beam's SoP, thus reducing noise and ensuring that only the desired polarization components are measured.

In essence, the interference fringes are extremely sensitive to phase changes, so even small variations caused by the droplets will shift or distort these fringes. By analysing these shifts, we can quantitatively determine the droplet's optical path difference (OPD), revealing its refractive index distribution or thickness profile. The ability to detect and measure small phase differences is exactly what enables the Mach-Zehnder interferometer to examine the phase properties of the LC droplet array.

5.5 Results and Discussion

Based on the methods described above for investigating polarization and phase properties, I analysed three distinct types of printed LC droplets: (1) nematic LC droplets on a homeotropic alignment layer, (2) nematic LC droplets on a planar alignment layer, and (3) long-pitch chiral nematic LC droplets on a planar alignment layer. Each droplet type exhibits different birefringence spatial distributions, inducing

different polarization and phase modulation.

5.5.1 Printed nematic LC on homeotropic alignment layer

A full Poincaré beam is a type of structured light that maps every SoP on the Poincaré sphere to distinct spatial locations in the beam's cross-section. Notably, the skyrmionic beam is a special case of the full Poincaré beam, and it is characterized by topological textures that arise from spatially varying SoPs[167-171]. In this experiment, a nematic LC droplet of the E7 mixture deposited on a homeotropic alignment layer is investigated. When circularly polarized light is used as the input, the droplet modulates both the phase and polarization of the transmitted light. As a result, the emergent beam exhibits a skyrmionic structure, carrying two units of OAM.

To investigate the optical properties of the nematic LC droplet on a homeotropic alignment layer, the droplet was first observed on a POM. As shown in **Figure 5.5**a(i), the droplet exhibits a characteristic “two dark brushes” pattern intersecting at the centre. These dark regions occur where the local LC director is oriented in such a way that its optical axis coincides with the orientation of the crossed polarizers, thereby blocking the passage of light. By contrast, the brighter regions indicate areas where the LC director’s orientation deviates from that of the polarizers, allowing more light to be transmitted[172]. This pattern, similar to the one described in Section 4.3.1, demonstrates how the droplet’s spatially varying birefringence modulates the polarization of transmitted light, thus revealing the structure of the droplet’s director configuration.

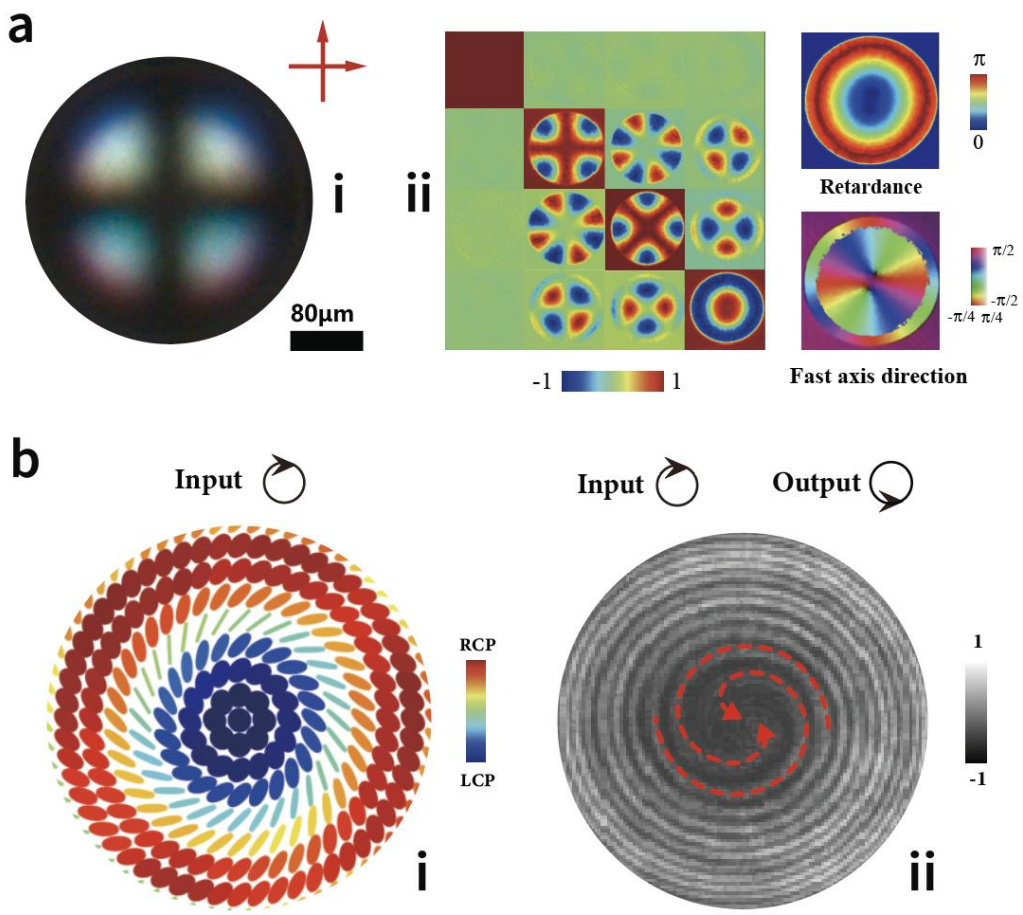


Figure 5.5 Experimental results demonstrating the modulation of light by a printed nematic LC droplet on a glass substrate coated with a homeotropic alignment layer. a(i) POM image of the printed droplet (diameter = 253 μm, height = 56 μm, contact angle ≈ 32°, temperature = 23℃). The single-headed red arrows represent the orientations of two polarizers. a(ii) The MM characterizes the droplet's full optical response, where each sub-panel represents the spatial distribution of one MM element, arranged according to the conventional 4×4 MM structure. The MM decomposition reveals the effective linear retardance and fast axis direction of the droplet. The retardance profile shows concentric rings, while the fast axis direction exhibits a radial symmetry, both indicating a vertical alignment with a gentle tendency for the LC director to align radially within the droplet. The fast axis was characterized using the Hue-Saturation-Luminance model: hue represents the elliptical axis orientation; luminance indicates the degree of ellipticity. The retardance distribution is represented using the colour bar, with values ranging from 0 to π. b(i) When right-handed circularly polarized light is incident on the droplet, the resulting polarization pattern demonstrates a full Poincaré beam (also exhibiting skyrmionic structure), showcasing a continuous transition of SoPs. The different colours in the pattern represent varying SoPs, with blue indicating left circular polarization and red indicating right circular polarization. The interference pattern in b(ii) illustrates the modulated light carrying two units of OAM. The spiral wavefront pattern is clearly visible, and the red dashed lines depict the shape of a light beam with two units of OAM.

The corresponding MM, shown in Figure 5.5a(ii), provides a complete description of the droplet's vectorial optical properties. Using a MM imaging polarimeter based on the dual rotating waveplates method, the LC droplets were measured to yield the MM of each sample. Since the MM is defined through the linear mapping between normalized Stokes vectors, whose components satisfy $S_i/S_0 \leq 1$, all MM elements are intrinsically constrained to the range [−1, 1]. By applying the MMPD method, detailed profiles of the retardance and fast-axis orientation were extracted from the measured data, as illustrated in the two subplots on the right side of Figure 5.5a(ii). Because the droplet acts as a continuous birefringent medium, it was modelled using an elliptical retarder instead of separating the effects into distinct circular and linear retarders. This approach more accurately represents the droplet's non-layered structure and captures the overall polarization modulation along the light propagation path. The retardance profile reveals a series of concentric rings, with retardance increasing from the centre outward, reaching a maximum near the droplet's edge, and then decreasing slightly. In addition, the fast-axis orientation profile exhibits radial symmetry, with the orientation varying smoothly as a function of the angular position around the centre. It is important to note that some abrupt changes in the fast-axis orientation map are not physical but are artifacts from the arctan calculation in the MMPD process, which has a limited range of $(-90°, 90°)$ and produces artificial $180°$ jumps when the true orientation crosses this boundary. Combining the information from both the retardance and fast-axis orientation maps, we can predict that the light emerging from the droplet contains

all possible SoPs, forming a full Poincaré beam.

Figure 5.5b(i) demonstrates the polarization pattern produced by a LC droplet when illuminated with right circularly polarized light. The output beam, identified as a full Poincaré beam, displays a continuous and smooth transition of SoPs across its cross-section. Moving radially outward, the polarization transitions from circular left-handed at the centre to elliptical, gradually evolving into a linear state at positions corresponding to the Poincaré sphere's equator. Beyond this region, the polarization shifts back to circular with reversed handedness, so that the beam's edges exhibit right-circular polarization. In the outermost region, where the measured retardance reaches its maximum and then decreases, the SoP gradually shifts from circular back toward an elliptical form. Overall, the observed polarization pattern confirms the generation of a full Poincaré beam.

The analysis of the droplet’s phase modulation reveals that the effective fast axis rotates twice around the azimuth, suggesting that the droplet generates two units of OAM when illuminated with circularly polarized light. To verify this, the Mach-Zehnder interferometer was employed as introduced previously. In this configuration, right-handed circularly polarized light from the PSG interacts with the droplet, while the left-handed circularly polarized light is filtered by the PSA. The interference pattern (see Figure 5.5b(ii)) produced displays a spiral structure, with two distinct red dashed lines outlining the spiral. The presence of two spiral arms directly indicates an OAM

order of two, as spiral interference patterns typically arise from the combination of a vortex phase and a spherical phase difference between the interfering beams. Although the reference beam is a plane wave, the observed spiral pattern confirms that the beam emerging from the droplet carries both vortex-like and spherical-like phase components. This observation verifies that the droplet functions as a 2-OAM generator and also introduces lens-like aberrations in the transmitted light. Since a ring-type interference pattern appears only when a vortex beam interferes with a spherical reference, yet our reference wave is planar, therefore, the droplet itself has added the spherical (and high order spherical) curvature.

In our experiment, right-handed circularly polarized light was used as the input state while the PSA was configured to transmit only the left-handed circularly polarized component. Utilizing JM formalism, the generation of complex VVBs with specific OAM characteristics can be demonstrated. A light beam possessing a helicoidal phase-front, described by $e^{il\theta}$, where θ is the azimuthal angle and l is an integer representing the number of full phase rotations around the beam's axis[173]. This means that when completing a full rotation around the beam's axis, its phase increases by $2\pi l$. The JM for a nematic LC droplet deposited on a homeotropic alignment layer can be considered to be similar to the JM for a GRIN lens, since according to Figure 5.5a(ii) they exhibit the same MM[141]. The JM in this case can be expressed as

$$\vec{J}_{drop} = \frac{1}{2}\begin{bmatrix} J_{11} & J_{12} \\ J_{21} & J_{22} \end{bmatrix} = \begin{bmatrix} sin^2(\theta) + \alpha\, cos^2(\theta) & (\alpha - 1)\, sin(\theta)\, cos(\theta) \\ (\alpha - 1)\, sin(\theta)\, cos(\theta) & cos^2(\theta) + \alpha\, sin^2(\theta) \end{bmatrix}, \quad (5.15)$$

where θ is the fast axis direction of the equivalent waveplate which equals the azimuthal angle in a cylindrical coordinate system, and α is related to, Γ, the linear retardance of the equivalent waveplate at the position (r, θ) [$\alpha = e^{i\Gamma} = \cos(\Gamma) + i\sin(\Gamma)$].

For this two units of OAM generation experiment, right-circularly polarized light I was used as the input SoP, E_{in} in right-circular eigenpolarization base:

$$\vec{E}_R = \frac{1}{\sqrt{2}}\begin{bmatrix}1\\ i\end{bmatrix}. \tag{5.16}$$

Using this input SoP, the output after passing through the droplet can be calculated by multiplying the input vector with the JM of the droplet, which takes the form

$$\vec{E}_{out} = \vec{J}_{drop}\begin{bmatrix}1\\ i\end{bmatrix} = \begin{bmatrix}\big(sin^2(\theta) + \alpha\, cos^2(\theta)\big) + i\big((\alpha-1)sin(\theta)cos(\theta)\big)\\ \big((\alpha-1)sin(\theta)cos(\theta)\big) + i\big(cos^2(\theta) + \alpha\, sin^2(\theta)\big)\end{bmatrix}. \tag{5.17}$$

For clarity, this can be denoted as follows:

$$\vec{E}_{out} = \vec{J}_{drop}\begin{bmatrix}1\\ i\end{bmatrix} = a_1\begin{bmatrix}1\\ i\end{bmatrix} + a_2\begin{bmatrix}1\\ -i\end{bmatrix}, \tag{5.18}$$

where $a_1 = \frac{1}{2}\left(e^{i0} + e^{i\Gamma}\right)$ and $a_2 = \frac{1}{2}\left(e^{i\,(2\theta+\pi)} + e^{i\,(2\theta+\Gamma)}\right)$. In this experiment, I project the output state onto the left-circular eigenpolarization base. The left-circular polarization eigenstate is defined as:

$$\vec{E}_L = \frac{1}{\sqrt{2}}\begin{bmatrix}1\\ -i\end{bmatrix}. \tag{5.19}$$

When a left-circular PSA is applied, it effectively filters out the component of the output state that does not match the left-circular polarization, so we would only get the $a_2\begin{bmatrix}1\\ -i\end{bmatrix}$ term from Eq. (5.19), which can be written as:

$$a_2 \begin{bmatrix} 1 \\ -i \end{bmatrix} = \frac{1}{2}\left(e^{i(2\theta+\pi)} + e^{i(2\theta+\Gamma)}\right)\begin{bmatrix} 1 \\ -i \end{bmatrix} = Ae^{i(2\theta+\varphi)}\begin{bmatrix} 1 \\ -i \end{bmatrix}, \qquad (5.20)$$

where $A(r)$ is the amplitude distribution, and $\varphi(r)$ is the initial phase delay determined by the retardance profile $\Gamma(r)$. The phase term $e^{i(2\theta+\varphi)}$ shows that the output beam acquires a phase shift of 2θ, which is characteristic of a beam carrying two units of OAM. This phase shift is crucial for confirming that a nematic LC droplet deposited onto a homeotropic alignment layer can be effectively used as a spin-to-OAM converter.

5.5.2 Printed nematic LC on planar alignment layer

Printed nematic LC droplets on planar alignment layers were examined for their ability to generate radially and azimuthally polarized beams. The planar alignment forces the LC director at the substrate to lie parallel to the surface, while the air/LC interface favours homeotropic alignment. This interplay produces a spatially varying birefringence that modulates the SoP of the transmitted light, resulting in output beams with either radial or azimuthal polarization. Such structured beams are particularly useful in super-resolution imaging techniques like stimulated emission depletion (STED) microscopy and other super-resolution imaging techniques, which can increase resolution beyond the diffraction limit[174-176].

A POM image of the printed droplet, shown in **Figure 5.6**a(i), reveals a darker vertical band and brighter horizontal regions, indicating that the director within the droplet predominantly tilt vertically (as discussed in more detail in Section 4.3.2). This

configuration results in minimal light transmission in the vertical direction, while the horizontal axis appears brighter between crossed polarizers. Figure 5.6a(i) presents the MM polarimeter results obtained via MMPD analysis. The retardance map exhibits symmetry about the horizontal line, with opposite values on either side. This pattern indicates that the LC droplet's internal director orientation undergoes an inversion across this boundary (as discussed in Section 4.2.4). In practical terms, if linearly polarized light is incident on the droplet, the region with positive retardance will impart a phase shift in one direction, while the region with negative retardance will impart an equal but opposite phase shift.

Having established the polarization-modulating capability of the LC droplet, we next examined how it influences both polarization and optical phase under different incident polarization conditions. Specifically, using vertically and horizontally aligned input light, the droplet produced azimuthal and radial polarization patterns, respectively, as shown in Figure 5.6b**.**

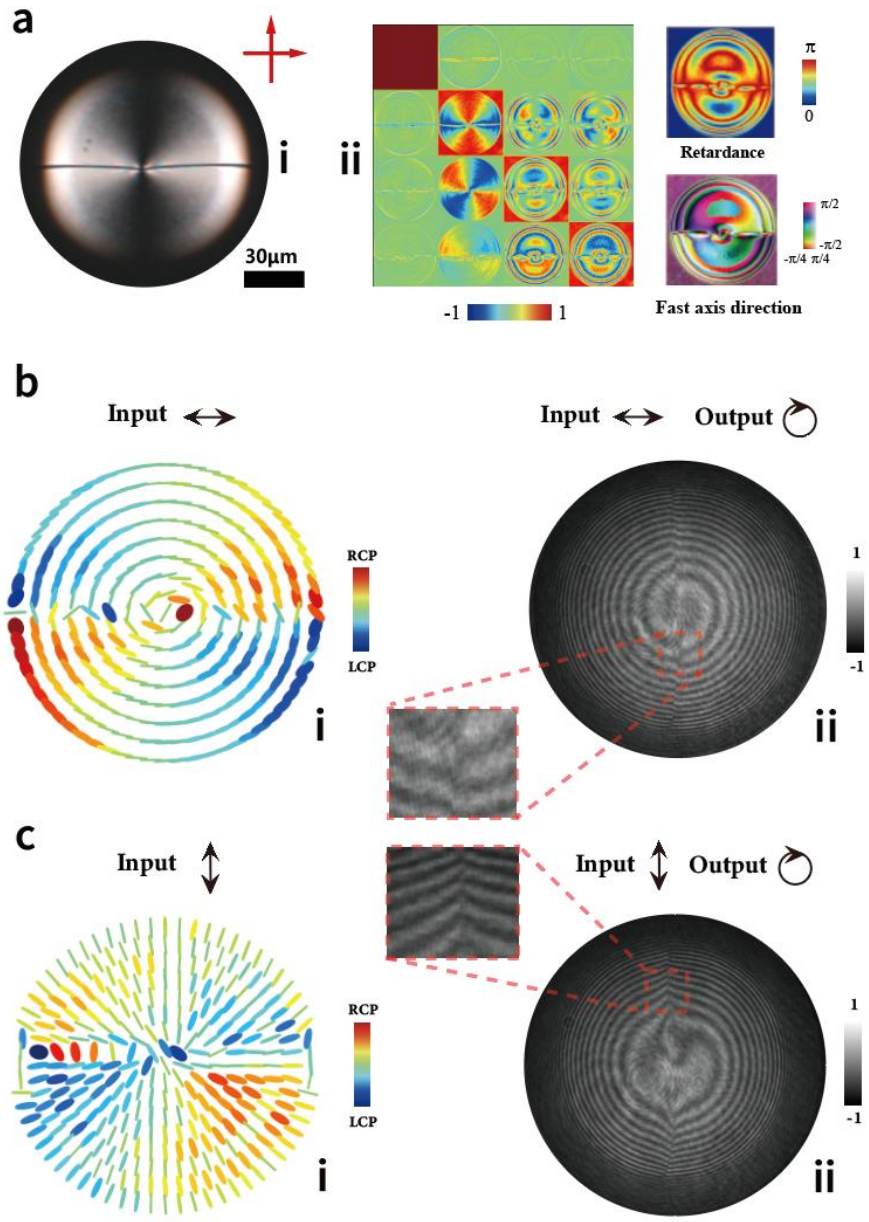


Figure 5.6 Experimental results demonstrate the modulation of light by a printed nematic LC droplet (E7) on a glass substrate coated with a planar alignment layer. a(i) POM image of the printed droplet. The single-headed red arrows represent the orientations of the polarizers. The characteristics of the droplets are as follows: diameter = 125 μm, height = 28 μm, and contact angle = 32.1°. a(ii) The MM components characterizing the droplet's full optical response. The decomposition of the MM provides the retardance and fast axis direction profiles, showing how the droplet alters the polarization. (b) The polarization patterns and the interference patterns when illuminated with horizontally polarized light. (c) The polarization patterns and the interference patterns when illuminated with vertically polarized light. Measurements were carried out at 23°C.

To further investigate the droplet's ability to modulate the phase of light, the interferometer introduced previously was used. In this configuration, the droplet was illuminated with either horizontally or vertically polarized light, and a circular polarizer in the PSA filtered the output before interference was recorded. The resulting interferograms, as shown in Figure 5.6c, exhibit ring patterns with discontinuities in the fringes. In one case, a nearly π-phase shift produces prominent fringe breaks, while in the other case the phase shift is minimal, and the fringes appear nearly continuous.

A possible explanation for the observed interference patterns is the influence of the alignment layer beneath the droplet. The planar alignment layer's rubbing direction, which is perpendicular to the declination line shown in Figure 5.6a(i), ensures uniform alignment of the LC director near the substrate. As light propagates through the droplet, its phase accumulates from local changes in refractive index that depend on the LC director orientation. On either side of the declination line, the director is mirror-symmetric but oppositely tilted, leading to different retardance values and a phase difference that produces discontinuous fringes.

When the incident light is polarized parallel to the rubbing direction, the light first encounters the extraordinary refractive index and then gradually the ordinary refractive index as the director reorients near the droplet's curved surface. Because the director tilt is mirror-symmetric but opposite on either side of the disclination line, the rate of this transition differs between the two regions. This results in a phase difference that is not smoothly varying across the disclination line, leading to discontinuities in the

interference fringes. In contrast, with incident light polarized perpendicular to the rubbing direction, the light experiences a uniform ordinary refractive index, yielding nearly equal optical path lengths and continuous interference fringes.

5.5.3 Printed long-pitch chiral nematic LC on a planar alignment layer

Printed long-pitch chiral nematic LC droplets (E7 + 4 wt.% R811, pitch = 2.5 μm) on a planar alignment layer can be used to generate optical singularities, which refer to specific points or regions in a light field where the orientation of the polarization ellipse is undefined (C-point) or where its handedness is indeterminate (L-line)[177-179]. These structured beams have practical applications in quantum communication and optical tweezers, and enable precise manipulation of microscopic particles, with further implications in fields such as optofluidic and biophotonics[180, 181].

The POM image, shown in **Figure 5.7**a(i), reveals a spiral pattern with multiple rings; the origins of this spiral pattern were discussed in more detail in Section 4.3.2. The polarization properties of these droplets were further examined using a MM polarimeter. As shown in Figure 5.7a(ii), the fast axis orientation map displays alternating black and white regions, which correspond to the alignment of circular SoP fast axis. In addition, the retardance map exhibits a series of concentric regions with significant retardance, indicating that the droplet introduces measurable phase delays to the transmitted circularly polarized light. These observations imply that the droplet

behaves as a localized circular retarder. It should be noted that the abrupt black-white transitions in the edge of the fast axis map are attributed to numerical discontinuities $(-90°, 90°)$.

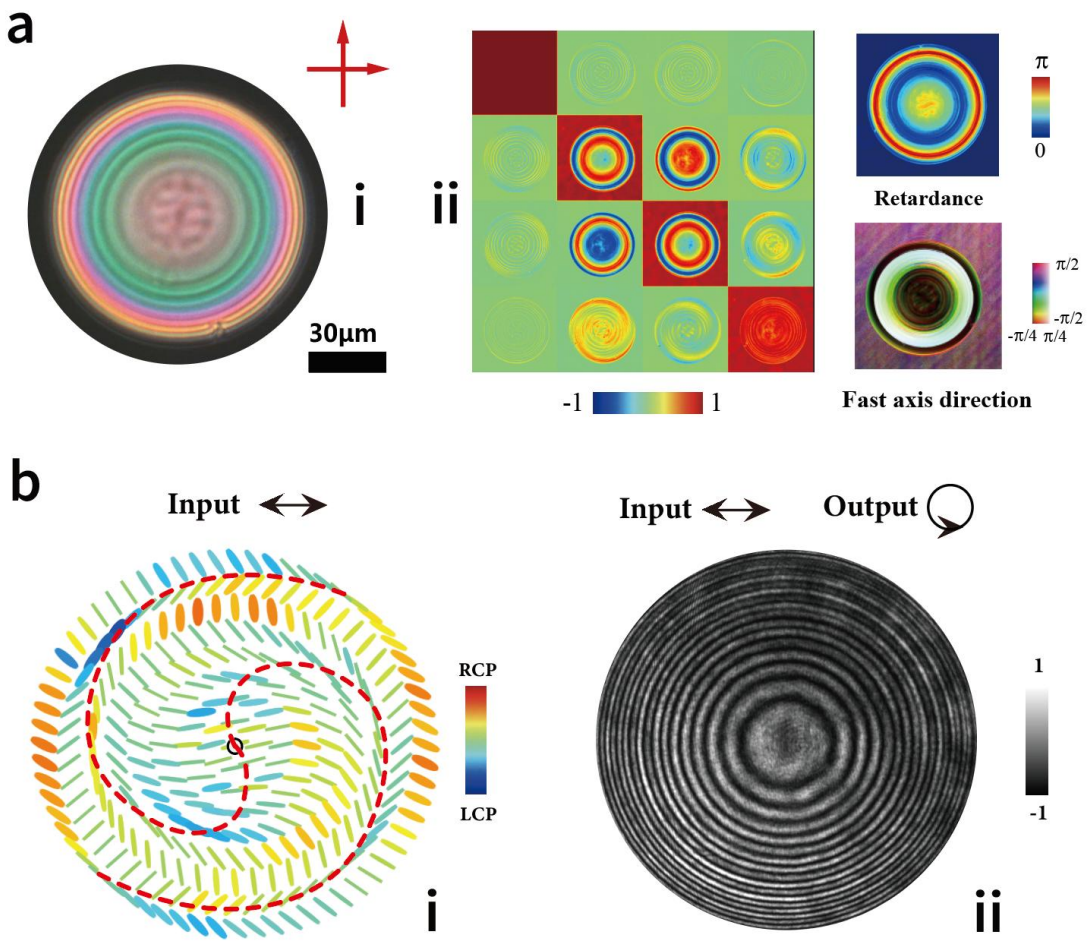


Figure 5.7 Experimental results demonstrating the modulation of light by a printed chiral nematic LC droplet (E7 + 4 wt.% R811) on a glass substrate coated with a planar alignment layer (lecithin). a(i) Polarizing optical microscopy image of the printed droplet. The geometric properties of the droplets are as follows: diameter = 122 μm, height = 28 μm, and contact angle = 32.2°. The single-headed red arrows represent the orientations of the polarizers. a(ii) The MM components characterizing the droplet's full optical response with the retardance and fast axis direction profiles. b(i) The polarization pattern highlights optical singularities, with the red dashed lines representing L lines in the pattern. b(ii) The interference pattern shows concentric rings, resulting from radial variations in phase retardation as light passes through the droplet. Measurements were taken at a temperature of 23℃.

Figure 5.7b(i) presents the polarization pattern obtained when the incident light is horizontally polarized. This pattern clearly reveals the presence of optical singularities. In particular, the red curves in the image delineate L-line spirals, which mark the regions where the polarization is linear but where the handedness cannot be defined. Following this, Figure 5.7b(ii) shows the interference pattern generated by the printed chiral nematic LC droplet. The interference pattern displays multiple concentric rings, which arise from aberrated phase shifts across the droplet — such as defocused or spherical-like phase variations.

These results collectively demonstrate the ability of the printed achiral and chiral nematic LC droplets to simultaneously modulate the phase and polarization of transmitted light. This dual modulation enables the generation of a wide variety of structured light fields, including full Poincaré beams with two units of OAM, radially or azimuthally polarized beams, and polarization singularities. The diversity and controllability of these beam profiles highlight the potential of printed LC droplets as compact, versatile elements for advanced beam shaping applications.

5.6 Summary

This work proposes an innovative method for generating complex structured light fields using inkjet-printed LC droplets. The approach utilizes nematic LC droplets on both homeotropic and planar alignment layers, as well as chiral nematic LC droplets on planar alignment layers, to exploit the intrinsic birefringence of LCs to expand the range

of achievable structured light. The method enables the generation of diverse structured light fields, including skyrmionic beams with two units of OAM, azimuthal and radial polarization beams, and beam exhibiting polarization singularities. Combined, these results demonstrate that by controlling the droplet alignment and composition, the phase and polarization of transmitted light can be precisely modulated. Compared to conventional methods, the use of LC droplets offers three distinct advantages. First, the inkjet-printing process is highly efficient and cost-effective, capable of producing nearly a hundred droplets per second, which enables large-scale array fabrication. Second, the small size of LC droplets makes them well-suited for miniaturized optical devices; their compact footprint allows integration into applications with limited space, such as photonic chips. Third, LC droplets provide a high degree of design flexibility, allowing for the precise tailoring of light fields without the need for complex optical setups. This versatility is particularly valuable in integrated photonics and optical sensing, where reducing system complexity and device footprint is critical.

In summary, this study demonstrates that printed LC droplets can serve as effective passive elements for generating structured light, and this approach lays a solid foundation for future studies into the design and control of structured light fields through LC droplet systems. The work inspires further developments across a range of disciplines, including integrated photonics, optical communication, quantum technologies, and biomedical imaging.

Chapter 6

Printed LC Droplet Arrays for Full Vectorial Optical Field Sensors

"Innovation is taking two things that exist and putting them together in a new way."

Tom Freston

6 Printed LC Droplet Arrays for Full Vectorial Optical Field Sensors

6.1 Introduction

The amplitude, phase, polarization, and wavelength of light are essential properties that determine how optical fields behave and interact with matter. Traditional optical techniques can measure these properties either separately or simultaneously using complex and bulky devices that are often challenging to fabricate[182-186]. An approach that is easier and faster to produce, with a simpler architecture and lower cost, would offer significant advantages for practical applications, meeting the rising demand for lightweight, low-power spectro-polarimetric modules in drone-borne remote sensing, handheld biomedical diagnostics, and in-line industrial laser monitoring[187-192].

In the realm of polarization measurements, Stokes polarimetry is widely used, typically through time-sequential modulation techniques involving rotating polarization elements[193], LC retarders[194], or photoelastic modulators[195]. For dynamic samples, simultaneous polarization detection is necessary to avoid errors introduced by temporal variations[196], and this can be achieved via multiple detectors or spatial and spectral modulation[197]. In addition, a variety of methods exist for phase measurement, such as the plenoptic wavefront sensors (WS)[198], confocal WS[199], curvature WS[200], image-based WS[201], and deep learning WS[186]. However, these techniques typically require costly optical elements and strict alignment conditions. In

contrast, Shack-Hartmann wavefront sensors (SHWS) offer a mature and stable alternative. SHWS map phase distortions across a wavefront by analysing the displacement of focal spots from a lens array, enabling real-time measurement of phase and amplitude profiles using standard imaging systems[202].

Unlike traditional polarization or phase measurement methods that typically require separate optical configurations or sequential measurements, this work proposes a proof-of-concept full optical vectorial field sensor based on an array of nematic LC (E7) droplets printed on a glass substrate with a homeotropic alignment layer. This approach leverages the unique optical properties of LC droplets (as discussed in the previous chapters) to simultaneously measure phase and polarization. Because each LC droplet behaves as a tiny lens, the entire droplet array can serve as a SHWS: each droplet focuses light from its local region onto the detector, and the shifts of these focal spots directly map the curvature of the local wavefront, allowing reconstruction of the phase profile.

Simultaneously, the radially varying birefringence of the LC droplets serves as an independent polarization sensing channel, enabling single-shot retrieval of the incident beam's SoPs without the need for sequential modulation. Furthermore, integration with an RGB camera allows for the separation of multiple wavelengths in a single measurement, facilitating the independent extraction of phase and polarization data for each wavelength. Moreover, by using an RGB camera to record intensity in three separate spectral bands (red, green, and blue), the system can infer wavelength-

dependent information alongside amplitude, phase, and polarization in a single, real-time acquisition. Some of the results and findings from this chapter have been submitted for publication.

6.2 LC droplet Arrays for Stokes Polarimetry

6.2.1 Introduction to division-of-wavefront polarimetry (DoWP)

A Stokes polarimeter is one that is designed to determine the SoP of light, which is fully described by a Stokes vector comprising four components: S_0, S_1, S_2, and S_3. These components together provide a complete description of the light's polarization characteristics, as previously discussed in Chapter 5. To determine these four components, at least four independent measurements are required — typically obtained by analysing the light after it passes through different polarization filters.

There are two primary approaches to Stokes polarimetry: a time-sequential method and a simultaneous/synchronous method[203-205]. In the time-sequential approach, the polarization information is captured sequentially by passing the light through a series of polarization elements, such as linear polarizers and wave plates, each configured to isolate one of the Stokes parameters[206, 207]. Although this method is straightforward, it requires multiple measurements over time and is less suitable for dynamic light fields. In contrast, the simultaneous method captures all four Stokes parameters in one instance by employing multiple detector arrays simultaneously or by dividing the incident light's wavefront into sub-wavefronts, each directed through different polarization

measurement channels[197]. One prominent technique within this category is the DoWP approach, which allows for the concurrent acquisition of the necessary intensity data.

6.2.2 Measurement principles

In the system presented in this chapter, printed LC droplets are utilized to measure the SoP of light using the DoWP method. The LC droplets serve as polarization-sensitive elements, enabling the simultaneous analysis of the light's SoP. By employing a MM polarimeter, the patterns of retardance (the phase difference between the ordinary and extraordinary rays) and the orientation of the fast axis (the axis along which the light experiences the least phase delay) within a nematic LC droplet (E7) are characterized as shown in **Figure 6.1**.

The retardance pattern of the LC droplets reveals concentric circles, where the retardance increases from the centre outward and then resets. The fast axis orientation shows radial symmetry, indicating that each position of the droplet modulates the SoP of the incident light differently. For example, when uniform polarized light illuminates the droplet, each segment of the emitted light experiences distinct modulation effects based on its position relative to the droplet’s centre. This behaviour allows each point on a droplet to function as multiple parallel analysis channels for polarisation sensing. Thus, a single LC droplet effectively operates as a DoWP, enabling the simultaneous capture of all Stokes parameters across the wavefront.

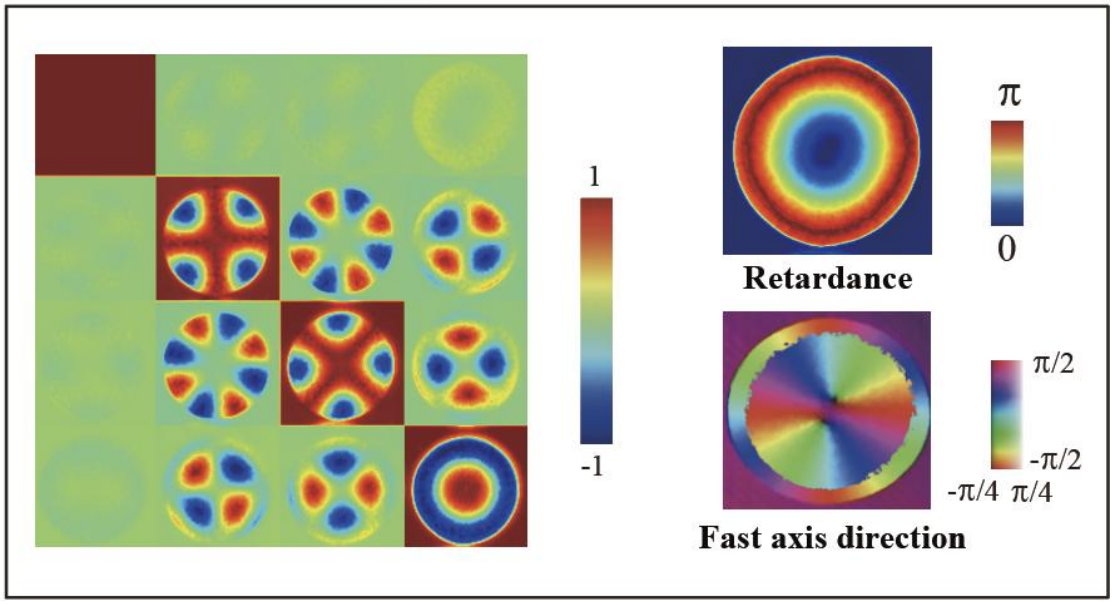


Figure 6.1 The MM characterizes the full optical response of the nematic LC (E7) droplets printed on the substrate with homeotropic alignment layer (diameter = 253 μm). The MM decomposition reveals the effective linear retardance and fast axis direction of the droplet. The retardance profile shows concentric rings, while the fast axis direction exhibits a radial symmetry, both indicating a vertical alignment with a gentle tendency for the LC director to align radially within the droplet. The fast axis was characterized using the Hue-Saturation-Luminance model: hue represents the elliptical axis orientation; luminance indicates the degree of ellipticity. The retardance distribution is represented using the colour bar, with values ranging from 0 to π.

A limitation of the LC droplet based DoWP is that it can only measure the SoP at a single spatial location, yielding a single SoP result. To overcome this limitation, an array of LC droplets is utilized, where each droplet independently measures the SoP within its respective area. This approach enables the LC droplet array polarimeter to capture the SoP of light beams that vary across both space and time. Based on this concept, a LC droplet array polarimeter is developed. In **Figure 6.2**(a), the system begins with a laser light source that passes through a SoP modulation block, which produces various controlled SoPs. The beam then enters the LC droplet array polarimeter. This

polarimeter consists of a LC droplet array placed in front of a fixed polarizer, followed by a CCD camera that records the resulting intensity distribution. Each droplet within the array acts as a local waveplate with its own birefringence characteristics, imprinting spatially varying polarization information on the beam. The polarizer then filters these polarization components, and the camera detects the corresponding intensity pattern. By analysing this pattern, the system can retrieve the full Stokes vector of the incident light in a single measurement.

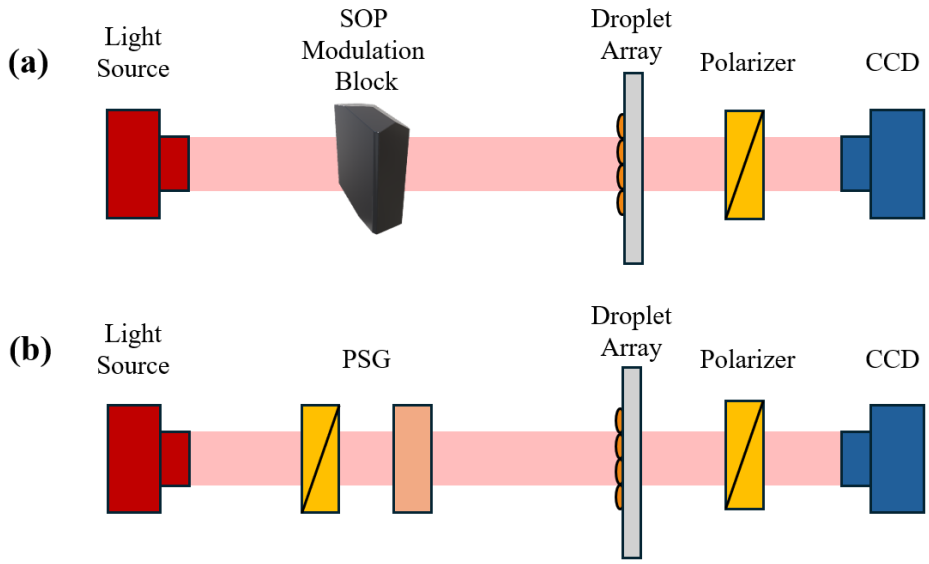


Figure 6.2 Schematic diagram of the measurement and calibration configurations for the LC droplet array based polarimeter. (a) Measurement configuration for the LC droplet array polarimeter. A SoP modulation block generates controlled SoPs, which pass through the droplet array and a polarizer before being recorded by a CCD camera. (b) Calibration process, where a PSG is used alongside the droplet array and polarizer to measure known input Stokes vectors and determine the system matrix.

The Stokes vector of the incident light is defined as $\vec{S}_{in} = \left(S_{0,in}, S_{1,in}, S_{2,in}, S_{3,in}\right)^T$. This enters the LC droplet array polarimeter, which comprises an array of LC droplets followed by a polarizer and a CCD camera. The polarimeter's

output light can be described by $\vec{S}_{out} = \left(S_{0,out}, S_{1,out}, S_{2,out}, S_{3,out}\right)^T$. The relationship between the incident and output Stokes vectors can be expressed as:

$$\vec{S}_{out} = M_P \cdot M_{LC} \cdot \vec{S}_{in}. \tag{6.1}$$

Here, M_P and M_{LC} represent the MM of the LC droplet array and the polarizer, respectively.

Since the CCD camera can only capture the intensity information of the light, corresponding to the first element of $\vec{S}_{out}$ *($\vec{S}_{0,out}$)*, so only the first row of the Mueller matrices M_P is relevant. The first row of the Mueller matrices for a linear polarizer can be expressed as:

$$M_P(1,:) = (p_t, \quad p_t, \quad 0, \quad 0). \tag{6.2}$$

As mentioned earlier, each point on a LC droplet can be approximated as a small waveplate with a fast axis θ_n and a retardance δ_n which vary over the droplet area. The MM of each waveplate $M_{n,LC}$ can be written as:

$$M_{n,LC} \approx \begin{bmatrix} 1, & 0, & 0, & 0 \\ 0, & cos^2 2\theta_n + sin^2 2\theta_n cos\delta_n, & 0.5sin4\theta_n(1-cos\delta_n), & -sin2\theta_n sin\delta_n \\ 0, & 0.5sin4\theta_n(1-cos\delta_n), & sin^2 2\theta_n + cos^2 2\theta_n cos\delta_n, & cos2\theta_n sin\delta_n \\ 0, & sin2\theta_n sin\delta_n, & -cos2\theta_n sin\delta_n, & cos\delta_n \end{bmatrix} \tag{6.3}$$

In the real experiment, the CCD camera simultaneously captures the intensity values corresponding to the output of each tiny waveplate, denoted as $\vec{S}_{0n,out}$. By substituting Eq. (6.2) and Eq. (6.3) into Eq. (6.1), we derive:

$$\vec{S}_{0n,out} =$$

$$(p_t, \quad p_t(cos^2 2\theta_n + sin^2 2\theta_n cos\delta_n), \quad 0.5p_t sin4\theta_n(1 - cos\delta_n), \quad -p_t sin2\theta_n sin\delta_n) \cdot \begin{pmatrix} S_{0,in} \\ S_{1,in} \\ S_{2,in} \\ S_{3,in} \end{pmatrix}. \tag{6.4}$$

Finally, by combining the results from the n measurements, the intensity can be expressed by:

$$I =$$

$$\begin{pmatrix} p_t, & p_t(cos^2 2\theta_1 + sin^2 2\theta_1 cos\delta_1), & 0.5p_t sin4\theta_1(1 - cos\delta_1), & -p_t sin2\theta_1 sin\delta_1 \\ \vdots & \vdots & \vdots & \vdots \\ p_t, & p_t(cos^2 2\theta_n + sin^2 2\theta_n cos\delta_n), & 0.5p_t sin4\theta_n(1 - cos\delta_n), & -p_t sin2\theta_n sin\delta_n \end{pmatrix} \cdot \begin{pmatrix} S_{0,in} \\ S_{1,in} \\ S_{2,in} \\ S_{3,in} \end{pmatrix}, \tag{6.5}$$

where I is an $n \times 1$ array of intensity measurements, with each entry corresponding to the light intensity recorded by the CCD at a specific droplet in the array. Here, n corresponds to the number of discrete intensity samples recorded by the CCD across the imaged area of a single LC droplet. The combined matrix in Eq. (6.5) can be expressed as A, an $n \times 4$ matrix. This matrix A represents the system MM of the entire LC droplet array polarimeter. In other words, as long as the LC droplet array and the polarizer remain unchanged, the system matrix A will remain constant. Consequently, the relationship can be expressed as:

$$\vec{I} = A \cdot \vec{S}_{in}. \tag{6.6}$$

The objective is to determine the incident Stokes vector $\vec{S}_{in}$. While the intensity vector $\vec{I}$ is directly obtained from the CCD camera, solving for $\vec{S}_{in}$ requires an accurate calibration of the system matrix A, which is independent of the incident light and remains fixed for a given system arrangement. It can be calibrated using the principles of MM polarimetry. To determine the system matrix M for the LC droplet array polarimeter, we use the relationship derived in Eq. (6.6), which can be expressed as

$$A = \vec{I} \cdot \vec{S}_{in}{}^{\dagger}, \tag{6.7}$$

where $\vec{S}_{in}{}^{\dagger}$ represents the pseudoinverse of $\vec{S}_{in}$.

To perform calibration, a set of at least four linearly independent SoPs is required; however, to increase accuracy and minimize measurement errors, 72 different SoPs are generated using a PSG. Specifically, the first 32 SoPs are produced by fixing the polarizer at $0°$ and rotating the QWP from $0°$ to $180°$ in $5°$ increments. Then, by removing the QWP and rotating the polarizer from $0°$ to $180°$ in $5°$ increments, an additional 32 states are obtained. For each of these 72 states, the CCD camera records the corresponding intensity values at n discrete points, forming an $n \times 72$ matrix $\vec{I}$. At the same time, the known input Stokes vectors for these states are compiled into a 4×72 matrix $\vec{S}_{in}$.

The calibration process is illustrated in Figure 6.2(b), which follows the conventional procedure used in MM polarimetry. By substituting these matrices into

Eq. (6.7), the system matrix A (of size $4 \times n$) is computed. This matrix A remains constant as long as the configuration of the LC droplet array and the polarizer do not change. The calibration procedure eliminates the need for a separate SoP analyser to measure the output Stokes vector, enabling a simple, single-shot measurement of the incident SoP. Once the system matrix A is calibrated, any unknown incident Stokes vector can be retrieved from a new intensity measurement $\vec{I}$ using

$$S_{in} = A^{\dagger} \cdot \vec{I}, \tag{6.8}$$

where $A^{\dagger}$ denotes the pseudoinverse of A.

6.2.3 Conventional Stokes polarimetry

To verify the accuracy of the LC droplet array-based sensing system, a well-established Stokes polarimetry method is required to measure the same incident beam's Stokes vector. A commonly used Stokes polarimetry technique employs a QWP followed by a polarizer, as illustrated in the **Figure 6.3**. A beam with an unknown SoP is directed into this PSA, where the QWP in practice should at least measure four independent intensity values to reconstruct any arbitrary incident SoP[141]. Typically, the QWP is rotated to four specific angles — chosen for optimal measurement accuracy (for example, $15.12°$, $51.69°$, $128.31°$, and $164.88°$)[183]. At each QWP angle, the output intensity is recorded by a CCD camera, providing four independent intensity measurements. These measurements are described by

$$\vec{S}_{out}^{(n)} = M_P \cdot M_{QWP}^{(n)} \cdot \vec{S}_{in},\ n = 1, 2, 3, 4 \tag{6.9}$$

$$\vec{I} = A \cdot \vec{S}_{in}, \quad S_{in} = A^{\dagger} \cdot \vec{I} \tag{6.10}$$

where $\vec{S}_{in}$ is the Stokes vector of the incident light field, M_P and $M_{QWP}^{(n)}$ are Mueller matrices of the corresponding polarizer and waveplate. $\vec{S}_{out}^{(n)}$ is the corresponding output Stokes vector for the n^{th} fast axis orientation state of the QWP. A is a $n \times 4$ matrix known as the instrument matrix, which is derived from $M_P \cdot M_{QWP}^{(n)}$. $\vec{I}$ is the intensity information recorded by the camera.

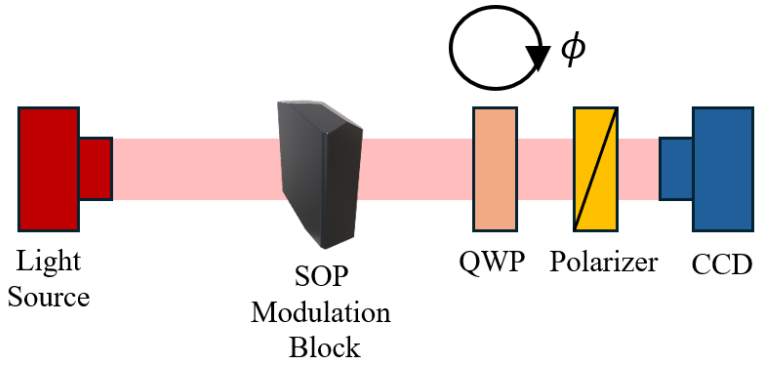


Figure 6.3 Schematic of a conventional Stokes polarimeter. A monochromatic light source passes through a SOP modulation block, then traverses a QWP and a polarizer. The CCD camera records intensities at different QWP angles, enabling reconstruction of the incident Stokes vector.

6.3 An LC droplet Array Shack-Hartmann Wavefront Sensor

6.3.1 Wavefront reconstruction method

A SHWS is an optical device designed to sample and reconstruct the phase profile of a distorted wavefront[208, 209]. The basic principle is that the overall wavefront can be divided into many small regions within the pupil plane, where each region's wavefront is approximated by a locally tilted plane wave relative to an ideal flat wavefront. By measuring the local tilt in every sub-aperture, the entire wavefront can be sampled and

reconstructed. The concept of using local tilt as a phase indicator was first introduced in the Hartmann test, where a mask with multiple small holes was placed behind an optical element. Each hole acted as a mini aperture, producing a spot whose position corresponded to the local wavefront tilt[210]. Later, Shack replaced the holes with an array of small lenses, which improved the accuracy and efficiency of the measurement. This innovation led to the modern SHWS, which remains widely used for characterizing phase distortions in optical systems[202]. Once the focal-spot pattern is recorded, however, a further computational step is still needed.

To reconstruct the complete wavefront, Zernike polynomials are utilized because they are particularly well-suited for representing wavefront distortions in optical systems, especially when dealing with circular apertures, such as the ones defined by the LC droplets in this configuration. Zernike polynomials can effectively capture various types of optical aberrations (e.g. defocus, astigmatism, and coma) with a compact set of mathematical functions. Each polynomial corresponds to a different type of wavefront deformation, making them highly efficient for describing the complex variations in phase caused by aberrations. The wavefront $\Phi(\rho, \theta)$ is expressed as:

$$\Phi(\rho, \theta) = \sum_{i=2}^{N} a_i Z_i(\rho, \theta), \tag{6.11}$$

where a_i is the coefficients of the i^{th} Zernike polynomial that represents its root-mean-square (RMS) phase value and $Z_i(\rho, \theta)$ are the corresponding Zernike polynomials. The summation starts from $i = 2$ because the first Zernike mode ($i = 1$)

corresponds to the piston term, which represents a constant phase offset across the wavefront. This term is not experimentally observable and does not affect the optical performance; therefore, it is excluded from the wavefront reconstruction. (For clarity, the definitions and ordering of the Zernike polynomials used throughout this thesis are provided in Appendix.) The coefficients a_n can be obtained using the orthogonality of Zernike polynomials,

$$a_i = \frac{1}{\pi}\int_0^1 \int_0^{2\pi} \Phi(\rho,\theta) Z_i(\rho,\theta) d\rho d\theta \,. \tag{6.12}$$

In this study, the LC droplet array is employed as a SHWS to reconstruct the wavefront and measure the phase information of the optical beam. As shown in Chapter 4, a nematic droplet on a homeotropic alignment layer develops a radial gradient-index profile, which can focus incoming light into spots just like a micro-lens. The LC droplets function similar to a traditional lenslet array by dividing the incoming wavefront into multiple sub-apertures. Within each sub-aperture, the local wavefront can be approximated by a tilted plane wave. The light passing through each droplet is then focused onto a detector, forming a pattern of focal spots, referred to as Shack-Hartmann spots. For an ideal, aberration-free wavefront, these spots would form a regular grid. However, wavefront aberrations cause displacements of these spots from their reference positions, which we use to determine the local slopes of the wavefront at each sub-aperture (**Figure 6.4**(a)).

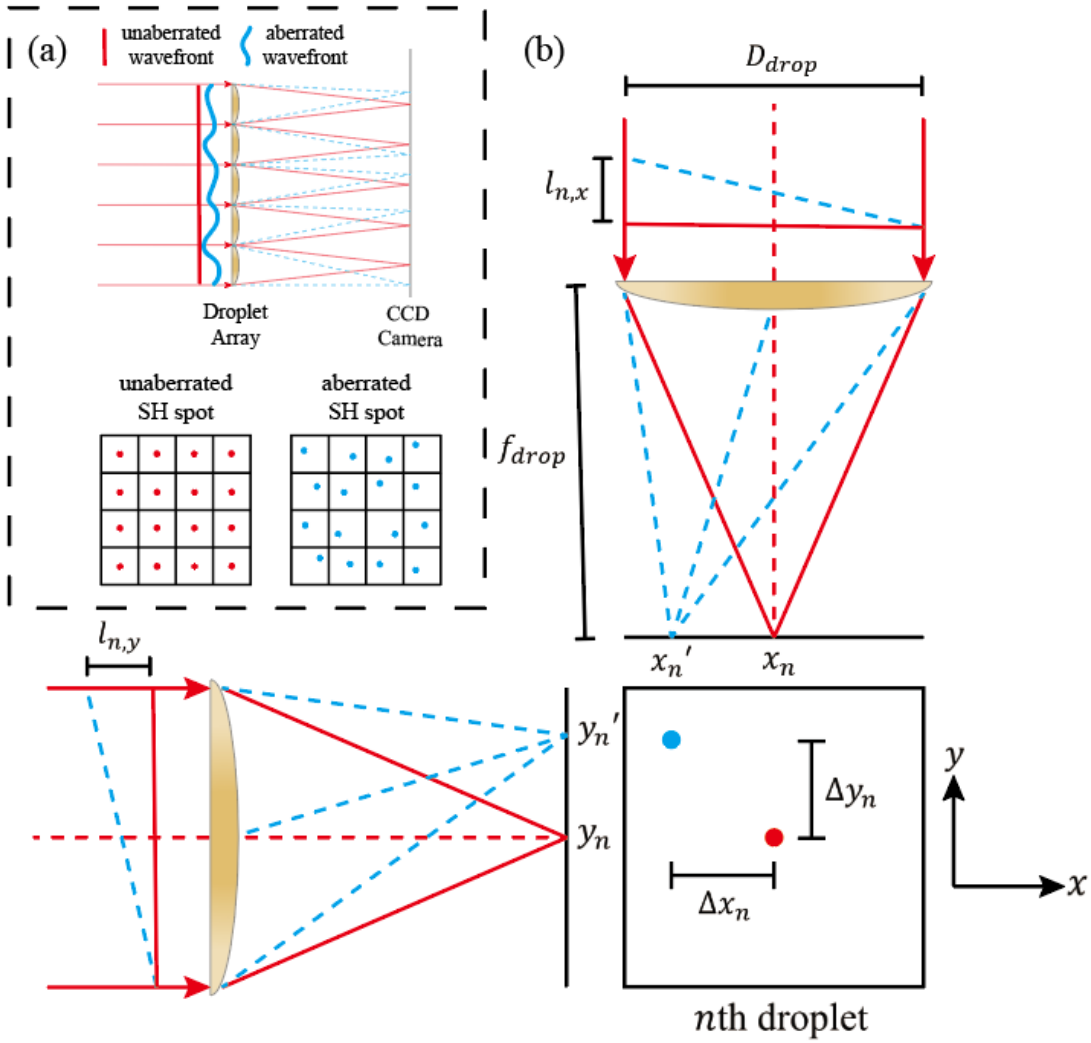


Figure 6.4 This diagram presents an overview of the SHWS configuration along with the corresponding spot pattern. (a) The sensor geometry: a collimated beam is divided by an array of droplets, with each droplet sampling a small sub-aperture. The local tilt of the wavefront in each sub-aperture causes a displacement of the focal spot along the *x* and *y*-axes. (b) Single spot displacement: an ideal wavefront produces a uniform array of spots, whereas an aberrated wavefront results in shifted spots that reveal the local wavefront tilt.

The precise position of each Shack-Hartmann spot is calculated using a centroiding algorithm that computes the centroid of the intensity distribution at each focal spot. The centroid coordinates (x_c, y_c) are determined by:

$$x_c = \frac{\sum_{m=1}^{N} x_m I_m}{\sum_{m=1}^{N} I_m}, \quad y_c = \frac{\sum_{m=1}^{N} y_m I_m}{\sum_{m=1}^{N} I_m} \tag{6.13}$$

where x_m and y_m are the coordinates of the m^{th} pixel, and I_m is the intensity at that pixel. By comparing the centroid positions with the expected positions for an unaberrated wavefront, the displacements Δx and Δy are calculated (Figure 6.4(b)). These displacements are directly proportional to the local wavefront slopes:

$$\frac{\partial(\Phi_n)}{\partial x} \simeq \frac{l_{n,x}}{D_{drop}} = \frac{\Delta x_n}{f_{drop}}, \quad \frac{\partial(\Phi_n)}{\partial y} \simeq \frac{l_{n,y}}{D_{drop}} = \frac{\Delta y_n}{f_{drop}} \tag{6.14}$$

where f_{drop} represents the focal length equivalent of the LC droplets, while D_{drop} is the diameter of each droplet. $l_{n,x}$ and $l_{n,y}$ the axial displacement of the wavefront tilt across the lenslet aperture in the *x*- and *y*-direction, respectively. These slopes provide the local wavefront tilt at each sub-aperture, capturing the phase variations across the wavefront.

Since the CCD camera records the intensity on a rectangular grid, the phase aberration Φ is also represented in Cartesian coordinates by rewriting Eq. (6.11) as

$$\Phi(x, y) = \sum_{n=2}^{N} a_n Z_n(x, y)\,, \tag{6.15}$$

with $\rho = \sqrt{x^2 + y^2}$ and $\theta = \tan\frac{y}{x}$. Assuming that (x_n, y_n) are now normalised coordinates of the n^{th} droplet on a unit circle, the local wavefront tilt at that droplet can be expressed as

$$\frac{\partial\big(\Phi_n(x_n, y_n)\big)}{\partial x} = \frac{\Delta x_n}{f_{drop}} = \sum_{i=2}^{N} a_i \frac{\overline{\partial Z_\iota(x_n, y_n)}}{\partial x}, \tag{6.16}$$

$$\frac{\partial\left(\Phi_n(x_n, y_n)\right)}{\partial y} = \frac{\Delta y_n}{f_{drop}} = \sum_{i=2}^{N} a_i \frac{\overline{\partial Z_i(x_n, y_n)}}{\partial y} \tag{6.17}$$

where $\frac{\overline{\partial Z_i(x_n,y_n)}}{\partial x}$ and $\frac{\overline{\partial Z_i(x_n,y_n)}}{\partial y}$ are the averaged x and y derivatives of the i^{th} Zernike polynomial. Here, the averaged derivatives represent the area-averaged first-order spatial derivatives of the Zernike polynomials over the effective aperture of each LC droplet. This averaging accounts for the finite size of the droplet, which samples the local wavefront slope over its entire aperture rather than at a single point, analogous to conventional Shack–Hartmann wavefront sensing. Collecting the local slopes from all droplets into a single vector $\vec{D}$ yields

$$\vec{D} = \nabla Z \vec{a}, \tag{6.18}$$

with

$$\vec{D} = \begin{bmatrix} \Delta x_1/f_{drop} \\ \Delta x_2/f_{drop} \\ \vdots \\ \Delta x_n/f_{drop} \\ \Delta y_1/f_{drop} \\ \Delta y_2/f_{drop} \\ \vdots \\ \Delta y_n/f_{drop} \end{bmatrix}, \ \vec{a} = \begin{bmatrix} a_1 \\ a_2 \\ \vdots \\ a_n \end{bmatrix} \tag{6.19}$$

and

$$\nabla Z = \begin{bmatrix} \overline{\frac{\partial Z_1(x_1,y_1)}{\partial x}} & \overline{\frac{\partial Z_2(x_1,y_1)}{\partial x}} & \cdots & \overline{\frac{\partial Z_n(x_1,y_1)}{\partial x}} \\ \overline{\frac{\partial Z_1(x_2,y_2)}{\partial x}} & \overline{\frac{\partial Z_2(x_2,y_2)}{\partial x}} & \cdots & \overline{\frac{\partial Z_n(x_2,y_2)}{\partial x}} \\ \vdots & \vdots & \ddots & \vdots \\ \overline{\frac{\partial Z_1(x_n,y_n)}{\partial x}} & \overline{\frac{\partial Z_2(x_n,y_n)}{\partial x}} & \cdots & \overline{\frac{\partial Z_n(x_n,y_n)}{\partial x}} \\ \overline{\frac{\partial Z_1(x_1,y_1)}{\partial y}} & \overline{\frac{\partial Z_2(x_1,y_1)}{\partial y}} & \cdots & \overline{\frac{\partial Z_n(x_1,y_1)}{\partial y}} \\ \overline{\frac{\partial Z_1(x_2,y_2)}{\partial y}} & \overline{\frac{\partial Z_2(x_2,y_2)}{\partial y}} & \cdots & \overline{\frac{\partial Z_n(x_2,y_2)}{\partial y}} \\ \vdots & \vdots & \ddots & \vdots \\ \overline{\frac{\partial Z_1(x_n,y_n)}{\partial y}} & \overline{\frac{\partial Z_2(x_n,y_n)}{\partial y}} & \cdots & \overline{\frac{\partial Z_n(x_n,y_n)}{\partial y}} \end{bmatrix} \tag{6.20}$$

Finally, the Zernike coefficients are obtained via the pseudoinverse of ∇Z:

$$\vec{a} = (\nabla Z)^{\dagger}\vec{D}. \tag{6.21}$$

This complete process yields the Zernike coefficients that fully describe the wavefront aberrations, thereby allowing a comprehensive reconstruction of the phase profile across the LC droplet array.

6.3.2 Focal length of the LC droplet

Measuring the focal length of the LC droplets is necessary for accurate phase reconstruction using the Shack-Hartmann method, as the local wavefront slope is calculated from the focal spot displacement divided by the droplet's focal length. To measure the effective focal length of the LC droplets f_{drop}, A collimated laser beam was directed through an LC droplet, and the transmitted light was then focused by a 4*f* system positioned immediately behind the droplet. This 4*f* system ensured that the droplet's image was accurately relayed to its focal plane. The light exiting the 4*f* system

was then captured by a CCD camera, which was mounted on a movable two-axis translation stage allowing precise movement along the optical z-axis (**Figure 6.5**).

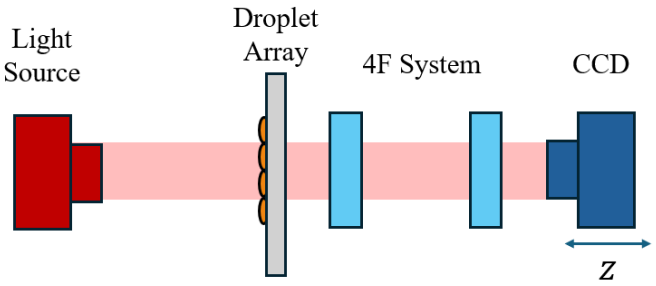


Figure 6.5 A schematic diagram of the optical arrangement for measuring the effective focal length of an LC droplet in an array. A collimated laser beam passed through the droplet array and a 4*f* system. The CCD was mounted on a translation stage and moved along the optical axis to locate the position Z where the focused spot from each droplet reached its minimum size, corresponding to the focal plane.

By translating the CCD along the beam path, a series of images were recorded at different z positions. The effective focal length of the droplets was determined by observing the transition in the droplet's image: initially, the image displays clear boundaries and a complete representation of the droplet, and then, at a specific z position, the image was focused into a minimal bright spot (focal spot). The distance between these two imaging conditions was taken as the effective focal length of the LC droplet.

6.3.3 Spatial light modulator calibration

To evaluate the performance of the LC droplet array as a phase sensor, it is essential to illuminate it with optical beams carrying well-defined and controllable wavefront distortions. This was achieved using a spatial light modulator (SLM), which allows us to impose controlled phase patterns — such as individual Zernike modes — onto the

incident beam. However, the SLM (Hamamatsu LCOS-SLM X15213-01) control software defines phase modulation using a unitless "Amplitude" parameter, which does not directly correspond to a physical OPD. To interpret the phase measurement results in meaningful physical units, it is therefore necessary to calibrate the SLM and establish a direct, quantitative relationship between the input amplitude and the actual root-mean-square optical path difference (RMS OPD) imparted on the wavefront. This calibration was performed using an external reference: a commercial SHWS (Edmund Optics 64-478), which provided traceable measurements of the applied phase.

The experimental layout follows a conventional configuration for phase calibration (**Figure 6.6**). After reflecting from the SLM, the collimated beam then entered the SHWS equipped with a lenslet array of 300 μm pitch and 18 mm focal length. This array samples the wavefront and generates a corresponding grid of focal spots. To accurately relay this focal plane onto the camera, a 4*f* imaging system was placed directly after the lenslet array.

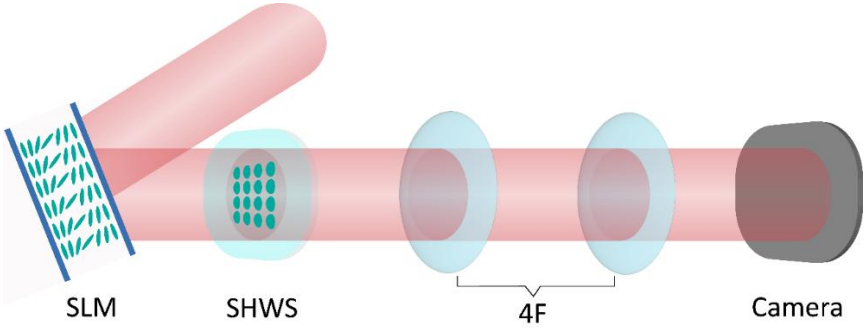


Figure 6.6 Schematic of the experimental setup for calibrating the SLM using a SHWS. A collimated beam is phase-modulated by the SLM and then directed into the SHWS, where a lenslet array (300 μm pitch, 18 mm focal length) samples the wavefront and forms a grid of focal spots. A 4*f* imaging system relays the focal plane onto a CCD camera for accurate measurement of spot displacements and wavefront reconstruction.

Calibration begins by applying a flat phase (software amplitude $= 0$) to the SLM, allowing the SHWS to record a baseline wavefront and confirm system alignment. Next, for each Zernike mode of interest, a series of five software amplitudes — 2, 5, 10, 15, and 20 — was loaded onto the SLM. For each setting, the SHWS measures the resulting wavefront and extracts the RMS OPD using its built-in reconstruction algorithm. The five RMS OPD values corresponding to each mode were then fitted using least-squares linear regression to obtain a mode-specific calibration slope k_n, which converted SLM software amplitude into physical RMS OPD (in μm). As shown in **Figure 6.7**, all tested modes exhibited a linear dependence between the applied aberration amplitude and the measured response, with horizontal and vertical tilt modes yielding slopes near $0.033\ \mu\text{m/unit}$, while defocus and astigmatism modes showed slightly different sensitivities. These variations arise from the distinct spatial energy distributions associated with each Zernike mode. The resulting calibration coefficients k_n were stored and applied during wavefront sensing experiments, ensuring that every phase pattern commanded on the SLM corresponded to a well-defined and reproducible physical aberration.

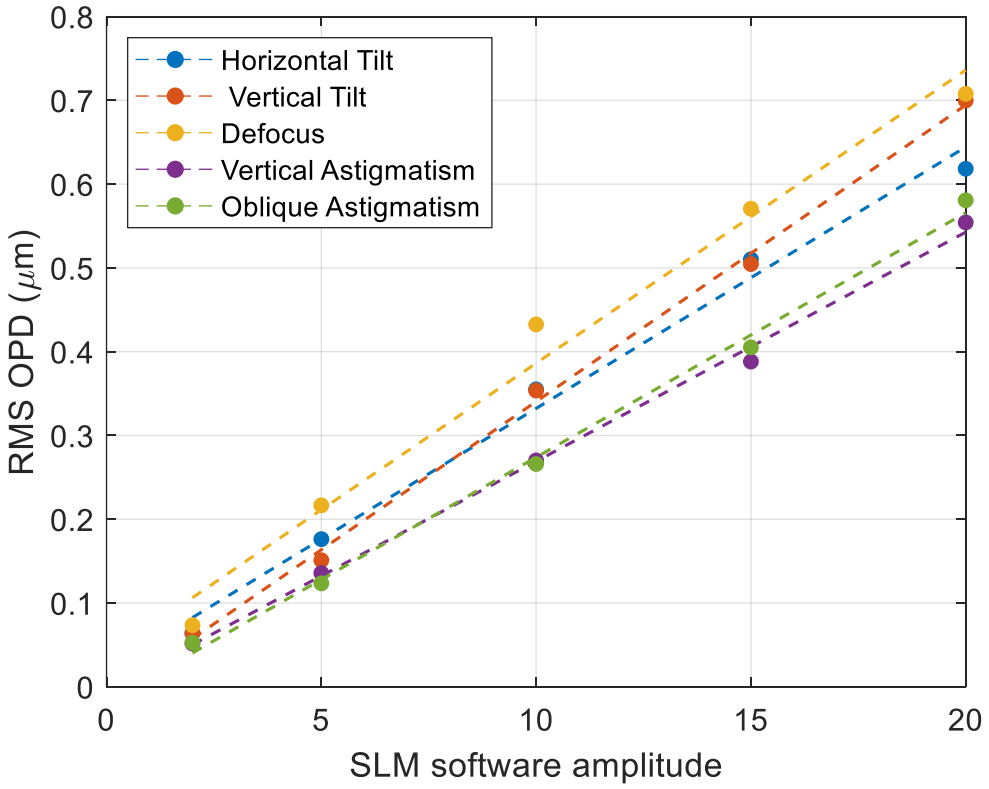


Figure 6.7 SLM calibration curves for five Zernike modes using a commercial SHWS. Each plot shows the measured RMS OPD as a function of the SLM software amplitude for a specific Zernike mode: horizontal tilt, vertical tilt, defocus, vertical astigmatism, and oblique astigmatism. Data points represent SHWS measurements, and dashed lines indicate least-squares linear fits. The extracted slopes provide mode-specific calibration coefficients that convert software input values into physically meaningful RMS OPD in μm.

6.4 Fabrication of the LC Droplet Array

The LC droplet array was fabricated using an inkjet printing method selected for its simplicity, efficiency, and precise control over droplet placement, as described in detail in previous chapters. The process began by spin-coating acetone-cleaned glass slides with a 0.02% lecithin solution in IPA at 1200 revolutions per second. The substrate was then baked at 70℃ for 30 seconds to form a homeotropic alignment layer, which ensured that LC director aligned perpendicularly to the substrate (**Figure 6.8**(a)(e)).

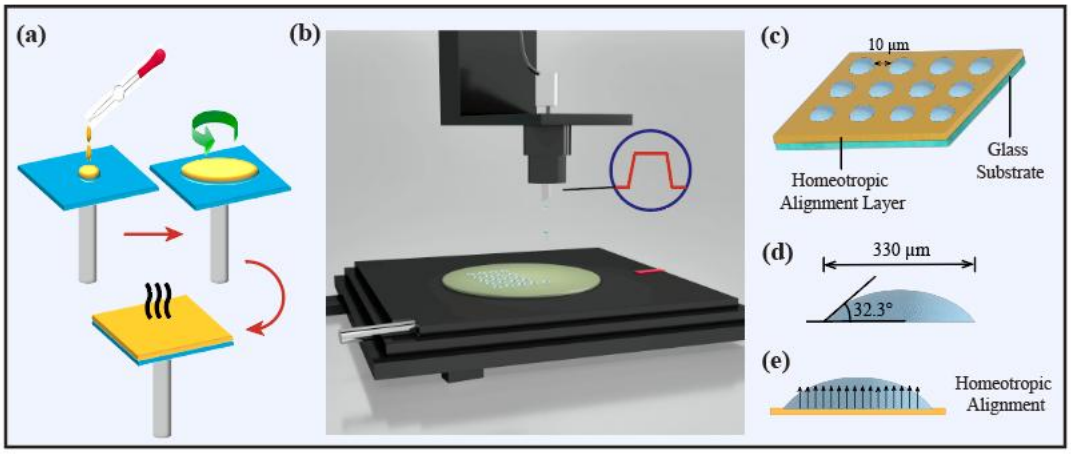


Figure 6.8 Schematic illustration of the fabrication process for the inkjet-printed LC droplet array on a homeotropic alignment substrate. (a) Substrate preparation, illustrating the spin coating and baking steps for forming a homeotropic alignment layer. (b) Inkjet printing process used to deposit the LC droplet array onto the prepared substrate. (c) Schematic diagram showing the arrangement of printed droplets, each droplet with a uniform spacing of $10\ \mu m$. (d) Side view of a single droplet, with a final diameter of approximately $330\ \mu m$, focal length of $0.55mm$ and contact angle of $32.3°$. (e) Depiction of the homeotropic alignment layer's influence on the LC director orientation within each droplet.

Inkjet printing was performed using the MicroFab Jetlab II system, equipped with an $80\ \mu m$ nozzle. The printhead operated at $70℃$, a temperature intentionally set above the isotropic transition temperature of the LC material E7 ($58℃$). This elevated temperature mitigates viscosity anisotropy, thereby enhancing the uniformity and stability of the printed droplets. LC droplets were deposited onto the prepared substrate in a two-dimensional array under the control of a trapezoidal voltage waveform as shown in Figure 6.8(b). A computer-controlled XY motorized stage positioned the droplets with a uniform spacing of $340\ \mu m$ (see Figure 6.8(c)). Droplet size could be adjusted by either changing the nozzle or depositing multiple droplets at the same location. In this experiment, 20 droplets were deposited at each site to produce final

droplets with a diameter of approximately 330 μm (see Figure 6.8(d)).

6.5 Simultaneous Polarization and Phase Sensing

Building on the measurement principles described earlier, the system has been designed to be structurally simple, cost-effective, and capable of real-time acquisition of both polarization and phase information. This integrated approach addresses the limitations of conventional systems, which often require separate, bulky optical arrangements for polarization and phase measurements, increasing complexity and cost. This section introduces a novel system that simultaneously measures the polarization and phase properties of multi-wavelength beams, leveraging the unique characteristics of the LC droplet array. Although the polarization and phase measurements are performed concurrently, they are analysed separately for clarity. The following subsections detail the system's configuration, experimental procedures, and results, demonstrating its ability to accurately retrieve the polarization and phase of a light beam.

6.5.1 Experimental design for full optical field measurements

To verify the capability of the LC droplet array-based sensing system to simultaneously measure the polarization and phase information of a beam, a series of experiments were conducted. **Figure 6.9** presents a schematic diagram that outlines the overall experimental workflow and logic.

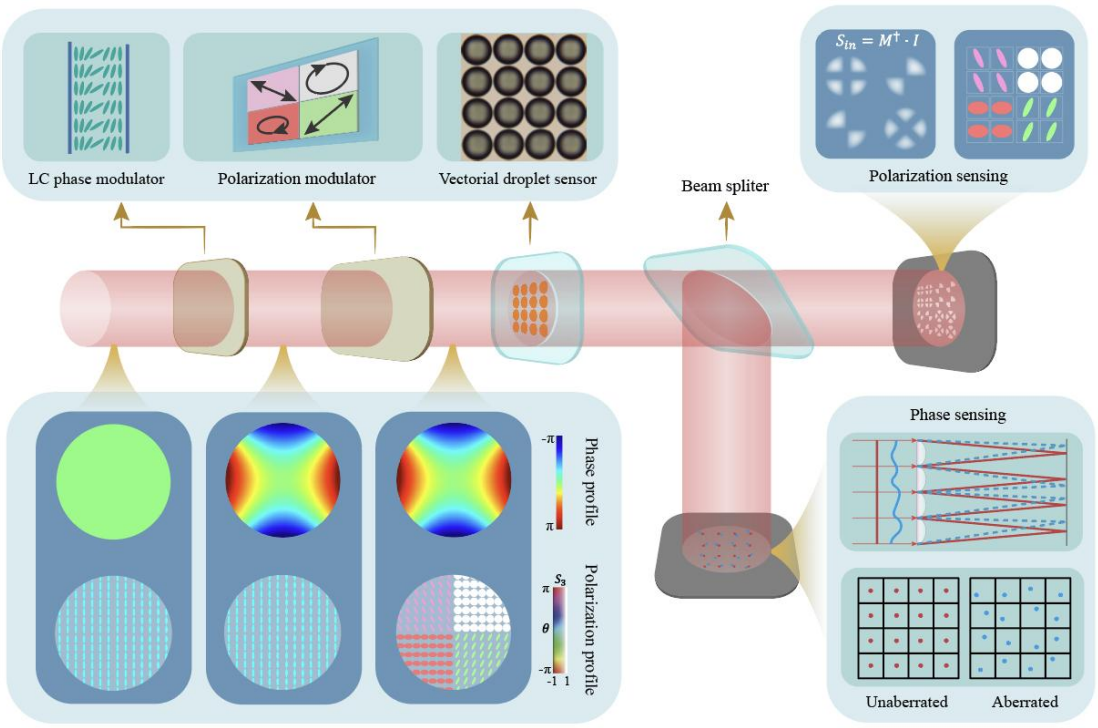


Figure 6.9 Schematic overview of the LC droplet array-based sensing system for simultaneous polarization and phase measurement of a light beam. The diagram summarizes the process: a controlled light beam is first modulated in phase (using an SLM or wedge cell) and in polarization (via a FWP), then directed into the sensing system. A beam splitter separates the beam into two channels — one for phase measurement (capturing focal spot shifts) and one for polarization analysis (recording droplet internal patterns) — allowing real-time reconstruction of the beam's vectorial properties.

An unmodulated laser beam, with uniform polarization and phase, was first directed through a phase modulation stage. At this stage, either a SLM or a wedge cell filled with nematic LC (E7) was used to impart a predetermined phase profile on the beam. Subsequently, the beam passed through a polarization modulation device — a four-division waveplate (FWP) assembled from half-wave plates (HWPs) and QWPs set at different angles. This arrangement modulated the SoP into four spatial regions, each with distinct polarization properties. Following modulation, the beam entered the detection system, and the modulated beam was analysed by a LC droplet array.

The beam was then split into two branches using a beam splitter. One branch was directed to a screen positioned at an imaging plane where the internal pattern of the droplet array was clearly resolved, allowing for the retrieval of polarization data via a calibrated system matrix A (as mentioned in Section 6.2.2). The other branch was sent to a second screen, located at the focal plane behind the droplet array, where the displacement of focal spots was measured to determine local phase variations (as mentioned in Section 6.3). By processing the information from both detection channels using the previously established analysing procedures, the system can reconstruct the Stokes vector and the phase distribution of the incident beam in real time.

To demonstrate the system's capability for simultaneous phase and polarization measurement, we directly implement a dual-wavelength experimental setup in which each beam carries independently controlled optical field properties. The experimental setup utilized is shown in **Figure 6.10**, a 633 nm helium-neon laser (HNLS008L-EC, Thorlabs) was used as one light source, emitting a vertically polarized beam. Directly after the laser, a HWP (WPHSM05-633**,** 633 nm, Thorlabs) rotated the linear polarization to 0°, ensuring that the beam aligned properly with the LC inside the SLM (Hamamatsu LCOS-SLM X15213-01) afterwards. This alignment was crucial for achieving high modulation efficiency, as the SLM's phase control depends on the polarization being parallel to the LC director.

Once the polarization was set, the beam is expanded by a 4*f* system composed of a

$10\times$ objective (RMS10X, 0.25 NA, Thorlabs) and a lens of $100\ \text{mm}$ focal length (AC254-100-A-ML, $f = 100\ \text{mm}$, ARC: 400-700 nm, Thorlabs). This 4*f* arrangement enlarged the beam's cross-section, ensuring uniform illumination across the SLM's active area. The beam then reflected off two mirrors (BB03-E02, 400-750 nm, Thorlabs) to maintain a small incident angle — less than $10°$ — on the SLM, with approximately $5°$ of deflection. Keeping the incident angle minimal was important for uniform phase modulation and minimal distortion.

The SLM was programmed to introduce known phase aberrations, often represented by Zernike modes, each with adjustable amplitude. By controlling these modes, the system can verify its phase measurement accuracy by applying specific wavefront distortions. After the SLM imposed the desired phase pattern, a second 4*f* system (AC254-100-A-ML, $f = 100\ \text{mm}$, ARC: 400-700 nm, Thorlabs) relayed the modulated wavefront to the next stage of the setup. The 4*f* configuration precisely mapped the pupil plane from the SLM onto the droplet array, ensuring that the phase aberrations remained accurately preserved for analysis.

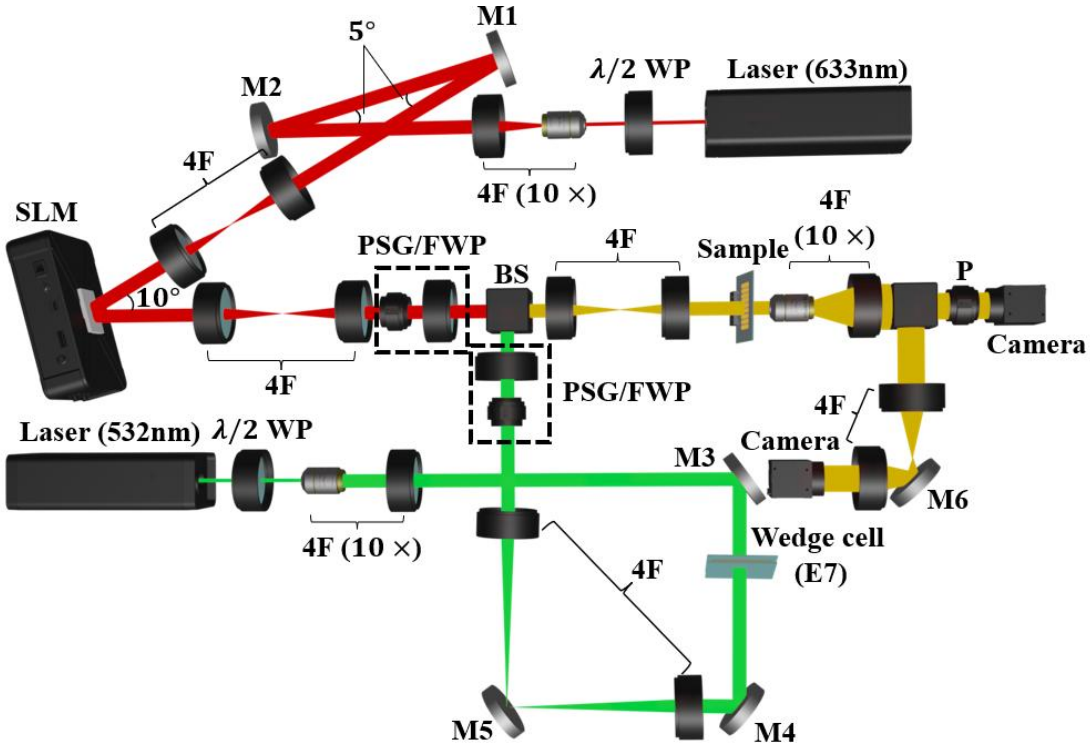


Figure 6.10 A schematic diagram of experimental setup for the multi-wavelength vectorial field sensing system. A 633 nm laser beam (red) is first polarization-aligned by a HWP and then phase-modulated by an SLM via a 10° incidence. Mirrors M1 and M2 relay the modulated beam through a 4*f* system before it enters the PSG/FWP, while the 532 nm green beam is modulated by a wedge cell filled with nematic LC (E7) and another FWP. The beams are combined and incident on a LC droplet array, after which a non-polarizing beam splitter divides the transmitted light into two arms. Two RGB cameras capture the output to independently extract phase and polarization information for both wavelengths. In the polarization arm, the droplet-array intensity is imaged through a fixed polarizer onto RGB cameras for Stokes vector reconstruction. In the phase arm, a second 4*f* relay the array's focal-spot pattern onto another RGB cameras for Shack-Hartmann-based wavefront analysis.

The next critical component in the setup was the PSG, which was used during calibration. The PSG consists of a polarizer (LPVISC050, 510-800 nm, Thorlabs) and a QWP (WPQSM05-633, 633 nm, Thorlabs) that together created a range of controlled SoP needed to calibrate the system matrix A. Once calibration was complete, the PSG was replaced by a FWP (HWP: WP280, 400-700 nm, Edmund Optics; QWP:

WP140HE, 400-700 nm, Edmund Optics) that modulates the beam's polarization across its cross-section, thereby generating spatially varying polarization patterns to test the system's polarization sensing ability.

A 532 nm green laser (532 nm DPSS Pointing Laser, 10 mW, Edmund Optics) was introduced alongside the existing 633 nm red source (HNLS008L-EC, Thorlabs). For the green-light path, phase modulation is introduced using a wedge cell filled with nematic LC (E7), which induced a tilt aberration due to its refractive index gradient. Since this modulation method differed from the red-light path, it provided a direct validation that the droplet array can simultaneously detect phase distortions at different wavelengths. The green beam then passed through a separate FWP, encoding distinct SoPs across different regions.

Both beams, carrying independently modulated phase and polarization information, were combined at a beam splitter (BS043, 400-700 nm, Thorlabs) and directed onto the droplet array for simultaneous sensing. To ensure that a clearly magnified image of the droplet array was obtained, a second $4f$ system — comprising a $10\times$ objective (RMS10X, 0.25 NA, Thorlabs) and a $100\ \mathrm{mm}$ focal length lens (AC254-100-A-ML, $f = 100\ \mathrm{mm}$, ARC: 400-700 nm, Thorlabs) — was used after the LC droplet array. This $4f$ system not only enlarged the image but also matched the droplet's natural numerical aperture of approximately 0.3 — this value followed directly from the droplet's $330\ \mu\mathrm{m}$ diameter and its $\sim 0.55\ \mathrm{mm}$ focal length ($NA \simeq D/(2f) \simeq$

$0.33\ \text{mm} / (2 \times 0.55\ \text{mm}) \approx 0.30$ when $D \ll 2f$).

Subsequently, a beam splitter (BS043, 400-700 nm, Thorlabs) divided the beam into two paths. In the first path, the beam passes through a polarizer set at $0°$ and is detected by a RGB cameras (Basler Ace acA4024-29uc, Edmund Optics), which naturally separate the red and green channels, enabling independent detection of their respective polarization information in a single measurement. The intensity information captured in each droplet image was used to reconstruct the incident beam's Stokes vector via the calibrated system matrix A. In the second path, the beam was relayed through another $4f$ system and directed to a separate RGB cameras (Basler Ace acA4024-29uc, Edmund Optics) that recorded the focal spots produced by each LC droplet. By analysing the displacements of these focal spots between an unaberrated wavefront and an aberrated wavefront, local wavefront slopes are determined, enabling precise phase reconstruction based on Zernike coefficients.

6.5.2 Polarization measurement result

A LC droplet array was fabricated according to the procedure in Section 6.4, ensuring a small inter-droplet spacing (about $10\ \mu\text{m}$) to maximize beam coverage while preventing adjacent droplets from merging. The MM of each droplet was then characterized using the method described in Section 5.4.1. This step confirmed that the retardance and fast-axis profiles matched those shown in Figure 6.1, indicating that each droplet could effectively provide a range of retardance values from 0 to π and

a radially oriented fast axis, these features allow each droplet to achieve comprehensive modulation of the incident light's vectorial properties. Once validated, the droplet array was placed into the optical setup illustrated in Figure 6.10, in order to evaluate its performance in simultaneously measuring polarization and phase under dual-wavelength conditions. The PSG produced 72 distinct SoPs to calibrate the system, yielding a system matrix A. During measurement, a beam with a specific SoP entered the droplet array, and the intensity patterns within each droplet were recorded by a CCD camera. Before recording, the camera position along the optical axis was finely adjusted to bring the droplet edges into sharp focus — this ensured that the recorded texture clearly reflected the internal optical modulation.

Figure 6.11shows examples of the droplet images obtained under various polarization inputs — such as horizontal (H), vertical (V), $\pm 45°$ linear (M, P), and left- or right-circular (L, R). Each SoP produces a distinct brightness pattern within each droplet, demonstrating the array's ability to discriminate between different SoPs. In the multi-wavelength polarization measurements, separate calibrations were required for the red and green beams because the LC material refractive indices differ, which leads to minor variations in the droplet's imaged size and position. This requirement leads to distinct system matrices for the red and green wavelengths, which were then used in subsequent calculations independently.

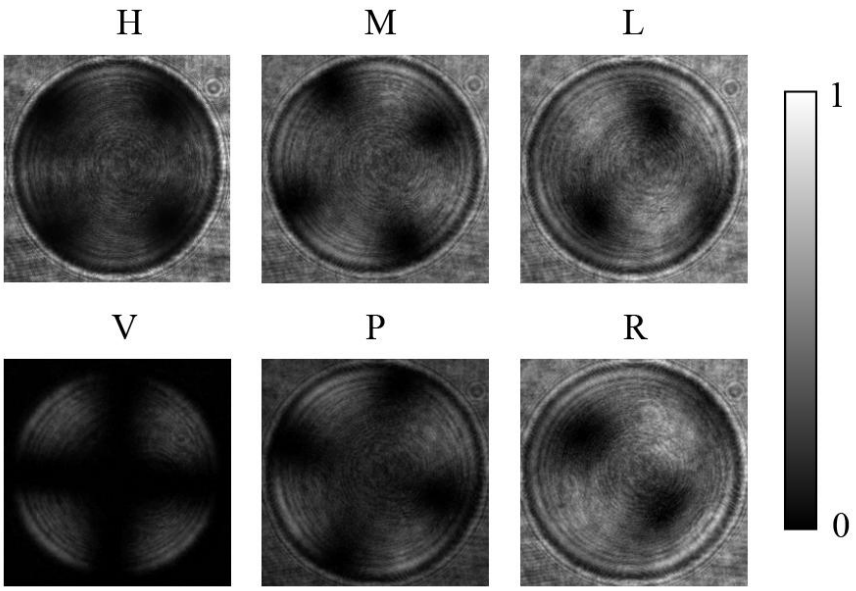


Figure 6.11 CCD-captured intensity patterns of a single droplet in the polarization sensing system for typical input SoPs: horizontal (H), vertical (V), $\pm 45°$ linear (M, P), and left- or right-circular (L, R).

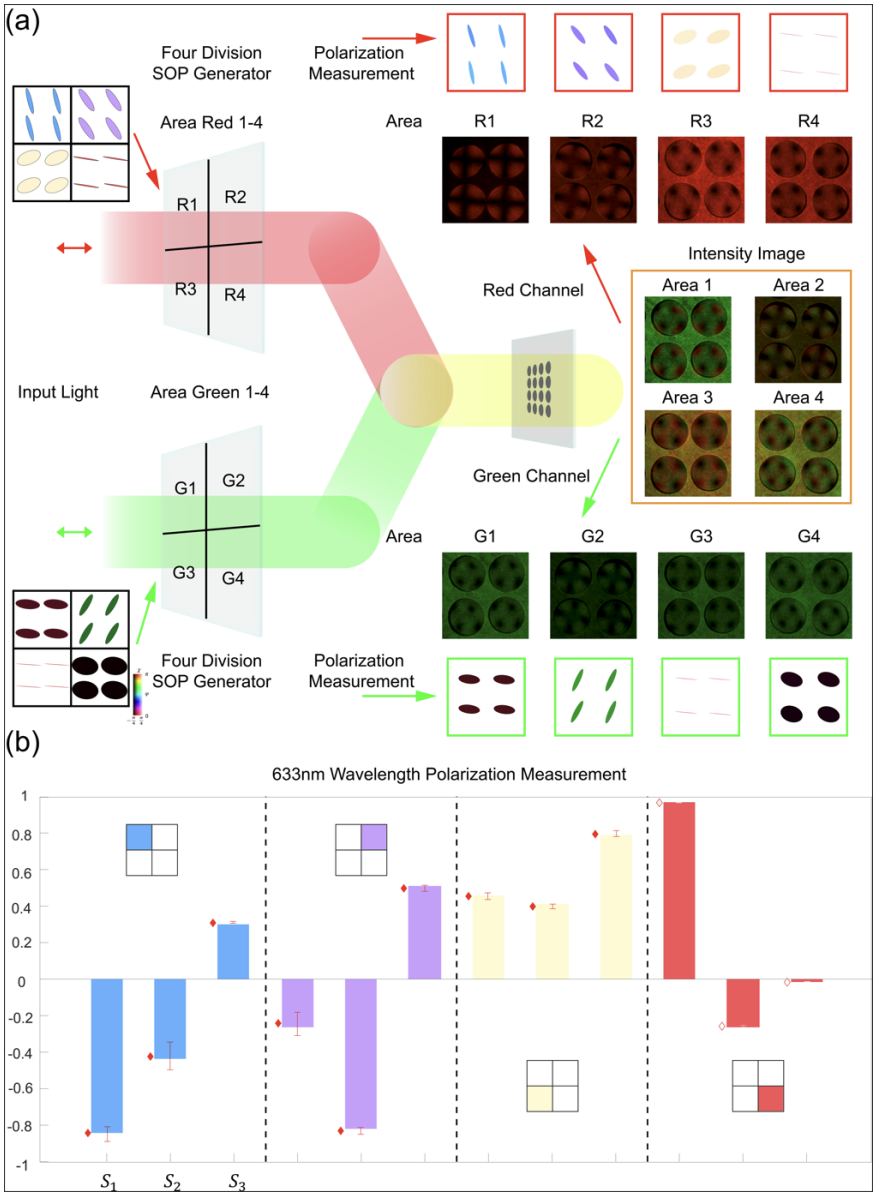


Figure 6.12 Dual-wavelength polarization measurement using the LC droplet array sensor. (a) The diagram illustrates the measurement configuration, input polarization states, and representative CCD images. The incident light contains red and green beams, each spatially divided into four quadrants with distinct polarization states. The output was recorded by an RGB camera, and the captured image was separated into red and green channels to independently analyse. Shown alongside are representative droplet images from each quadrant and the reconstructed polarization ellipses, clearly demonstrating the system's ability to resolve different SoPs across both wavelengths. (b) A quantitative comparison between the droplet-array results (red diamonds, representing the average of four droplets within each polarization region; error bars denote the corresponding spread) and the reference values (bar charts) shows close agreement for every Stokes parameter, confirming the system's accuracy.

To validate the polarization sensing capability of the LC droplet array system, a series of experiments was performed to measure the full Stokes vector of both incident beams. In the experiment, both the red and green beam are initially 0° linearly polarized. Each beam passes through its respective FWP, which modulates the incident light into four regions, each carrying a different SoP. The SoPs of the incident beams are characterized using the Stokes polarimetry method described in Section 6.2.3, and the corresponding polarization ellipses are determined (see **Figure 6.12Figure 6.12**(a)). The resulting Stokes vectors are represented as coloured polarization ellipses, where the ellipse parameters are derived from the Stokes components: the rotation angle ψ given by $2\varphi = \tan^{-1}(S_2/S_1)$ and the ellipticity χ computed from $2\chi = \sin^{-1}(S_3/S_0)$. With respect to the colour of the polarization ellipse, the HSL model was employed with saturation fixed at 1, lightness reflecting the degree of ellipticity χ (higher brightness indicating greater ellipticity), and hue representing the rotation angle φ.

These modulated beams were then combined and directed into the LC droplet array sensing system. Due to differences in the optical response for the SOP of red and green light, the resulting patterns comprise overlapping contributions from both wavelengths. An RGB camera naturally separated these contributions into red and green channels, thus, by analysing the intensity patterns in the respective channels and applying the pre-calibrated system matrix for each wavelength, the Stokes vector was computed for each droplet in every polarization region. The calculated Stokes vectors were then visualized as polarization ellipses, and comparison between these reconstructed polarization

ellipses and the expected input SoPs shows a high degree of agreement, confirming the system's ability to accurately measure polarization information across multiple wavelengths simultaneously (see Figure 6.12**Figure 6.12**(a)).

A more quantitative view is provided in Figure 6.12(b), where the three normalised Stokes parameters (S_1, S_2, S_3) are plotted separately for the four FWP-defined quadrants; dashed boxes outline the data that belong to each quadrant. Red diamonds mark the mean Stokes values retrieved from the four droplets in each quadrant, while the attached error bars show their standard deviation, and the bars represent the reference measurements. For clarity, only the measurement results for the red beam are shown here as a representative example. Across all Stokes parameters, the experimental data and reference values align closely, demonstrating that the LC droplet array system accurately measures SoPs at a single wavelength.

6.5.3 Phase measurement result

To evaluate the phase measurement performance of the system for vectorial light fields, we introduced controlled wavefront aberrations using a SLM. Based on the previously established calibration (see Figure 6.7), each SLM input amplitude was mapped to a physically meaningful RMS OPD. The SLM was programmed to generate individual phase aberrations corresponding to selected Zernike polynomials, allowing us to benchmark the system's ability to accurately reconstruct both the shape and strength of known wavefront distortions.

In the experiment, the SLM generated a disk-shape aberration pattern with radius of $10\ \mathrm{mm}$, while the effective pupil captured by the CCD camera that defined by the size of the LC droplet array was only $2\ \mathrm{mm}$ in diameter. To ensure that the intended phase aberration amplitudes were accurately applied within this smaller pupil, a scaling procedure was implemented based on the radial dependence of Zernike modes. Because Zernike polynomials are orthogonal over the disk-shape pattern generated by the SLM and their amplitude scales with radial distance, the effective amplitude within a reduced pupil size must be compensated accordingly. Specifically, if the full SLM aperture is defined as having a normalized radius of 1, then the LC droplet array occupies only 0.2 of this radius (i.e., $\frac{2\ \mathrm{mm}}{10\ \mathrm{mm}} = 0.2$). Therefore, for Zernike modes of different radial orders, a scaling factor proportional to the inverse of this radius raised to the power of the mode's radial order was applied. For instance, First-order modes, such as tilt, scale linearly with radius and were therefore multiplied by $\frac{1}{0.2} = 5$, Second-order modes, such as defocus or astigmatism, scale quadratically and were multiplied by $\frac{1}{(0.2)^2} = 25$. For clarity, all mentioned phase aberration amplitudes refer exclusively to those actual amplitude applied on the pupil.

To evaluate the system's phase measurement accuracy, we conducted experiments using the red channel of the dual-wavelength setup as a representative example. First, a reference image was recorded at the focal plane with no phase aberration, establishing baseline positions of the focal spots. The SLM was then used to sequentially apply four distinct aberrations, each corresponding to a single Zernike mode with a known RMS

OPD. Spot displacements induced by these aberrations were measured relative to the baseline and used to reconstruct the wavefront phase.

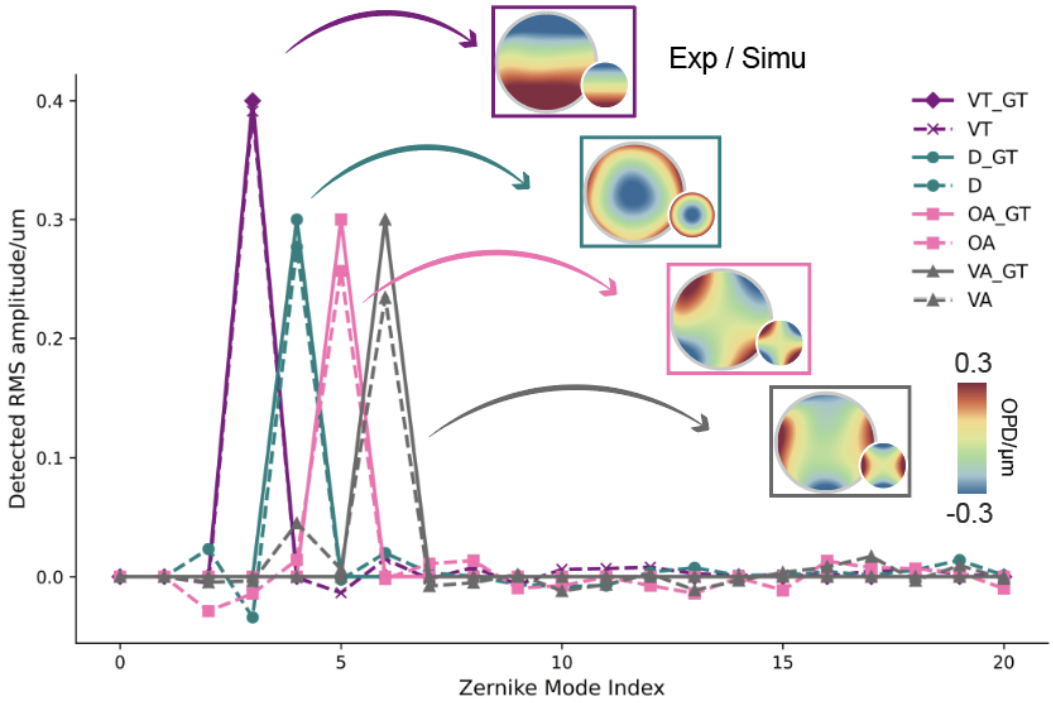


Figure 6.13 Reconstructed Zernike coefficients and phase maps for four known aberrations. The plot shows experimentally retrieved Zernike coefficients (solid lines) compared with ground truth values (dashed lines) for vertical tilt (VT), defocus (D), oblique astigmatism (OA), and vertical astigmatism (VA), applied via a calibrated SLM. Insets show reconstructed 2D phase maps (left, larger image) alongside simulated references (right, smaller image), confirming accurate phase retrieval in both amplitude and spatial profile. 'GT' refers to the ground truth Zernike coefficients corresponding to the known aberrations applied by the calibrated SLM.

Figure 6.13 presents the results of this validation. The line plot shows the experimentally retrieved Zernike coefficients (solid lines with markers) alongside the simulated ground truth values (dashed lines) for four key aberrations: horizontal tilt (0.4 μm RMS), defocus (0.3 μm RMS), vertical astigmatism (0.3 μm RMS), and oblique astigmatism (0.3 μm RMS). The x-axis labels correspond to the standard

Zernike mode indices. In each case, the dominant mode appears as a peak at the expected position, while all other modes remain near zero, confirming the sensor's selectivity.

The inset images show the corresponding 2D reconstructed phase profiles (left sub-circles) compared with their theoretical counterparts (right, smaller sub-circles), both visualised using the same colour scale representing OPD relative to a flat wavefront. The close match in both coefficient amplitude and spatial phase pattern confirms that the droplet-array-based sensor accurately resolves low-order aberrations in vectorial beams.

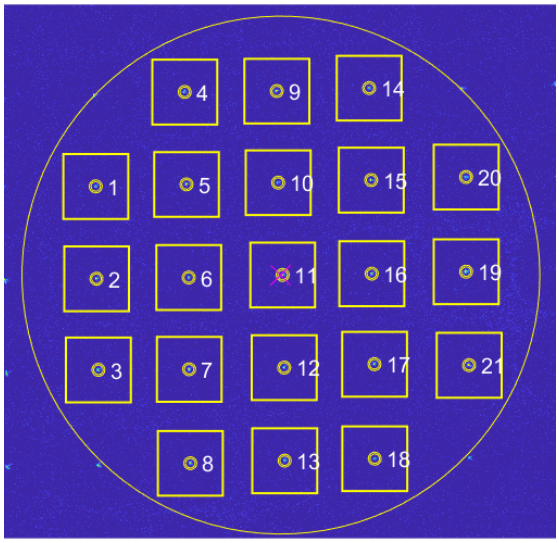


Figure 6.14 Detected droplet sub-apertures within the effective pupil region. A total of 21 droplets were used for wavefront reconstruction, as highlighted by the numbered yellow boxes. The limited number of sub-apertures constrains the system's ability to resolve higher-order Zernike modes.

In this study, the focus has been on low-order Zernike modes, as the number of droplets captured within the effective pupil limits the maximum resolvable spatial complexity of the wavefront. As shown in **Figure 6.14**, only 21 droplets fall within the

measurement region imaged by the CCD camera. This number is sufficient for accurate reconstruction of low-order aberrations such as tilt, defocus, and astigmatism, but is insufficient to reliably resolve higher-order modes that require finer spatial sampling. Due to the physical size of each droplet and the optical magnification used, further increasing the number of droplets within the pupil would require either smaller droplets or a wider field of view.

To evaluate the phase sensing capability of the system under dual-wavelength conditions, experiments were conducted using two simultaneously incident beams carrying different, independently controlled phase distortions. As shown in **Figure 6.15**(a), a $633\ \mathrm{nm}$ red beam was modulated using an SLM to impose well-defined Zernike phase aberrations, while a $532\ \mathrm{nm}$ green beam was modulated by passing through a wedge cell filled with nematic LC (E7), which introduced a variable tilt depending on cell orientation. The two beams were combined and directed into the LC droplet array, where their wavefronts were simultaneously measured and separated via the RGB detection scheme. On the sensor side, the focal spots corresponding to the red and green beams appeared at different positions within each droplet due to their distinct aberration profiles, as illustrated schematically in Figure 6.15(a).

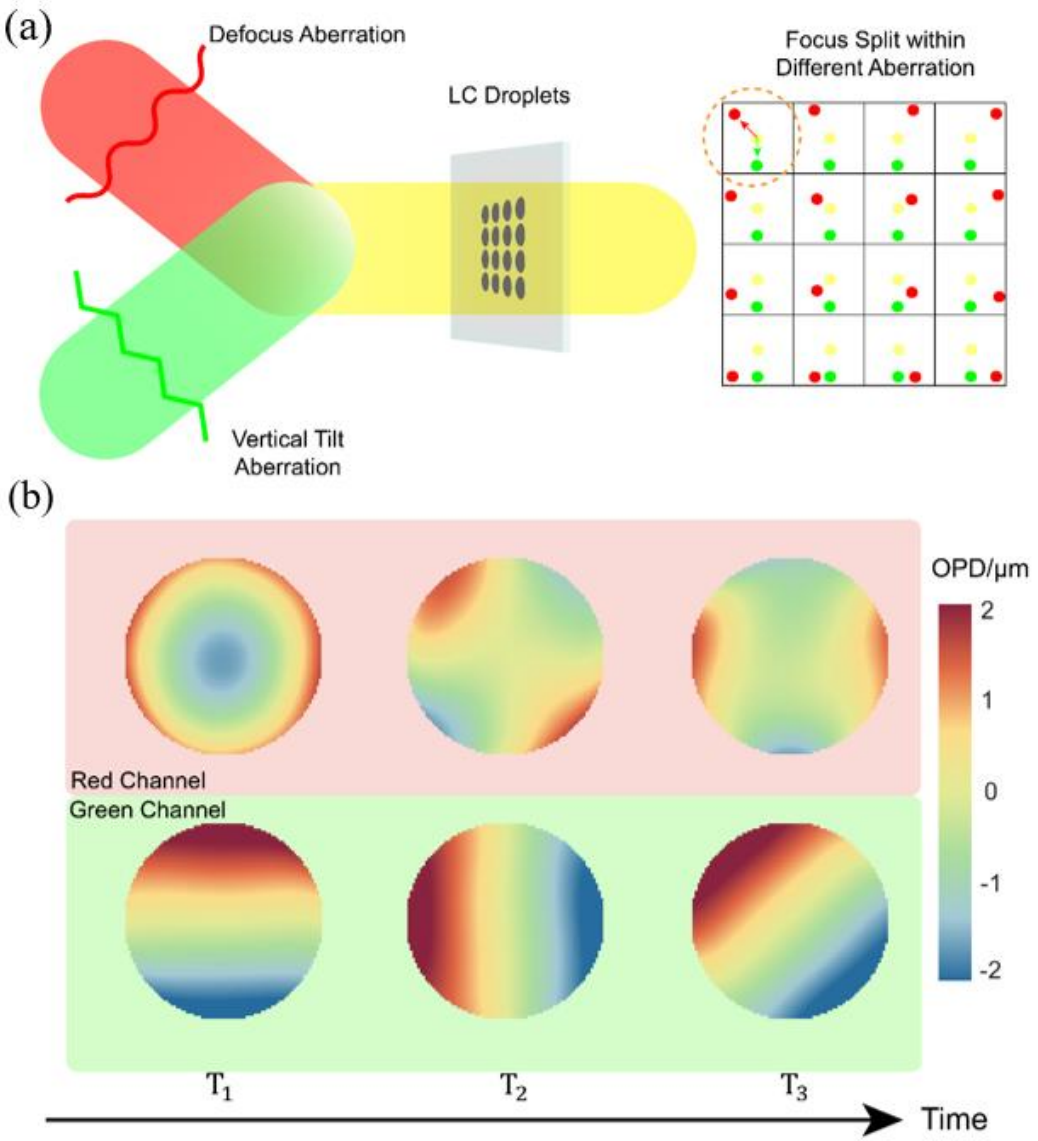


Figure 6.15 Dual-wavelength phase-sensing demonstration. (a) Experimental concept: a 633 nm red beam is phase-modulated by the SLM, while a 532 nm green beam acquires tilt aberrations from an LC wedge cell (tilt angle of $\tan^{-1}(0.00763)$). After both beams pass through the LC-droplet array, their focal spots (red and green dots) are spatially separated in each droplet. (b) Reconstructed OPD maps for three successive test cases T_1, T_2, T_3. The red channel (top row) recovers SLM-imposed defocus, vertical astigmatism and oblique astigmatism, respectively; the green channel (bottom row) simultaneously retrieves vertical, horizontal and combined tilt aberrations. Colour scale: OPD relative to a planar wavefront.

To systematically explore the system's response, three phase conditions were tested for the green beam: vertical tilt, horizontal tilt, and a combination of both. Meanwhile,

the red beam was assigned different low-order aberrations in each case — defocus, vertical astigmatism, and oblique astigmatism, respectively. Figure 6.15(b) shows the reconstructed 2D phase profiles at three different time steps (T_1, T_2, T_3), with red and green channels plotted separately. The recovered phase maps show strong agreement with the imposed aberrations in both spatial distribution and relative magnitude. For reference, the wedge cell tilt angle of $\tan^{-1}(0.00763)$ corresponds to a maximum OPD variation of approximately $1.91\ \mu m$ across the pupil, confirming that the sensor effectively resolves even subtle tilt components in the green channel. These results verify that the LC droplet array sensor can accurately decompose and retrieve wavelength-specific phase aberrations in real time, even when two beams with distinct profiles are simultaneously present.

6.5.4 Error analysis for polarisation and phase measurements

We should note that recent demonstrations in both polarisation and phase sensing are proof-of-concept only, and detailed error analysis, along with further enhancement strategies, are still required.

For polarisation sensing, errors mainly arise from systematic errors due to imperfections of the LC droplet, other optical elements, detector imperfections, and beam profile variations, as well as random noise such as Gaussian noise. Thus, the improvement strategy includes: 1) Calibration: A systematic calibration method should be applied to droplet polarimetry — for instance, the illuminated Stokes vectors should

cover as much of the Poincaré sphere as possible to precisely estimate the instrument matrix. 2) Optimisation: The droplet profile can be optimised. Currently, we use the entire droplet as an analysing channel. However, as the 132° retardance has been shown to provide the best condition number[183], the droplet should be designed to utilise regions near this optimal retardance for measurements, while maintaining the best conditional number. 3) Denoising: Multiple images can be acquired to average out Gaussian and Poisson noise. Moreover, novel approaches such as using pure imaging data as training sets for machine learning[211] can combine calibration, optimisation, and denoising into a single high-performance step.

For phase sensing, the key factor causing unexpected errors is geometric phase[212]. Since the droplet is a spatially varying birefringent device, it modulates both phase and polarisation, making the actual wavefront anisotropic, i.e., a combination of two distinct wavefronts corresponding to orthogonal polarisation states. In all our previous work, we temporarily neglected geometric phase effects, assuming them to be minimal. Although this allowed us to retrieve most of the phase profile, significant barriers remain for high-precision phase retrieval. Thus, future strategies should include: 1) Introducing a circular polarisation beam splitter after the droplet to separate the sensing beam into two orthogonal polarisation states with distinct wavefronts. Two sets of cameras can then acquire two distinct spot patterns, from which the complete phase profile can be accurately reconstructed. Considering spin-orbit interaction effects[212], we know geometric phase primarily affects beams of a single handedness. Thus, an

engineering strategy could be defining the geometric phase contribution of the droplet (quickly measured via in-situ Mueller matrix polarimetry or pre-calibrated by testing a simple input wavefront such as tip or tilt), and identifying the sensing arm (without geometric phase contributions) as the high-precision SHWS. 2) Optimisation of the droplet design could further reduce geometric phase impact on the sensed input wavefront. Note, the birefringence cannot be entirely flattened, as it is essential for polarisation sensing. 3) Although multiple images can be acquired for denoising, incorporating machine learning would be beneficial. With enough training data, machine learning methods might directly extract the true input phase profile without geometric phase interference — this promising route is definitely worth exploring.

6.6 Intensity Retrieval Capability

Beyond polarization and phase, our system also enables estimation of the absolute optical intensity of the incident beam. This is achieved by analyzing the greyscale values in the background regions of the CCD image, which are the areas outside the droplet array where the light passes through unmodulated. These regions retain the original beam profile and provide a direct channel for intensity sensing.

To convert pixel values into absolute intensity units (e.g., $\mu W/cm^2$), the system accounts for the camera's exposure time and gain. Under uniform illumination, the

recorded grey level G (0-255) is approximately proportional to the incident optical power P according to:

$$P \propto \frac{G}{t \cdot g} \tag{6.11}$$

where t is the exposure time and g is the gain factor. A one-time calibration using a known reference light source allows this proportionality to be quantified, yielding a conversion factor from pixel value to absolute optical intensity. Once calibrated, the system can recover intensity maps alongside phase and polarization with no added hardware.

It is worth noting that this intensity recovery assumes stable illumination across the region and no significant clipping or optical loss. In cases where such assumptions break down, a compensation procedure based on prior system response characterization can be applied. Overall, this approach allows the system to retrieve absolute optical intensity by analysing the background greyscale levels, with calibration based on exposure time, gain, and pixel response.

6.7 Summary

In conclusion, the LC droplet array-based sensing system developed in this study enables simultaneous measurement of phase, polarization, and intensity across multiple wavelengths within a single compact platform. By exploiting the wavelength-selective response of an RGB camera and the polarization- and phase-sensitivity of the LC droplets, the system performs full-field optical characterization without the need for

moving parts, active scanning, or multiple optical paths. This architecture offers a low-cost, easily fabricated, and scalable solution for real-time analysis of complex vectorial light fields. For polarization sensing, each droplet serves as an independent measurement unit under a DoWP scheme, enabling real-time calculation of the full Stokes vector across the beam. For phase sensing, the droplets function similarly to a SHWS by focusing the beam into sub-apertures, from which local wavefront slopes and the corresponding Zernike coefficients are derived to describe phase aberrations. Additionally, integrating an RGB camera naturally provides wavelength and intensity data, facilitating simultaneous multi-wavelength detection. Together, these features yield a comprehensive instrument capable of accurately characterizing the amplitude, phase, polarization, and spectral properties of light.

Chapter 7

Conclusions and Future work

"What we call the beginning is often the end. And to make an end is to make a beginning."

T.S. Eliot

7 Conclusions and Future work

The work presented in this thesis focuses on exploiting the properties and potential applications of inkjet-printed LC droplets — a subject that has been largely underexplored. LC materials exhibit unique responsiveness to their surroundings and possess inherent optical birefringence. When combined with confined droplet structures, these attributes make the system particularly attractive. In this study, both theoretical and experimental investigations were conducted to elucidate the internal director configurations and optical behaviour of both nematic and chiral nematic LC droplets under various conditions. The insights gained from these studies have provided the foundation for the development of new methods in beam generation and beam analysis, as described in the latter parts of the thesis.

7.1 Concluding remarks

In Chapter 1, the primary aim and motivation were introduced, highlighting the exploration of inkjet-printed LC droplets on glass substrates, along with an overview of the thesis structure. Chapter 2 reviewed the essential background of LCs, detailing their intrinsic physical properties, which were crucial for understanding their behaviour and potential applications. This background set the stage for the theoretical and experimental work that followed. Chapter 3 then described the experimental methods in detail, including substrate preparation and the inkjet printing processed for producing well-defined LC droplet arrays.

To systematically understand and classify the diverse behaviours of inkjet-printed LC droplets under varying conditions, a regime mapping study was conducted (Chapter 4). The investigation focused on characterizing the internal director configurations of droplets deposited on glass substrates under both homeotropic and planar alignment conditions while varying the chiral dopant concentration for chiral nematic LC droplets. In this Chapter, the helicity number $N_0 = 2h/P$ as a key dimensionless parameter to classify the internal configurations of printed LC droplets, where h is the droplet height and P is the chiral pitch. The droplets were printed using an $80\ \mu m$ nozzle and consistently formed with a lateral diameter of approximately $120 \pm 10\ \mu m$ and a height of $28 \pm 2\ \mu m$. By adjusting the concentration of the chiral dopant, the pitch was tuned from the nematic limit (infinite pitch) down to $2.5\ \mu m$, yielding a corresponding N_0 range from 0 to approximately 25. In the homeotropic case, droplets with low N_0 exhibited radial-like configurations, while increasing chirality led to the emergence of fingerprint textures. In contrast, droplets on planar substrates evolved to spiral structures. These trends were consistently reproduced in simulations, confirming the role of geometry, pitch, and surface anchoring in determining director patterns. This integrated approach provided critical insights into the optical properties and potential applications of LC droplet arrays, forming the basis for further advances in photonic device technology.

Chapter 5 began by reviewing essential concepts from vectorial optics that are fundamental to this study, including the description of vector light fields, the principle

of vectorial light responses, and the operational principles of polarimeters and interferometers. These concepts provided the theoretical background required to understand how the phase and polarization of light can be controlled and measured. Building on this foundation, the chapter explored the application of the printed LC droplets considered in the previous chapter for generating structured light fields. Optical techniques — specifically, interferometry and MM polarimetry — were employed to investigate the optical properties of LC droplets. By employing nematic achiral and chiral LC droplets on both homeotropic and planar alignment layers, this approach takes advantage of the intrinsic birefringence of LCs to broaden the range of achievable optical modulations. In particular, structured light fields were produced that exhibited a full Poincaré beam with spatially varying SoPs and two units of OAM, as well as beams with both azimuthal and radial polarization distributions, and beams that contain polarization singularities. These distinct light fields underscore the versatility of LC droplets as a platform for generating complex optical fields.

In Chapter 6, based on the insights gained from previous chapters regarding the optical properties of various LC droplets, a system capable of addressing complex optical problems was developed based on a nematic LC droplet printed onto a homeotropic alignment layer. This chapter introduces a full-field optical sensing system that simultaneously measures both polarization and phase information. For polarization measurements, the system employs Stokes polarimetry, which reconstructs the complete SoP by analysing the intensity data from the droplet-modulated light pattern

captured by the CCD camera. In our approach, each LC droplet acts as an independent modulation element, effectively replacing the function of a rotating QWP, thereby allowing the Stokes vectors across the beam to be determined in a single shot. For phase sensing, the droplets function similar to a SHWS by focusing the beam into sub-apertures, from which local wavefront slopes and the corresponding Zernike coefficients are derived to describe phase aberrations. By integrating these two measurement techniques with an RGB detector which naturally provides wavelength and intensity information the system achieves simultaneous, real-time full-field characterization of amplitude, phase, polarization, and spectral properties.

The next section of this Thesis describes future work that could be performed to continue the research described here, as well as to discuss avenues of research suggested by my results.

7.2 Future Work

Future work should focus on improving the performance and versatility of both structured light generation and full optical field sensing based on LC droplet arrays, through the following directions: 1. Optimizing alignment layers to achieve more uniform and controllable droplet anchoring conditions, which can improve device reproducibility and measurement accuracy. 2. Introducing external electric fields to dynamically tune the internal director configuration of LC droplets, enabling reconfigurable phase and polarization modulation. 3. Developing full Poincaré beam

illumination using single printed droplets as compact structured light sources for polarization-resolved imaging. 4. Exploring alternative LC mixtures with higher birefringence, faster response time, or tailored dispersion properties to enhance multi-wavelength performance and temporal resolution.

7.2.1 Patterned alignment for enhanced structured light generation

One promising direction for future work involves expanding the range of structured light patterns that can be generated by overcoming the limitations imposed by conventional alignment layers. In typical devices, the alignment layer enforces a single, uniform director orientation — either planar or homeotropic — which restricts the diversity of the achievable light field structures. An alternative approach might leverage direct laser writing (DLW) on photoalignment layers doped with a photosensitive azo-dye material, such as SD1[213]. Under laser exposure, the SD1 molecules undergo local reorientation, enabling the precise patterning of the alignment layer[214]. This technique allows for the creation of spatially varying director alignment across the substrate, which in turn facilitates the generation of a much broader variety of structured light fields. Such an approach could lead to the production of custom-designed optical patterns with tailored phase and polarization features, significantly enhancing the functionality of structured light-based applications in fields like optical communication, imaging, and quantum information processing.

7.2.2 Dynamic Tuning of LC Droplets

A promising strategy could be explored that leverages the intrinsic sensitivity of LCs to electric fields for real-time tuning of the optical response of the printed LC droplets. By applying an electric field, the LC director configuration within the droplet can be adjusted on demand, thereby enabling dynamic control over the properties of the resulting structured light. Furthermore, the approach combines DLW for local curing with electrical tuning; specifically, DLW is employed to selectively cure spatial regions within the LC droplet, forming polymer networks that permanently lock the LC director in those areas, while the remaining, uncured regions retain their responsiveness to applied electric fields[215]. This hybrid strategy not only ensures stable, spatially controlled director profiles but also allows for subsequent dynamic modulation of the droplet's optical properties. Such a capability is anticipated to substantially broaden the range of structured light patterns that can be generated, which is particularly advantageous for applications requiring tunable optical functionality.

7.2.3 Full Poincaré Beam-Based Structured Illumination

A promising direction is to implement the nematic LC droplet printed on homeotropic alignment layer as a structured illumination module for polarization-sensitive imaging, using the full Poincaré beam as the light source. This type of beam carries all possible polarization states across its transverse profile, making it well-suited for probing spatial variations in sample anisotropy. Unlike conventional imaging systems that require

multiple illumination states to reconstruct polarization information, the use of a single full Poincaré beam allows all polarization channels to be simultaneously encoded into the interaction with the sample.

To realize this, the droplet should be printed onto a transparent substrate with homeotropic alignment layer and illuminated by a collimated circularly polarized laser beam. The beam emerging from the droplet can then be directed onto a sample with known or expected birefringence. The transmitted or reflected light is then captured using a Stokes imaging system, with a rotating QWP and polarizer configuration. By comparing the polarization distribution before and after interaction with the sample, one can retrieve spatially resolved information about the sample's optical anisotropy, including retardance, orientation, and depolarization index. This method could enable rapid, label-free analysis of materials that exhibit subtle polarization responses, without the need for active polarization modulation. Furthermore, because the LC droplet is compact and passive, the system has the potential to be miniaturized for portable polarimetric diagnostics or integrated into advanced microscopy platforms.

7.2.4 High resolution full optical field sensing

In our full optical field sensor project, the nematic LC droplets based on E7 must be relatively large — at least $300\ \mu m$ in diameter — to attain full retardance ranging from $0°$ to $180°$. This full retardance range is essential, because an incomplete range would introduce significant measurement errors. Each droplet functions as an

independent channel for detecting the Stokes vector, effectively serving as one pixel in the sensor. However, larger droplets inherently lower the spatial resolution of the measurement system. To address this limitation, it is necessary to identify LC droplet systems that preserve the advantageous properties of nematic LC droplets (such as their responsiveness and high birefringence) while also allowing for a reduced droplet size with a full retardance range. Preliminary experiments indicate that negative LCs may offer such a solution.

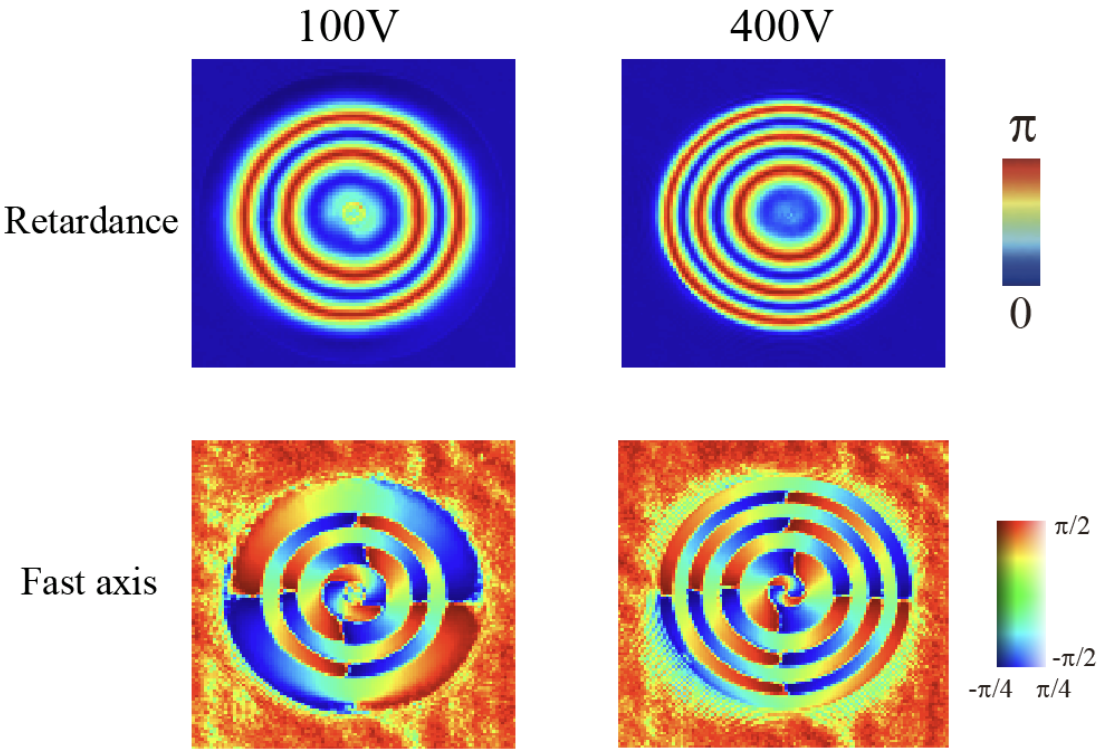


Figure 7.1 Retardance and fast axis distribution of a negative dielectric anisotropy liquid crystal (LC) droplet with a diameter of 150 μm under two applied voltages: 100 V (left) and 400 V (right). The droplet was printed onto an ITO-coated glass substrate and subsequently enclosed by another ITO-coated cover glass. A 50 μm spacer was used to define the cell gap and prevent compression of the droplet, ensuring preservation of its internal structure while enabling uniform electric field application across the droplet. The colour scale indicates phase shifts from 0 to π. The fast axis was characterized using the Hue-Saturation-Luminance model: hue represents the elliptical axis orientation; luminance indicates the degree of ellipticity.

In a LC with positive dielectric anisotropy, the director tends to align parallel to the electric field, making the fast optical axis also align with the field direction. By contrast, a LC with negative dielectric anisotropy orients the director (and thus its fast axis) perpendicular to the applied field. This difference arises from how each type of LC's molecular dipole moment and permittivity interact with the external electric field. As a result, for negative dielectric anisotropy LCs, applying a voltage forces the director to align orthogonal to the field, enabling distinct optical and electro-optical characteristics compared to positive LC systems.

Here, we experimentally tested a negative dielectric anisotropy LC mixture (VATS-14, Instec) to evaluate its electro-optic tunability. When a VATS-14 droplet was sandwiched between two ITO-coated glass substrates, an electric field applied in the vertical (up-down) direction causes the LC director to tilt perpendicularly to the electric field, inducing a large change in the droplet's effective birefringence. In contrast, the director within a positive dielectric anisotropy LC droplet under the same conditions would align parallel to the field, effectively cancelling the radially varying retardance. For the negative dielectric anisotropy LC droplets, however, increasing the applied voltage increases the tilt within the droplet, thereby enlarging the range of achievable phase shifts.

Figure 7.1 illustrates a negative dielectric anisotropy LC droplet with a diameter of 150 μm, confined in a cell with a 50 μm gap, was characterized under different

applied voltages to assess its modulation capabilities. At 100V, the droplet exhibits two full 0° to 180° retardance profile; when the voltage is increased to 400V, an additional 180° ring appears. In combination with the corresponding fast axis orientation data — which confirms that the fast axis is radially aligned — the results indicate that even a relatively small droplet can achieve a complete modulation range comparable to that of a rotating QWP. Consequently, combining negative dielectric anisotropy LC droplets with high-resolution printing methods, such as EHD printing to achieve diameters on the order of 1 μm to 10 μm, could greatly enhance the sensing resolution.

Reference

1. Silva TC, Eppink M, Ottens M. Automation and miniaturization: enabling tools for fast, high-throughput process development in integrated continuous biomanufacturing. *J Chem Technol Biotechnol* **2022**, 97, 2365-2375.
2. Piechulek N, Xu L, Fröhlich J, Bründl P, Franke J. Miniaturization Potential of Additive-Manufactured 3D Mechatronic Integrated Device Components Produced by Stereolithography. *Micromachines* **2025**, 16, 16.
3. Licardo JT, Domjan M, Orehovački T. Intelligent Robotics—A Systematic Review of Emerging Technologies and Trends. *Electronics* **2024**, 13, 542.
4. Hoath SD. Fundamentals of inkjet printing: the science of inkjet and droplets. *John Wiley & Sons* **2016**, 419.
5. Qiu X, Gong X, Zhang X, Zheng W. Ink-Jet Printing towards Ultra-High Resolution: A Review. *Coatings* **2022**, 12, 1893.
6. Kim Y, Park J, Yoon W, Kim J, Jung S. Drop-on-demand inkjet-based cell printing with 30-μm nozzle diameter for cell-level accuracy. *Biomicrofluidics* **2016**, 10, 064110.
7. Elkaseer A, Chen KJ, Janhsen JC, Refle O, Hagenmeyer V, Scholz SG. Material jetting for advanced applications: A state-of-the-art review, gaps and future directions. *Addit Manuf* **2022**, 60, 103270.
8. Arango JC, Pintro CJ, Singh A, Claridge SA. Inkjet Printing of Nanoscale Functional Patterns on 2D Crystalline Materials and Transfer to Soft Materials. *ACS Appl Mater Interfaces* **2024**, 16, 8055-8065.
9. Azizi Machekposhti S, Mohaved S, Narayan RJ. Inkjet dispensing technologies: recent advances for novel drug discovery. *Expert Opin Drug Discov* **2019**, 14, 101-113.
10. Zapka W. Inkjet printing in industry: Materials, technologies, systems, and applications. *John Wiley & Sons* **2022**, 3, 405.
11. Acosta C, Flynn WP, Santillan L, Garnsey S, Bhalla AS, Guo R. The Performance Characterization of a Drop-on-Demand Inkjet-Printed Gold Film Under the Temperature Conditions for Airborne Equipment. *J Compos Sci* **2025**, 9, 231.
12. Sirringhaus H. Inkjet Printing of Functional Materials. *MRS Bull* **2003**, 28, 802-806.
13. Koide N. Liquid Crystal Display Story. *Springer* **2016**, 1-5.
14. Yin K, Hsiang E-L, Zou J, Li Y, Yang Z, Yang Q*, et al.* Advanced liquid crystal

devices for augmented reality and virtual reality displays: principles and applications. *Light Sci Appl* **2022**, 11, 161.

15. Lazarev G, Chen P-J, Strauss J, Fontaine N, Forbes A. Beyond the display: phase-only liquid crystal on Silicon devices and their applications in photonics. *Opt Express* **2019**, 27, 16206-16249.

16. Agarwal S, Srivastava S, Joshi S, Tripathi S, Singh BP, Pandey KK*, et al.* A Comprehensive Review on Polymer-Dispersed Liquid Crystals: Mechanisms, Materials, and Applications. *ACS Mater Au* **2025**, 5, 88-114.

17. Ukleja P. Liquid Crystals (Physics). *Encyclopedia of Physical Science and Technology* **2003**, 717-739.

18. Huang Y, Hsiang E-L, Deng M-Y, Wu S-T. Mini-LED, Micro-LED and OLED displays: present status and future perspectives. *Light Sci Appl* **2020**, 9, 105.

19. Tsujimura T. *OLED display fundamentals and applications*. John Wiley & Sons, **2017**, 1-5.

20. Li M, Elston SJ, He C, Qiu X, Castrejón-Pita AA, Morris SM. Printed Liquid Crystal Optical Vortex Beam Generators. *Adv Opt Mater* **2024**, 12, 2400450.

21. Lee H-G, Munir S, Park S-Y. Cholesteric Liquid Crystal Droplets for Biosensors. *ACS Appl Mater Interfaces* **2016**, 8, 26407-26417.

22. Humar M. Liquid-crystal-droplet optical microcavities. *Liq Cryst* **2016**, 43, 1937-1950.

23. Humar M, Muševič I. 3D microlasers from self-assembled cholesteric liquid-crystal microdroplets. *Opt Express* **2010**, 18, 26995-27003.

24. McGloin D. Droplet lasers: a review of current progress. *Rep Prog Phys* **2017**, 80, 054402.

25. Bajc J, Zumer S. Structural transition in chiral nematic liquid crystal droplets in an electric field. *Phys Rev E* **1997**, 55, 2925-2937.

26. Bezić J, Žumer S. Structures of the cholesteric liquid crystal droplets with parallel surface anchoring. *Liq Cryst* **1992**, 11, 593-619.

27. Smalyukh II, Lansac Y, Clark NA, Trivedi RP. Three-dimensional structure and multistable optical switching of triple-twisted particle-like excitations in anisotropic fluids. *Nat Mater* **2010**, 9, 139-145.

28. Xu S, Ren H, Liu Y, Wu S-T. Color Displays Based on Voltage-Stretchable Liquid Crystal Droplet. *J Disp Technol* **2012**, 8, 336-340.

29. Parry E, Bolis S, Elston SJ, Castrejón-Pita AA, Morris SM. Drop-on-Demand Inkjet Printing of Thermally Tunable Liquid Crystal Microlenses. *Adv Eng Mater* **2018**, 20, 1700774.

30. He Z, Gou F, Chen R, Yin K, Zhan T, Wu S-T. Liquid Crystal Beam Steering Devices: Principles, Recent Advances, and Future Developments. *Crystals* **2019**, 9, 292.

31. Jiang L, Shui Q, Han B, Huang R, Deng J, Hu N*, et al.* Recent advances in liquid crystal droplet-based biosensors. *TrAC, Trends Anal Chem* **2024**, 180, 117920.

32. Singh S. Handbook of Liquid Crystals. *Springer* **2024**, 1, 4.

33. de Gennes PG, Prost J. The physics of liquid crystals. *International series of monographs on physics* **1995**, 2, 10-17.

34. Blinov LM. Structure and properties of liquid crystals. *Springer* **2010**, 123, 19-39.

35. Khoo I-C. Liquid crystals. *John Wiley & Sons* **2022**, 1-11.

36. Reinitzer F. Beiträge zur Kenntniss des Cholesterins. *Monatsh Chem* **1888**, 9, 421-441.

37. Lehmann O. Über fliessende Krystalle. *Z Phys Chem* **1889**, 4U, 462-472.

38. Mitov M. Liquid-Crystal Science from 1888 to 1922: Building a Revolution. *ChemPhysChem* **2014**, 15, 1245-1250.

39. de Gennes PG. Soft matter (Nobel lecture). *Angew Chem Int Ed* **1992**, 31, 842-845.

40. Ajdari A. Pierre-Gilles de Gennes (1932-2007). *Science* **2007**, 317, 466-466.

41. Schadt M. Liquid crystal materials and liquid crystal displays. *Annu Rev Mater Sci* **1997**, 27, 305-379.

42. Bahadur B. Liquid crystal-applications and uses. *World scientific* **1990**, 1, 398-401.

43. Yang D-K, Wu S-T. Fundamentals of liquid crystal devices. *John Wiley & Sons* **2014**, 235.

44. Geffroy B, Le Roy P, Prat C. Organic light-emitting diode (OLED) technology: materials, devices and display technologies. *Polym Int* **2006**, 55, 572-582.

45. Tsujimura T. OLED display fundamentals and applications. *John Wiley & Sons* **2017**, 1-5.

46. Dierking I, Neto AMF. Lyotropic liquid crystals. *Oxford University Press* **2024**, 143-171.

47. Vertogen G, De Jeu WH. Thermotropic liquid crystals, fundamentals. *Springer* **2012**, 45, 3-8.

48. Pershan PS. Structure of liquid crystal phases. *World Scientific* **1988**, 23, 7.

49. Jen S, Clark NA, Pershan PS, Priestley EB. Polarized Raman scattering studies of orientational order in uniaxial liquid crystalline phases. *J Chem Phys* **1977**, 66, 4635-4661.

50. Collings PJ, Goodby JW. Introduction to liquid crystals: chemistry and physics. *CRC Press* **2019**, 420.

51. Tsvetkov V. On molecular order in the anisotropic liquid phase. *Acta Physicochim URSS* **1942**, 16, 6.

52. Kuczyński W, Żywucki B, Małecki J. Determination of orientational order parameter in various liquid-crystalline phases. *Mol Cryst Liq Cryst* **2002**, 381, 1-19.

53. Ghosh SK. A model for the orientational order in liquid crystals. *Nuovo Cimento D* **1984**, 4, 229-244.

54. Hanemann T, Haase W, Svoboda I, Fuess H. Crystal structure of 4′-pentyl-4-cyanobiphenyl (5CB). *Liq Cryst* **1995**, 19, 699-702.

55. Mitov M. Cholesteric Liquid Crystals with a Broad Light Reflection Band. *Adv Mater* **2012**, 24, 6260-6276.

56. Eelkema R, Feringa BL. Amplification of chirality in liquid crystals. *Org Biomol Chem* **2006**, 4, 3729-3745.

57. Cook MJ, Wilson MR. Calculation of helical twisting power for liquid crystal chiral dopants. *J Chem Phys* **2000**, 112, 1560-1564.

58. Creagh LT, Kmetz AR. Mechanism of Surface Alignment in Nematic Liquid Crystals. *Mol Cryst Liq Cryst* **1973**, 24, 59-68.

59. Berreman DW. Solid Surface Shape and the Alignment of an Adjacent Nematic Liquid Crystal. *Phys Rev Lett* **1972**, 28, 1683-1686.

60. Chiou D-R, Chen L-J, Lee C-D. Pretilt Angle of Liquid Crystals and Liquid-Crystal Alignment on Microgrooved Polyimide Surfaces Fabricated by Soft Embossing Method. *Langmuir* **2006**, 22, 9403-9408.

61. Yaroshchuk O, Reznikov Y. Photoalignment of liquid crystals: basics and current trends. *J Mater Chem C* **2012**, 22, 286-300.

62. Rapini A, Papoular M. Distorsion d'une lamelle nématique sous champ magnétique conditions d'ancrage aux parois. *J Phys Colloq* **1969**, 30, C4-54-C54-56.

63. Andrienko D. Introduction to liquid crystals. *J Mol Liq* **2018**, 267, 520-541.

64. Frank FC. I. Liquid crystals. On the theory of liquid crystals. *Spec Discuss Faraday Soc Special* **1958**, 25, 19-28.

65. Oseen C. The theory of liquid crystals. *Trans Faraday Soc* **1933**, 29, 883-899.

66. Kilian A. Computer simulations of nematic droplets. *Liq Cryst* **1993**, 14, 1189-1198.

67. Raj RSA, Joseph A, Hussain S, Fahad M, Maity T, Sarun PM*, et al.* Frequency and temperature dependent dielectric properties of CoFe2−xYxO4: polarization and conduction mechanisms related to crystallographic symmetry and electronic transitions. *J Mater Chem C* **2025**, 13, 5880-5910.

68. Smirnov I. The effect of MRET polymer compound on SAR values of RF phones. *J Microw Power Electromagn Energy* **2008**, 42, 42-54.

69. Alarifi SA, Mahmoud M. Laboratory dielectric measurements to evaluate the conductivity change in the presence of chelating agent with different brines. *Sci Rep* **2022**, 12, 19856.

70. De Ninno A, Nikollari E, Missori M, Frezza F. Dielectric permittivity of aqueous solutions of electrolytes probed by THz time-domain and FTIR spectroscopy. *Phys Lett A* **2020**, 384, 126865.

71. Kumar S. Liquid crystals: experimental study of physical properties and phase transitions. *Cambridge University Press* **2001**, 6-10.

72. Meyer RB. Distortion of a cholesteric structure by a magnetic field. *Appl Phys Lett* **1969**, 14, 208-209.

73. St. John WD, Fritz WJ, Lu ZJ, Yang DK. Bragg reflection from cholesteric liquid crystals. *Phys Rev E* **1995**, 51, 1191-1198.

74. Binet C, Mitov M, Boudet A. Bragg Reflections In Cholesteric Liquid Crystals: From Selectivity To Broadening And Reciprocally. *Mol Cryst Liq Cryst Sci Technol, Sect A* **2000**, 339, 111-123.

75. Parry E, Kim D-J, Castrejón-Pita AA, Elston SJ, Morris SM. Formation of radial aligned and uniform nematic liquid crystal droplets via drop-on-demand inkjet printing into a partially-wet polymer layer. *Optical Materials* **2018**, 80, 71-76.

76. Kamal W, Lin J-D, Elston SJ, Ali T, Castrejón-Pita AA, Morris SM. Electrically Tunable Printed Bifocal Liquid Crystal Microlens Arrays. *Adv Mater Interfaces* **2020**, 7, 2000578.

77. Kamal W, Li M, Lin J-D, Parry E, Jin Y, Elston SJ*, et al.* Spatially Patterned Polymer Dispersed Liquid Crystals for Image-Integrated Smart Windows. *Adv Opt Mater* **2022**, 10, 2101748.

78. Li M, Kamal W, Orr ACJ, Castrejón-Pita AA, Elston SJ, Morris SM. Printed Polymer-Stabilized Chiral Nematic Liquid Crystal Privacy Windows. *Macromol Chem Phys* **2022**, 223, 2200154.

79. Xu FF, Li YJ, Lv Y, Dong H, Lin X, Wang K*, et al.* Flat-Panel Laser Displays Based on Liquid Crystal Microlaser Arrays. *CCS Chem* **2020**, 2, 369-375.

80. Aliño VJ, Sim PH, Choy WT, Fraser A, Yang K-L. Detecting Proteins in Microfluidic Channels Decorated with Liquid Crystal Sensing Dots. *Langmuir* **2012**, 28, 17571-17577.

81. Li J, Tian M, Xu H, Ding X, Guo J. Photoswitchable Fluorescent Liquid Crystal Nanoparticles and Their Inkjet-Printed Patterns for Information Encrypting and Anti-Counterfeiting. *Part Syst Charact* **2019**, 36, 1900346.

82. Hamlington BD, Steinhaus B, Feng JJ, Link D, Shelley MJ, Shen AQ. Liquid crystal droplet production in a microfluidic device. *Liq Cryst* **2007**, 34, 861-870.

83. Naoto Tamai NT, Takashi Ito TI, Hiroshi Masuhara HM. Second- and Third-Harmonic Generation from Optically Trapped Liquid Crystal Droplet. *Jpn J Appl Phys* **1996**, 35, L547.

84. Kim DS, Bae G, Bae BS, Han S, Shin SS, Gwag JS*, et al.* Monodispersed Liquid Crystal Droplets Fabricated by the Droplet Break-up Process in the Microfluidic System. *Mol Cryst Liq Cryst* **2014**, 596, 45-50.

85. Phanphak S, Pattanaporkratana A, Limtrakul J, Chattham N. Precession mechanism of nematic liquid crystal droplet under optical tweezers. *Sch Psychol Int* **2013**, 8883, 88830Y.

86. Wang J, Wang L, Song Y, Jiang L. Patterned photonic crystals fabricated by inkjet printing. *J Mater Chem C* **2013**, 1, 6048-6058.

87. Alamán J, Alicante R, Peña JI, Sánchez-Somolinos C. Inkjet printing of functional materials for optical and photonic applications. *Materials* **2016**, 9, 910.

88. Yang C-S, Lin C-J, Pan R-P, Que CT, Yamamoto K, Tani M*, et al.* The complex refractive indices of the liquid crystal mixture E7 in the terahertz frequency range. *J Opt Soc Am B* **2010**, 27, 1866-1873.

89. Orr ACJ, Qiu X, Kamal W, Sykes TC, Elston SJ, Yeomans JM*, et al.* Topologically frustrated structures in inkjet printed chiral nematic liquid crystal droplets – experiments and simulations. *Soft Matter* **2024**, 20, 7493-7501.

90. Ma X, Wu B, Hou L, Wu P. Edible Structurally Colored Plastics. *ACS Nano* **2025**, 19, 23945-23954.

91. Zhang Y, Yang H, Chen Y, Yu H. Progress in Fabrication and Applications of Cholesteric Liquid Crystal Microcapsules. *Chem Eur J* **2024**, 30, e202303198.

92. Lee SS, Kim JB, Kim YH, Kim S-H. Wavelength-tunable and shape-reconfigurable photonic capsule resonators containing cholesteric liquid crystals. *Sci Adv* **2018**, 4, eaat8276.

93. Lee SS, Kim S-H. Controlled Encapsulation of Cholesteric Liquid Crystals Using Emulsion Templates. *Macromol Res* **2018**, 26, 1054-1065.

94. Liu X, Debije MG, Heuts JPA, Schenning APHJ. Liquid-Crystalline Polymer Particles Prepared by Classical Polymerization Techniques. *Chem Eur J* **2021**, 27, 14168-14178.

95. Concellón A. Liquid Crystal Emulsions: A Versatile Platform for Photonics, Sensing, and Active Matter. *Angew Chem Int Ed* **2023**, 62, e202308857.

96. M S, Ameya D J, A.S VM. Perturbed soliton and director deformation in a ferronematic liquid crystal. *Chaos Soliton Fract* **2018**, 106, 220-226.

97. Andrienko D. Introduction to liquid crystals. *Journal of Molecular Liquids* **2018**, 267, 520-541.

98. Bell T, Li B, Zhang S. Structured Light Techniques and Applications. *Wiley EEE* **2016**, 1-24.

99. Wang W-Y, Cheng T-Y, Bai Z-X, Liu S, Lü J-Q. Vector Optical Beam with Controllable Variation of Polarization during Propagation in Free Space: A Review. *Appl Sci* **2021**, 11, 10664.

100. Pierangeli D, Conti C. Single-shot polarimetry of vector beams by supervised learning. *Nat Commun* **2023**, 14, 1831.

101. Khonina SN, Ustinov AV, Porfirev AP. Generation of Light Fields with Controlled Non-Uniform Elliptical Polarization When Focusing on Structured Laser Beams. *Photonics* **2023**, 10.

102. Ke L, Li C, Zhang S, Fang B, Tang Y, Hong Z*, et al.* Tight focusing field of cylindrical vector beams based on cascaded low-refractive index metamaterials. *Nanophotonics* **2023**, 12, 3563-3578.

103. Zhan Q. Cylindrical vector beams: from mathematical concepts to applications. *Adv Opt Photonics* **2009**, 1.

104. Bauer T, Banzer P, Karimi E, Orlov S, Rubano A, Marrucci L*, et al.* Observation of optical polarization Möbius strips. *Science* **2015**, 347, 964-966.

105. Rosales-Guzmán C, Ndagano B, Forbes A. A review of complex vector light fields and their applications. *J Opt* **2018**, 20.

106. Maurer C, Jesacher A, Fürhapter S, Bernet S, Ritsch-Marte M. Tailoring of arbitrary optical vector beams. *New J Phys* **2007**, 9, 78-78.

107. Parigi V, D'Ambrosio V, Arnold C, Marrucci L, Sciarrino F, Laurat J. Storage and retrieval of vector beams of light in a multiple-degree-of-freedom quantum memory. *Nat Commun* **2015**, 6, 7706.

108. Padgett MJ. Orbital angular momentum 25 years on [Invited]. *Opt Express* **2017**, 25, 11265-11274.

109. Yao AM, Padgett MJ. Orbital angular momentum: origins, behavior and

applications. *Adv Opt Photonics* **2011**, 3.

110. Li M, Elston SJ, He C, Qiu X, Castrejón-Pita AA, Morris SM. Printed Liquid Crystal Optical Vortex Beam Generators. *Advanced Optical Materials* **2024**, 12.

111. Courtial J, Robertson DA, Dholakia K, Allen L, Padgett MJ. Rotational Frequency Shift of a Light Beam. *Phys Rev Lett* **1998**, 81, 4828-4830.

112. Molina-Terriza G, Torres JP, Torner L. Management of the angular momentum of light: preparation of photons in multidimensional vector states of angular momentum. *Phys Rev Lett* **2002**, 88, 013601.

113. Ritsch-Marte M. Orbital angular momentum light in microscopy. *Phil Trans R Soc A* **2017**, 375.

114. Hell SW, Wichmann J. Breaking the diffraction resolution limit by stimulated emission: stimulated-emission-depletion fluorescence microscopy. *Opt Lett* **1994**, 19, 780-782.

115. Friese MEJ, Nieminen TA, Heckenberg NR, Rubinsztein-Dunlop H. Optical alignment and spinning of laser-trapped microscopic particles. *Nature* **1998**, 394, 348-350.

116. Garces-Chavez V, McGloin D, Padgett MJ, Dultz W, Schmitzer H, Dholakia K. Observation of the transfer of the local angular momentum density of a multiringed light beam to an optically trapped particle. *Phys Rev Lett* **2003**, 91, 093602.

117. Padgett M, Bowman R. Tweezers with a twist. *Nat Photonics* **2011**, 5, 343-348.

118. He C, Lin J, Chang J, Antonello J, Dai B, Wang J*, et al.* Full Poincaré polarimetry enabled through physical inference. *Optica* **2022**, 9, 1109-1114.

119. He C, Chang J, Salter PS, Shen Y, Dai B, Li P*, et al.* Revealing complex optical phenomena through vectorial metrics. *Adv Photonics* **2022**, 4, 26001.

120. He C, Booth M. Extraordinary Beam Modulation with Ordinary GRIN Lenses. *Opt Photonics News* **2020**, 31, 47-47.

121. Chao H, Jianyu L, Ben D, Peng X, Martin B. GRIN lens: a new element for complex vectorial beam modulation. Proc.SPIE **2020**, 112970O.

122. Chao H, Jintao C, Honghui H, Shaoxiong L, Daniel SE, Hui M*, et al.* GRIN lens based polarization endoscope: from conception to application. *SPIE* **2020**, 11251, 112510Z.

123. Yue F, Wen D, Xin J, Gerardot BD, Li J, Chen X. Vector Vortex Beam Generation with a Single Plasmonic Metasurface. *ACS Photonics* **2016**, 3, 1558-1563.

124. D'Ambrosio V, Carvacho G, Graffitti F, Vitelli C, Piccirillo B, Marrucci L*, et al.*

Entangled vector vortex beams. *Phys Rev A* **2016**, 94.

125. Litchinitser NM. Structured Light Meets Structured Matter. *Science* **2012**, 337, 1054-1055.

126. Li Z-X, Ruan Y-P, Chen P, Tang J, Hu W, Xia K-Y*, et al.* Liquid crystal devices for vector vortex beams manipulation and quantum information applications. *Chin Opt Lett* **2021**, 19, 112601.

127. Giordani T, Suprano A, Polino E, Acanfora F, Innocenti L, Ferraro A*, et al.* Machine Learning-Based Classification of Vector Vortex Beams. *Phys Rev Lett* **2020**, 124, 160401.

128. Radwell N, Hawley RD, Götte JB, Franke-Arnold S. Achromatic vector vortex beams from a glass cone. *Nat Commun* **2016**, 7, 10564.

129. Rong Z-Y, Han Y-J, Wang S-Z, Guo C-S. Generation of arbitrary vector beams with cascaded liquid crystal spatial light modulators. *Opt Express* **2014**, 22, 1636-1644.

130. Cai M-Q, Wang Z-X, Liang J, Wang Y-K, Gao X-Z, Li Y*, et al.* High-efficiency and flexible generation of vector vortex optical fields by a reflective phase-only spatial light modulator. *Appl Opt* **2017**, 56, 6175-6180.

131. Zhang Y, Li P, Ma C, Liu S, Cheng H, Han L*, et al.* Efficient generation of vector beams by calibrating the phase response of a spatial light modulator. *Appl Opt* **2017**, 56, 4956-4960.

132. Hu Q, Dai Y, He C, Booth MJ. Arbitrary vectorial state conversion using liquid crystal spatial light modulators. *Opt Commun* **2020**, 459, 125028.

133. Rao AS, Kumar P, Omatsu T. Cylindrical Vector Vortex Beams Generation with a Single Phase Encoded Spatial Light Modulator. *CLEO/Europe-EQEC* **2023**, 1-1.

134. Szatkowski M, Masajada J, Augustyniak I, Nowacka K. Generation of composite vortex beams by independent Spatial Light Modulator pixel addressing. *Opt Commun* **2020**, 463, 125341.

135. Mei-Li H, Mao-Ling C, Chau-Jern C. Improvement of the complex modulated characteristic of cascaded liquid crystal spatial light modulators by using a novel amplitude compensated technique. *Opt Eng* **2007**, 46, 070501.

136. Cardano F, Karimi E, Slussarenko S, Marrucci L, de Lisio C, Santamato E. Polarization pattern of vector vortex beams generated by q-plates with different topological charges. *Appl Opt* **2012**, 51, C1-C6.

137. Rubano A, Cardano F, Piccirillo B, Marrucci L. Q-plate technology: a progress review [Invited]. *J Opt Soc Am B* **2019**, 36, D70-D87.

138. Zhang Y, Gao J, Yang X. Spatial variation of vector vortex beams with plasmonic metasurfaces. *Sci Rep* **2019**, 9, 9969.

139. Bao Y, Ni J, Qiu C-W. A Minimalist Single-Layer Metasurface for Arbitrary and Full Control of Vector Vortex Beams. *Adv Mater* **2020**, 32, 1905659.

140. Shen Y, He C, Song Z, Chen B, He H, Ma Y*, et al.* Topologically controlled multiskyrmions in photonic gradient-index lenses. *Phys Rev Appl* **2024**, 21, 024025.

141. He C, Chang J, Hu Q, Wang J, Antonello J, He H*, et al.* Complex vectorial optics through gradient index lens cascades. *Nat Commun* **2019**, 10, 4264.

142. Wang AA, Ma Y, Zhang Y, Zhao Z, Cai Y, Qiu X*, et al.* Unlocking new dimensions in photonic computing using optical Skyrmions. *arXiv preprint arXiv:240716311* **2024**.

143. Park J-U, Hardy M, Kang SJ, Barton K, Adair K, Mukhopadhyay Dk*, et al.* High-resolution electrohydrodynamic jet printing. *Nat Mater* **2007**, 6, 782-789.

144. Park J-U, Lee JH, Paik U, Lu Y, Rogers JA. Nanoscale Patterns of Oligonucleotides Formed by Electrohydrodynamic Jet Printing with Applications in Biosensing and Nanomaterials Assembly. *Nano Lett* **2008**, 8, 4210-4216.

145. Mishra S, Barton KL, Alleyne AG, Ferreira PM, Rogers JA. High-speed and drop-on-demand printing with a pulsed electrohydrodynamic jet. *J Micromech Microeng* **2010**, 20, 095026.

146. Parry E, Kim D-J, Castrejón-Pita AA, Elston SJ, Morris SM. Formation of radial aligned and uniform nematic liquid crystal droplets via drop-on-demand inkjet printing into a partially-wet polymer layer. *Opt Mater* **2018**, 80, 71-76.

147. Born M, Wolf E. Principles of optics: electromagnetic theory of propagation, interference and diffraction of light. *Elsevier* **2013**, 10-18.

148. Huard S. Polarization of light. *Wiley-VCH* **1997**, 348.

149. Goldstein DH. Polarized Light. *CRC Press* **2017**, 31-43.

150. Tuchin VV. Tissue optics. *SPIE* **2015**, 40.

151. Goldstein D, Goldstein DH. Polarized Light, revised and expanded. *CRC press* **2003**, 83, 1-5.

152. Azzam RMA, Bashara NM. Ellipsometry and Polarized Light. *Phys Today* **1977**, 31(11), 72.

153. Gutiérrez-Vega JC. The field of values of Jones matrices: classification and special cases. *Proc Math Phys Eng Sci* **2020**, 476, 20200361.

154. Hall SA, Hoyle MA, Post JS, Hore DK. Combined Stokes vector and Mueller

matrix polarimetry for materials characterization. *Anal Chem* **2013**, 85, 7613-7619.

155. Schirmer J, Schmidt-Kaler T. Liquid crystal phase retarder with broad spectral range. *Opt Commun* **2000**, 176, 313-317.

156. Oldenbourg R. Polarization Microscopy. *Biomedical Optical Phase Microscopy and Nanoscopy* **2013**, 311-338.

157. Lu S-Y, Chipman RA. Interpretation of Mueller matrices based on polar decomposition. *J Opt Soc Am A* **1996**, 13, 1106-1113.

158. Yang C-S, Lin C-J, Pan R-P, Que CT, Yamamoto K, Tani M*, et al.* The complex refractive indices of the liquid crystal mixture E7 in the terahertz frequency range. *J Opt Soc Am B* **2010**, 27, 1866-1873.

159. Azzam R. Mueller-matrix ellipsometry: a review. *SPIE* **1997**, 3121, 396.

160. K. U S, Mahato KK, Mazumder N. Polarization-resolved Stokes-Mueller imaging: a review of technology and applications. *Lasers Med Sci* **2019**, 34, 1283-1293.

161. Goldstein DH, Chipman RA. Error analysis of a Mueller matrix polarimeter. *J Opt Soc Am A* **1990**, 7, 693-700.

162. Smith MH. Optimization of a dual-rotating-retarder Mueller matrix polarimeter. *Appl Opt* **2002**, 41, 2488-2493.

163. Azzam RMA. Photopolarimetric measurement of the Mueller matrix by Fourier analysis of a single detected signal. *Opt Lett* **1978**, 2, 148-150.

164. Zetie KP, Adams SF, Tocknell RM. How does a Mach-Zehnder interferometer work? *Phys Educ* **2000**, 35, 46.

165. Ben-Aryeh Y. Phase estimation by photon counting measurements in the output of a linear Mach–Zehnder interferometer. *J Opt Soc Am B* **2012**, 29, 2754-2764.

166. Mytsyk BH, Demyanyshyn NM, Andrushchak AS, Maksishko YY, Kohut ZO, Kityk AV. Characterization of photoelastic materials by Mach–Zehnder interferometry: Application to trigonal calcium galogermanate (CGG) crystals. *J Appl Phys* **2024**, 135.

167. Gao S, Speirits FC, Castellucci F, Franke-Arnold S, Barnett SM, Götte JB. Paraxial skyrmionic beams. *Phys Rev A* **2020**, 102, 053513.

168. He C, Shen Y, Forbes A. Towards higher-dimensional structured light. *Light Sci Appl* **2022**, 11, 205.

169. Shen Y, Zhang Q, Shi P, Du L, Yuan X, Zayats AV. Optical skyrmions and other topological quasiparticles of light. *Nat Photonics* **2024**, 18, 15-25.

170. Wang AA, Zhao Z, Ma Y, Cai Y, Morris S, He H*, et al.* Generalized Skyrmions. *arXiv preprint arXiv:240917390* **2024**.

171. He C, Chen B, Song Z, Zhao Z, Ma Y, He H*, et al.* A reconfigurable arbitrary retarder array as complex structured matter. *Nat Commun* **2025**, 16(1), 4902.

172. Orr ACJ, Qiu X, Kamal W, Sykes TC, Elston SJ, Yeomans JM*, et al.* Topologically frustrated structures in inkjet printed chiral nematic liquid crystal droplets - experiments and simulations. *Soft Matter* **2024**, 20, 7493-7501.

173. Allen L, Beijersbergen MW, Spreeuw RJC, Woerdman JP. Orbital angular momentum of light and the transformation of Laguerre-Gaussian laser modes. *Phys Rev A* **1992**, 45, 8185-8189.

174. Xue Y, Kuang C, Li S, Gu Z, Liu X. Sharper fluorescent super-resolution spot generated by azimuthally polarized beam in STED microscopy. *Opt Express* **2012**, 20, 17653-17666.

175. Sheppard CJR, Choudhury A. Annular pupils, radial polarization, and superresolution. *Appl Opt* **2004**, 43, 4322-4327.

176. Tang F, Wang Y, Qiu L, Zhao W, Sun Y. Super-resolution radially polarized-light pupil-filtering confocal sensing technology. *Appl Opt* **2014**, 53, 7407-7414.

177. Cardano F, Karimi E, Marrucci L, de Lisio C, Santamato E. Generation and dynamics of optical beams with polarization singularities. *Opt Express* **2013**, 21, 8815-8820.

178. Naidoo D, Roux FS, Dudley A, Litvin I, Piccirillo B, Marrucci L*, et al.* Controlled generation of higher-order Poincaré sphere beams from a laser. *Nat Photonics* **2016**, 10, 327-332.

179. Beckley AM, Brown TG, Alonso MA. Full Poincaré beams. *Opt Express* **2010**, 18, 10777-10785.

180. Freund I. Polarization singularity indices in Gaussian laser beams. *Opt Commun* **2002**, 201, 251-270.

181. Alpmann C, Schlickriede C, Otte E, Denz C. Dynamic modulation of Poincaré beams. *Sci Rep* **2017**, 7, 8076.

182. Yang Z, Wang Z, Wang Y, Feng X, Zhao M, Wan Z*, et al.* Generalized Hartmann-Shack array of dielectric metalens sub-arrays for polarimetric beam profiling. *Nat Commun* **2018**, 9, 4607.

183. Chang J, He H, He C, Wang Y, Zeng N, Liao R*, et al.* Optimization of GRIN lens Stokes polarimeter. *Appl Opt* **2015**, 54, 7424-7432.

184. Lin Z, Rusch L, Chen Y, Shi W. Chip-scale, full-Stokes polarimeter. *Opt Express* **2019**, 27, 4867-4877.

185. Wu PC, Chen J-W, Yin C-W, Lai Y-C, Chung TL, Liao CY*, et al.* Visible Metasurfaces for On-Chip Polarimetry. *ACS Photonics* **2018**, 5, 2568-2573.

186. Nishizaki Y, Valdivia M, Horisaki R, Kitaguchi K, Saito M, Tanida J*, et al.* Deep learning wavefront sensing. *Opt Express* **2019**, 27, 240-251.

187. Zhang Y-L, Cao F. Fine particulate matter (PM2.5) in China at a city level. *Sci Rep* **2015**, 5, 14884.

188. Chrysostomou A, Lucas PW, Hough JH. Circular polarimetry reveals helical magnetic fields in the young stellar object. *Nature* **2007**, 450, 71-73.

189. Cotton DV, Bailey J, Howarth ID, Bott K, Kedziora-Chudczer L, Lucas PW*, et al.* Polarization due to rotational distortion in the bright star Regulus. *Nat Astron* **2017**, 1, 690-696.

190. Totzeck M, Ulrich W, Göhnermeier A, Kaiser W. Pushing deep ultraviolet lithography to its limits. *Nat Photonics* **2007**, 1, 629-631.

191. Anastasiadou M, Martino AD, Clement D, Liège F, Laude-Boulesteix B, Quang N*, et al.* Polarimetric imaging for the diagnosis of cervical cancer. *Phys Status Solidi C* **2008**, 5, 1423-1426.

192. Ji N. Adaptive optical fluorescence microscopy. *Nat Methods* **2017**, 14, 374-380.

193. Sabatke DS, Descour MR, Dereniak EL, Sweatt WC, Kemme SA, Phipps GS. Optimization of retardance for a complete Stokes polarimeter. *Opt Lett* **2000**, 25, 802-804.

194. De Martino A, Kim Y-K, Garcia-Caurel E, Laude B, Drévillon B. Optimized Mueller polarimeter with liquid crystals. *Opt Lett* **2003**, 28, 616-618.

195. Alali S, Yang T, Vitkin IA. Rapid time-gated polarimetric Stokes imaging using photoelastic modulators. *Opt Lett* **2013**, 38, 2997-3000.

196. Liao R, Ma H. Study on errors of nonsimultaneous polarized-light scattering measurements of suspended rod-shaped particles. *Appl Opt* **2015**, 54, 418-424.

197. Azzam RMA. Arrangement of four photodetectors for measuring the state of polarization of light. *Opt Lett* **1985**, 10, 309-311.

198. Wu C, Ko J, Davis CC. Determining the phase and amplitude distortion of a wavefront using a plenoptic sensor. *J Opt Soc Am A* **2015**, 32, 964-978.

199. Shaw M, O'Holleran K, Paterson C. Investigation of the confocal wavefront sensor and its application to biological microscopy. *Opt Express* **2013**, 21, 19353-19362.

200. Roddier F. Curvature sensing and compensation: a new concept in adaptive optics. *Appl Opt* **1988**, 27, 1223-1225.

201. Robert AG. Phase Retrieval And Diversity In Adaptive Optics. *Opt Eng* **1982**,

21, 215829.

202. Platt Ben C, Shack R. History and Principles of Shack-Hartmann Wavefront Sensing. *J Refract Surg* **2001**, 17, S573-S577.

203. Singh K, Tabebordbar N, Forbes A, Dudley A. Digital Stokes polarimetry and its application to structured light: tutorial. *J Opt Soc Am A* **2020**, 37, C33-C44.

204. Kilosanidze B, Kakauridze G, Chaganava I, Dadivadze V, Mshvenieradze Y. Full Stokes polarimetry based on the polarization-holographic diffraction element of an optimal configuration. *EPJ Web Conf* **2024**, 309, 02009.

205. Gao C, Wang F, Wen X, Weng J, Lei B. Error calibration method for a vortex retarder based spatially modulated polarimeter. *Measurement* **2023**, 212, 112631.

206. Imazawa R, Kawano Y, Ono T, Itami K. Development of real-time rotating waveplate Stokes polarimeter using multi-order retardation for ITER poloidal polarimeter. *Rev Sci Instrum* **2016**, 87, 013503.

207. Wang Y, Su Y, Sun X, Hao X, Liu Y, Zhao X*, et al.* Principle and Implementation of Stokes Vector Polarization Imaging Technology. *Appl Sci* **2022**, 12, 6613.

208. Huang J, Yao L, Wu S, Wang G. Wavefront Reconstruction of Shack-Hartmann with Under-Sampling of Sub-Apertures. *Photonics* **2023**, 10.

209. Go G-H, Lee D-g, Oh J, Song G, Lee D, Jang M. Meta Shack–Hartmann wavefront sensor with large sampling density and large angular field of view: phase imaging of complex objects. *Light Sci Appl* **2024**, 13, 187.

210. Tyson RK, Frazier BW. Principles of Adaptive Optics (5th ed.). *CRC Press* **2022**, 356.

211. He C, Lin J, Chang J, Antonello J, Dai B, Wang J*, et al.* Full Poincaré polarimetry enabled through physical inference. *Optica* **2022**, 9, 1109-1114.

212. He C, Chang J, Hu Q, Wang J, Antonello J, He H*, et al.* Complex vectorial optics through gradient index lens cascades. *Nature Communications* **2019**, 10, 4264.

213. Li C-Y, Liu S-J, Yu B-S, Wu H-J, Rosales-Guzmán C, Shen Y*, et al.* Toward Arbitrary Spin-Orbit Flat Optics Via Structured Geometric Phase Gratings. *Laser Photonics Rev* **2023**, 17, 2200800.

214. Shi Y, Salter PS, Li M, Taylor RA, Elston SJ, Morris SM*, et al.* Two-Photon Laser-Written Photoalignment Layers for Patterning Liquid Crystalline Conjugated Polymer Orientation. *Adv Funct Mater* **2021**, 31, 2007493.

215. Xu A, Nourshargh C, Salter PS, He C, Elston SJ, Booth MJ*, et al.* Laser-Written Tunable Liquid Crystal Aberration Correctors. *ACS Photonics* **2023**, 10, 3401-3408.

Appendix

Mueller Matrices of Other LC Droplets

This section presents MM measurements of CLC droplets with different pitches, printed on homeotropic and planar alignment layers, which were not included in the main text.

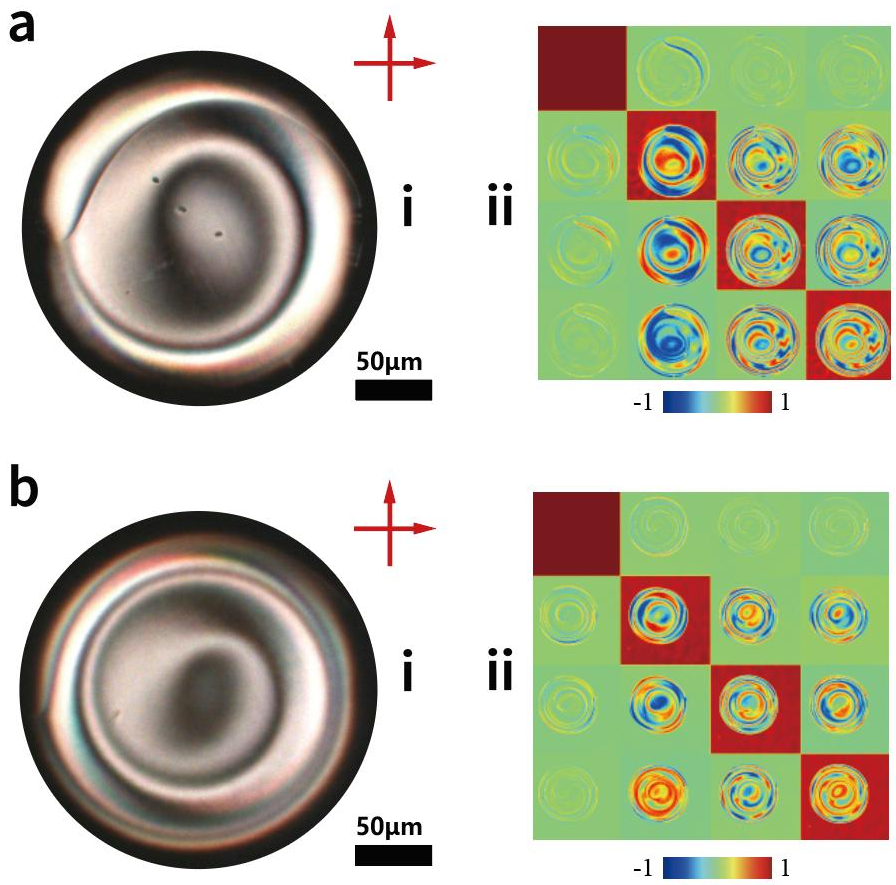


Figure A1 Experimental results demonstrating the full optical response of LC droplets on a glass substrate with a planar alignment layer and various chiral dopant concentrations. As the concentration of chiral dopant increases, it results in the formation of a spiral texture. (a) An $E7 + 0.5\ \mathrm{wt.\%R811}$ mixture droplet on a planar alignment layer exhibits a spiral-like texture in the POM image in (i). (ii) the corresponding Mueller matrix. (b) Shows an $E7 + 1\mathrm{wt.\%\ R811}$ printed droplet. The POM image in (i) shows a larger spiral texture. (ii) the corresponding Mueller matrix. The single headed red arrows in (i) represent the orientations of the polarizer and analyser.

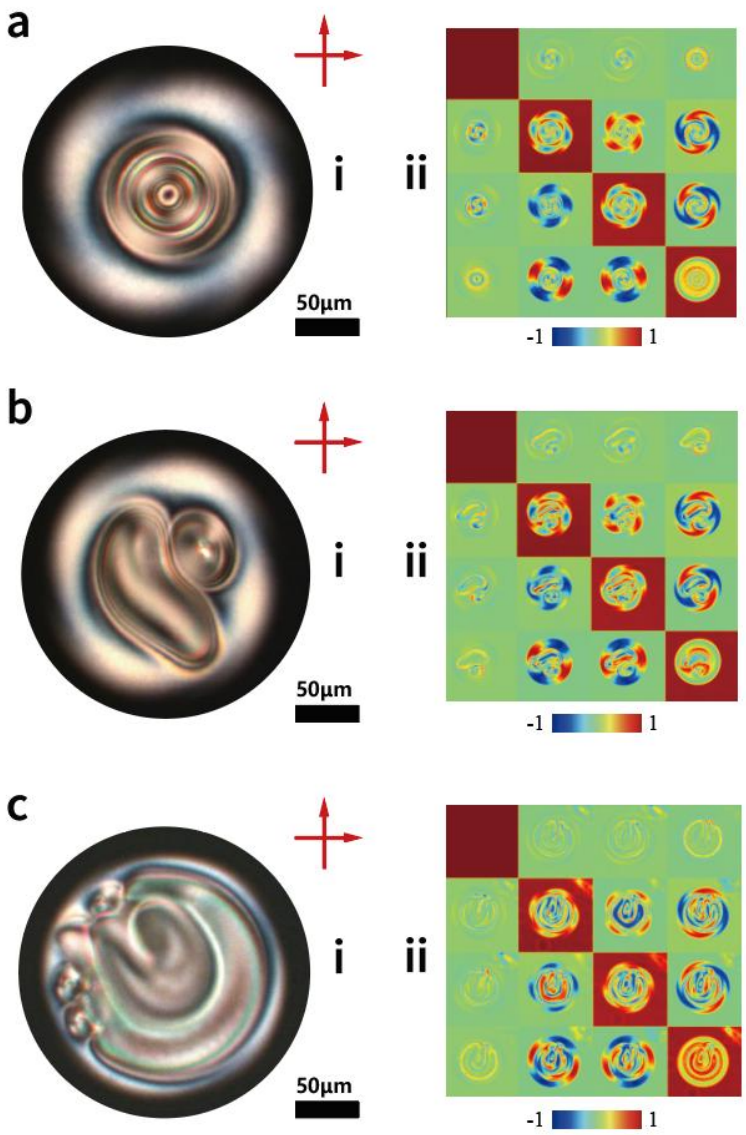


Figure A2 Experimental results demonstrating the full optical response of LC droplet arrays with homeotropic alignment substrate and various chiral dopant concentrations. As the concentration of chiral dopant increases, the interaction between the chiral nematic LC's general properties and the limitations imposed by the droplet surface results in the formation of a fingerprint-like texture. (a) An $E7 + 0.4\text{wt.}\,\%\,R811$ mixture printed on a homeotropic alignment layer exhibits a new feature near the centre in (i). The corresponding Mueller matrix in (ii) characterizes the droplet's full optical response. (b) Shows an $E7 + 0.6\text{wt.}\,\%\,R811$ printed droplet on a homeotropic alignment layer. The polarizing optical microscope (POM) image in (i) shows the droplet evolves to exhibit a fingerprint texture. (ii) the corresponding Mueller matrix. (c) Illustrates an $E7 + 0.8\,\text{wt.}\,\%\,R811$ printed droplet on a homeotropic alignment layer. The POM image between crossed polarizers (i) shows the fingerprint texture. (ii) the corresponding Mueller matrix. The single headed red arrows in (i) represent the orientations of the polarizer and analyser.

Zernike Polynomials

Zernike polynomials are a set of orthogonal basis functions defined over the unit circle and are widely used to represent optical wavefront aberrations. In this work, the Zernike polynomials $Z_i(\rho, \theta)$ follow the Noll indexing convention, where each mode corresponds to a specific classical aberration. The first Zernike mode ($i = 1$) corresponds to piston, which represents a constant phase offset and does not affect wavefront shape. It is therefore excluded from the wavefront reconstruction in this thesis. Modes starting from $i = 2$ describe physically meaningful aberrations such as tilt, defocus, astigmatism, coma, and spherical aberration. **Table A1** lists the Zernike modes used in this thesis.

Noll index	**Aberration name**	**Conventional symbol**	**Zernike polynomial** $Z_i(\rho, \theta)$
1	Piston	Z_1	1
2	Horizontal tilt	Z_2	$2\rho\cos\theta$
3	Vertical tilt	Z_3	$2\rho\sin\theta$
4	Defocus	Z_4	$\sqrt{3}(2\rho^2 - 1)$
5	Oblique astigmatism	Z_5	$\sqrt{6}\rho^2\sin 2\theta$

6	Vertical astigmatism	Z_6	$\sqrt{6}\rho^2\cos2\theta$
7	Vertical coma	Z_7	$\sqrt{8}(3\rho^3-2\rho)\sin\theta$
8	Horizontal coma	Z_8	$\sqrt{8}(3\rho^3-2\rho)\cos\theta$
9	Vertical trefoil	Z_9	$\sqrt{8}\rho^3\sin3\theta$
10	Oblique trefoil	Z_{10}	$\sqrt{8}\rho^3\cos3\theta$

Table A1 Zernike polynomial definitions based on the Noll indexing scheme used for wavefront reconstruction in this thesis.